แอมเพอโรเมทริกเซ็นเซอร์แบบเลือกจำเพาะสูงสำหรับการตรวจติดตามคาร์บอนมอนอกไซด์

นางสาวชนัดดา ภวชโลทร

วิทยานิพนธ์นี้เป็นส่วนหนึ่งของการศึกษาตามหลักสูตรปริญญาวิทยาศาสตรดุษฎีบัณฑิต
สาขาวิชาเคมี ภาควิชาเคมี
คณะวิทยาศาสตร์ จุฬาลงกรณ์มหาวิทยาลัย
ปีการศึกษา 2554
ลิขสิทธิ์ของจุฬาลงกรณ์มหาวิทยาลัย

HIGHLY SELECTIVE AMPEROMETRIC SENSORS FOR CARBON MONOXIDE
MONITORING

Miss Chanadda Phawachalotorn

A Dissertation Submitted in Partial Fulfillment of the Requirements
for the Degree of Doctor of Philosophy Program in Chemistry
Department of Chemistry
Faculty of Science
Chulalongkorn University
Academic Year 2011
Copyright of Chulalongkorn University

Thesis Title   HIGHLY SELECTIVE AMPEROMETRIC SENSORS FOR CARBON MONOXIDE MONITORING

By   Miss Chanadda Phawachalotorn

Field of Study   Chemistry

Thesis Advisor   Assistant Professor Oravan Sanguanruang, Ph.D.

Thesis Co-advisor   Professor Tatsumi Ishihara, Ph.D.

   Accepted by the Faculty of Science, Chulalongkorn University in Partial Fulfillment of the Requirements for the Doctoral Degree

……………………………………….. Dean of the Faculty of Science

(Professor Supot Hannongbua, Dr.rer.nat)

THESIS COMMITTEE

……………………………………….… Chairman

(Assistant Professor Preecha Lertpratchya, Ph.D.)

……………………………………….… Thesis Advisor

(Assistant Professor Oravan Sanguanruang, Ph.D.)

……………………………………….… Thesis Co-advisor

(Professor Tatsumi Ishihara, Ph.D.)

……………………………………….… Examiner

(Assistant Professor Soamwadee Chaianansutcharit, Ph.D.)

……………………………………….… Examiner

(Parichatr Vanalabhpatana, Ph.D.)

……………………………………….… External Examiner

(Siriporn Larpkiattaworn, Ph.D.)

ชนัดดา ภวชโลทร : แอมเพอโรเมทริกเซ็นเซอร์แบบเลือกจำเพาะสูงสำหรับการตรวจ
ติดตามคาร์บอนมอนอกไซด์. (HIGHLY SELECTIVE AMPEROMETRIC
SENSORS FOR CARBON MONOXIDE MONITORING) อ. ที่ปรึกษาวิทยานิพนธ์
หลัก : ผศ.ดร. อรวรรณ สงวนเรือง, อ. ที่ปรึกษาวิทยานิพนธ์ร่วม : Prof. Tatsumi
Ishihara, 107 หน้า.

ศึกษาตัวตรวจวัดแก๊สคาร์บอนมอนอกไซด์แบบแอมเพอโรเมตริกโดยการใช้
สารประกอบเพอรอฟสไกต์ $LaGaO_3$ ที่มีการเติมเหล็กลงไปเป็นอิเล็กโตรไลต์ อิเล็กโตรดสอง
ชนิดคือ Au10wt%-ITO955 (แคโทด) และ RuO_2-LSC64 (แอโนด) ถูกเคลือบลงบนแผ่น
อิเล็กโตรไลต์ในแต่ละด้าน เชื่อมต่อวงจรด้วยแผ่นทองคำและแผ่นแพลทินัมตามลำดับ นำไป
วางในท่อเซรามิกที่ต่ออยู่กับท่อแก๊สและวงจรไฟฟ้า อุณหภูมิที่ทำการศึกษาอยู่ในช่วง
300-500 องศาเซลเซียส จากผลการศึกษาความไวต่อแก๊สคาร์บอนมอนอกไซด์พบว่า
สารประกอบเพอรอฟสไกต์ที่มีการเติมเหล็กลงไป 15 mol% (LSGF 828515) ให้ค่าการ
ตอบสนองมากที่สุด และค่าความไวในการตอบสนองจะเพิ่มมากขึ้นตามอุณหภูมิที่เพิ่มขึ้นด้วย
นอกจากนี้ยังพบว่า ตัวตรวจวัดที่ทำการศึกษานี้มีความเลือกจำเพาะต่อแก๊ส
คาร์บอนมอนอกไซด์สูงที่สุดเมื่อเปรียบเทียบกับแก๊สชนิดอื่นๆ ที่สามารถพบได้ในท่อปล่อย
แก๊ส เช่น คาร์บอนไดออกไซด์ มีเทน และไฮโดรเจน กล่าวคือ มีการตอบสนองต่อแก๊สเหล่านี้
น้อยมากจนแทบไม่เห็นการเปลี่ยนแปลง แม้กระทั่งในส่วนของแก๊สไฮโดรเจนเองซึ่งเป็นแก๊ส
ที่ค่อนข้างว่องไวต่อการเกิดปฏิกิริยาออกซิเดชันก็ตาม ในการศึกษาผลของการเติมโลหะลงไป
ในขั้วแอโนด (LSC64) พบว่า LSC64 ที่ถูกเติมด้วยแพลทินัมหรือแพลเลเดียมแสดงการ
ตอบสนองต่อแก๊สคาร์บอนมอนอกไซด์สูงกว่าในกรณีที่ไม่มีการเติมโลหะใดๆ ลงไปใน
LSC64 และยังพบว่า ภายใต้สภาวะที่ทำการศึกษานั้น ไม่มีผลของแก๊สหรือปัจจัยใดๆ ที่ทำให้
ตัวตรวจวัดเกิดการเปลี่ยนแปลงทางด้านโครงสร้าง

ภาควิชา............เคมี............. ลายมือชื่อนิสิต..
สาขาวิชา............เคมี............. ลายมือชื่อ อ.ที่ปรึกษาวิทยานิพนธ์หลัก.....................................
ปีการศึกษา........2554............ ลายมือชื่อ อ.ที่ปรึกษาวิทยานิพนธ์ร่วม ....

5073898723 : MAJOR CHEMISTRY

KEYWORDS : $LaGaO_3$-BASED ELECTROLYTE / CO SENSOR / AMPEROMETRIC SENSOR / LSGMF / LSGF /

CHANADDA PHAWACHALOTORN : HIGHLY SELECTIVE AMPEROMETRIC SENSORS FOR CARBON MONOXIDE MONITORING. ADVISOR : ASST. PROF. ORAVAN SANGUANRUANG, Ph.D., CO-ADVISOR : PROF. TATSUMI ISHIHARA, Ph.D., 107 pp.

An amperometric carbon monoxide sensor using Fe-doped $LaGaO_3$ oxides as electrolyte was investigated. The electrodes which are Au10wt%-ITO955 (as cathode) and RuO_2-LSC64 (as anode) were coated on each side of the electrolyte and connected with Au mesh and Pt mesh, respectively. The fabricated sensor was placed inside a ceramic tube which was attached with a gas flow assembly and external electrical contacts. The operating temperature is in the range of 300°C to 500°C. From this study, the perovskite compound doped with 15mol% Fe into Ga site (LSGF828515) showed the highest sensitivity and its sensitivity increased with increasing temperature. Moreover, the examined sensor exhibited higher selectivity to carbon monoxide compared with that of coexisting gases such as carbon dioxide, methane and hydrogen. Namely, the sensor has no significant responses to these coexisting gases, even hydrogen which is quite reactive to oxidation reaction. The effect of additive adding into anode (LSC64) was studied. It was found that LSC64 doped with Pt or Pd exhibited higher responses compared with that of non-doped LSC64 case. In addition, under sensing measurement conditions, there were no effects of gases or other factors on the sensor's structure.

Department : _____Chemistry_____   Student's Signature _____

Field of Study : _____Chemistry_____   Advisor's Signature _____

Academic Year : _____2011_____   Co-advisor's Signature _____

ACKNOWLEDGEMENTS

First of all, I would like to thank my advisor, Assistant Professor Dr. Oravan Sanguanruang, for giving me a chance to study here as Ph.D. candidate. Thank you for the encouragement and discussion during my work in Thailand.

This thesis could not successfully complete without the kindness of my co-advisor, Professor Tatsumi Ishihara. I would like to express my sincere gratitude to him for giving me an experience to do my research at Kyushu University, Japan and for introducing me into this intriguing research field. Thank you for knowledge and financial support and special thanks for patient guidance, the extensive encouragement and good suggestion through my work until I can get publications.

I would like to gratitude Assistant Professor Dr. Preecha Lertpratchya, Assistant Professor Dr. Soamwadee Chaianansutcharit, Dr. Parichatr Vanalabhpatana and Dr. Siriporn Larpkiattaworn as the chairman and members of this thesis committee, respectively, for all of their kindness and useful advice in the research.

I would like to thank Mr. Jun Iwata at Department of Applied Chemistry, Faculty of Engineering, Kyushu University, Japan for SEM images. I also want to thanks all of members at Professor Ishihara's laboratory for their assistance with the equipments.

Moreover, I would like to thank Department of Chemistry, Faculty of Science, Chulalongkorn University for the valuable knowledge and experience. In addition, I would like to thank the Development and Promotion of Science and Technology talents project (DPST) for financial support throughout of the course of my study and Center of Excellence on Petrochemical and Materials Technology.

Last but not least, I would like to express my deepest gratitude to my dear parents for their entirely care, financial support, encouragement and love.

CONTENTS

LIST OF TABLES

LIST OF FIGURES

Page

LIST OF SCHEMES

LIST OF ABBREVIATIONS

ppm	parts per million
ppb	parts per billion
NOx	Nitrogen oxide
HCs	Hydrocarbons
VOCs	Volatile organic compounds
O^{2-}	Oxide ion
SOFCs	Solid oxide fuel cells
YSZ	Yttria stabilized zirconia
SDC	Samaria doped ceria
LDC	Lanthanum doped ceria
°C	degree Celsius
EMF	Electromotive force
E_0	Electromotive force at a standard pressure
R	Gas constant / Resistance
T	Absolute temperature
n	Number of electrons involved in the electrochemical reaction of the gas molecule
F	Faraday constant
P_w	Gas partial pressure at the working electrode
P^0	Standard pressure
e^-	Electron
NASICON	$Na_3Zr_2Si_2PO_{12}$
SE	Sensing electrode
RE	Reference electrode
P_{O_2}	Partial pressure of oxygen
$i_{O_2}/i_{O_2}^0$	Current density for oxygen / for cathodic reaction
i_{CO}/i_{CO}^0	Current density for oxygen / for anodic reaction

α	Transference coefficient
E	Electrode potential
E^0	Equilibrium electrode potential
ΔG^0	Standard Gibbs energy change
E_{mix}	Mixed potential
A	Electrode area
D_i	Diffusion coefficient of i
δ	Diffusion boundary layer thickness / oxygen non-stoichiometry
I	Current
V	Voltage
I_{lim}	Limiting current
P_T	Total pressure
l	Length
x	Mole fraction
c_i	Concentration of i
MIECs	Mixed ionic-electronic conductors
ABO_3	Typical general formula of perovskites
X-O	Distance between X atom and oxygen atom
a, b, c	Unit lattice parameter
r_x	Ionic radius of x
t	Tolerance factor
M	Metal
σ	Total conductivity
σ_n	N-type electronic conductivity
σ_p	P-type electronic conductivity
σ_i	Ionic conductivity
$V_o^{\cdot\cdot}$	Oxygen vacancy
O_o^x	Lattice oxygen ion
$h^{\cdot}$	Electron holes

J_{O_2}	Oxygen flux
L	Membrane thickness
P'_{O_2}	High oxygen partial pressure
P''_{O_2}	Low oxygen partial pressure
σ_{amb}	Ambipolar conductivity
σ_e	Electronic conductivity
$LaGaO_3$	Lanthanum gallate
$LaCoO_3$	Lanthanum cobaltate
K	degree Kelvin
μ	micro-
LSGM8282	$La_{0.8}Sr_{0.2}Ga_{0.8}Mg_{0.2}O_3$
LSGMF828155	$La_{0.8}Sr_{0.2}Ga_{0.8}Mg_{0.15}Fe_{0.05}O_3$
LSGMF82811	$La_{0.8}Sr_{0.2}Ga_{0.8}Mg_{0.1}Fe_{0.1}O_3$
LSGMF828515	$La_{0.8}Sr_{0.2}Ga_{0.8}Mg_{0.05}Fe_{0.15}O_3$
LSGF8291	$La_{0.8}Sr_{0.2}Ga_{0.9}Fe_{0.1}O_3$
LSGF828515	$La_{0.8}Sr_{0.2}Ga_{0.85}Fe_{0.15}O_3$
LSGF8282	$La_{0.8}Sr_{0.2}Ga_{0.8}Fe_{0.2}O_3$
LSGF8273	$La_{0.8}Sr_{0.2}Ga_{0.7}Fe_{0.3}O_3$
LSC64	$La_{0.6}Sr_{0.4}CoO_3$
ITO955	$In_{0.95}Sn_{0.05}O_{1.5}$
SSR	Solid state reaction
M-	Mega-
m-	Milli-
Pa	Pascal
θ	Theta
k	kilo-
sec	Second
dc	Direct current
XRD	X-ray diffractometry
SEM	Scanning electron microscopy

%	percent
min	minute
h	hour
ml	milliliter
mm	millimeter
cm	centimeter
nm	nanometer
Å	Angstrom
T_{90}	90% response time

CHAPTER I

INTRODUCTION

Carbon monoxide (CO) is one of the most toxic pollutant gases in the environment. It is the product of incomplete combustion. CO is an odorless, colorless and undetectable from human senses. People may not know that they are being exposed with it. Thus, it is referred to as the "silent killer".

When CO is inhaled, it can bind to hemoglobin (Hb) more tightly than oxygen (O_2) and forms a compound called carboxyhemoglobin (COHb). The presence of COHb in bloodstream causes the body tissues become starved of oxygen, resulting in tissue hypoxia. Table 1.1 demonstrates the estimated COHb levels resulting from steady-state exposure and CO concentrations in atmosphere [1].

Table 1.1 Equilibrium carboxyhemoglobin levels resulting from steady-state exposure to increasing concentrations of carbon monoxide in ambient air[a] [1].

CO in atmosphere		Estimated COHb in blood (%)
%	ppm	
0.001	10	2
0.007	70	10
0.012	120	20
0.022	220	30
0.035-0.052	350-520	40-50
0.080-0.122	800-1220	60-70
0.195	1950	80

[a] Source: adapted from Winter and Miller (1976), Ellenhorn and Barceloux (1988).

Exposure to CO can cause the health risks associated with various CO concentrations. With low levels of CO poisoning, it results in flu-like symptoms such as mild headaches, slight nausea and confusion. At high levels, CO poisoning can cause unconsciousness and death. The acute effects produced by CO in relation to ambient concentration in parts per million are listed in Table 1.2.

Table 1.2 Carbon monoxide poisoning effects in relation to ambient concentration in ppm [2].

Concentration	Symptoms
35 ppm	Headache and dizziness within 6-8 hours of constant exposure
100 ppm	Slight headache in 2-3 hours
200 ppm	Slight headache within 2-3 hours; loss of judgment
400 ppm	Frontal headache within 1-2 hours
800 ppm	Dizziness, nausea and convulsions within 45 minutes; insensible within 2 hours
1,600 ppm	Headache, tachycardia, dizziness and nausea within 20 minutes; death in less than 2 hours
3,200 ppm	Headache, dizziness and nausea in 5-10 minutes; death within 30 min
6,400 ppm	Headache and dizziness in 1-2 minutes; convulsions, respiratory arrest and death in less than 20 minutes
12,800 ppm	Unconsciousness after 2-3 breaths; death in less than 3 minutes

Every year, hundreds of deaths are recorded from carbon monoxide which was produced by malfunctioning or improperly vented heating appliances [3-6]. Many more people suffer chronic illness brought on by less than lethal CO levels that go undetected. Thus, many kinds of gas sensors have been developed under the great demand for gas detection and monitoring because of the serious concern towards the growth of the environmental pollution.

1.1 Classification of sensors

Generally, a sensor is defined as a primary device which measures a physical input and converts it into an observable output signal. It is also called detector [7]. The output nowadays is preferably to be an electronic quantity. The basic requirements of sensors are [12]:

- high sensitivity;
- high selectivity;
- absence of hysteresis;
- high accuracy;
- high reproducibility;
- broad range of measurement and temperature;
- stability to noise or interference;
- high durability;
- simple calibration;
- rapid response;
- high reliability;
- low price;
- compact.

The classification of sensors by their principles of operation is divided into physical and chemical sensors which summarized in Table 1.3.

Table 1.3 Classification of sensors according to the principle of operation [8].

Physical sensors	Chemical sensors
- Optical sensors - Pressure sensors - Temperature sensors - Magnetic sensors - Acoustic sensors - Sensors for radioactive radiation	- Gas sensors - Humidity sensors - Ionic sensors - Biochemical sensors

1.2 Gas sensors

With dramatically increasing of global industrial growths caused the concerns towards the surroundings. The environmental pollutants such as carbon monoxide (CO), hydrocarbons (HCs), nitrogen oxide (NO) were emitted from automobiles and industrial processes. Therefore, the intensive demand on a reliable sensor for detection or monitoring environmental pollutant becomes increase. This need is not only on the development of efficiency materials but also highly sensitive of gas sensors.

Gas sensors are widely used in numerous fields with the two major groups of applications. One is the need for the detection of single gases such as NO_x, CO, HCs and SO_2. Single gas sensors can be used as fire detectors, leakage detectors, controllers of ventilation in cars and planes, alarm devices warning the overcoming of threshold concentration values of hazardous gases in the work places. Another application is for the monitoring of changes in the ambient; for example, the detection of volatile organic compounds (VOCs) or smells caused from food or household products in food industry and indoor air quality. Table 1.4 demonstrated some applications for gas sensors and electronic noses (or multisensors).

Among various analytical methods, solid state electrochemical gas sensors are predominant candidates for commercial gas sensor development with a variety of applications because this method is a selective and accurate way of sensing chemical species. The great attention on this type of sensors comes from their advantages such as compact, high sensitivities on the detection of very low concentration (ppm or ppb levels) of a wide range of various gas species, high selectivities, rapid responses and cost effective in large-scale production.

Table 1.4 Applications for gas sensors and electronic noses [9].

Systems	Applications
Automobiles	• Filter control • Car ventilation control • Gasoline vapor detection • Alcohol breath tests
Indoor air quality	• Air purifiers • Cooking control • Ventilation control
Safety	• Boiler control • Fire detection • Leak detection • Personal gas monitor • Toxic/flammable/explosive gas detectors
Environmental control	• Weather stations • Pollution monitoring
Food	• Process control • Food quality control • Packaging quality control
Medicine	• Breath analysis • Disease detection
Industrial production	• Process control • Fermentation control

However, solid-state electrochemical sensors can suffer from the problem on limitation of measurement accuracy and long-term stability. Thus, a lot of researches continue focusing on the gas sensing development to improve their higher sensitivities, higher selectivities and long-term stabilities at reduce cost.

1.3 Solid state electrochemical gas sensor

Depending on the mode of operation, these electrochemical sensors are generally categorized as potentiometric, amperometric, conductometric and so on. At the present, the major applications of commercial electrochemical gas sensors are based on potentiometric and amperometric modes. In potentiometric mode, the sensors allow the measuring of chemical activities or the electromotive forces, while in amperometric mode the electric current is measured. In addition, the applications of the electrochemical cells using solid electrolytes have several advantages including [10]:

- the generated electrical quantities (current and voltage) are easily to measurable with high accuracy,
- the measured quantity (e.g. partial pressure) is directly converted into an electrical signals (current and voltage),
- the signal is selective for the transferred component of the electrolyte.

Solid electrolytes are essential components of electrochemical gas sensors. Commonly, they operate at elevated temperature due to their low conductivities at low temperature.

1.3.1 Solid electrolyte membranes

In general, solid electrolyte membranes are classified into two major groups which are porous and dense membranes as further described.

1.3.1.1 Porous membranes

In porous membranes, oxygen is transferred as molecule form by diffusion, viscous flow and surface diffusion. Considering in terms of permeability, the porous membranes exhibit the high oxygen permeability compared with the dense membranes while the permselectivity is moderate. Both permeability and

permselectivity can be improved by preparing the membranes with a suitable pore size distribution and pore structure as displayed in Figure 1.1.
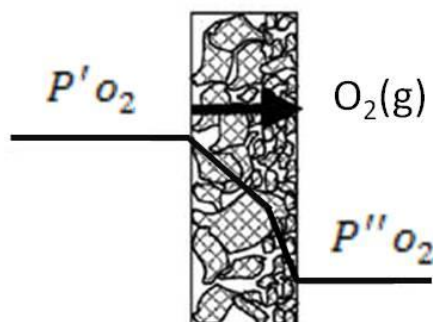
Figure 1.1 The representative porous membranes for oxygen transport [11].

1.3.1.2 Dense membranes

In this type of membrane, oxygen is transferred as ionic species (O^{2-}) by moving from vacancy to vacancy in the lattice of solid materials. This movement from one side to the other generates the potential difference. In this case, the permeability is lower than in the porous membranes but can be improved by elevated operating temperature.

Moreover, this membrane is further divided into two categories: mixed ion-electron conducting membranes (MIECs) and ion conducting membranes (or ceramic membranes). These two dense membranes are distinguished by their conductivities. For MIEC materials, they exhibit both high electronic and ionic conductivities, whereas solid electrolyte or oxygen ion conducting membranes have predominant high ionic conductivities but very low electronic ones.

A mixed ion-electron conducting membrane and ion conductive one are shown in Figure 1.2 and Figure 1.4, respectively. Figure 1.2(a) demonstrates a single phase MIEC membrane and Figure 1.2(b) displays a dual-phase MIEC membrane which is a mixture of an electron conducting and an ion conducting phase.

(a) (b)
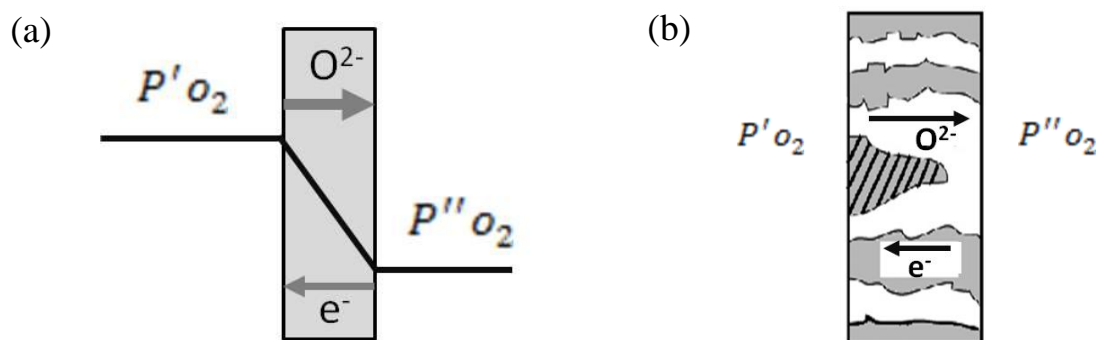
Figure 1.2 The representative MIEC dense membranes (a) single phase and (b) dual-phase for oxygen transport [11-12].

When a MIEC dense membrane was used in the separation of oxygen (as illustrated in Figure 1.3), if the membrane is dense, no cracks and connected-through porosity, the direct transport of oxygen molecules (O_2) is blocked. Nevertheless, under the driving force of a gradient of oxygen partial pressure across the membrane, oxygen can transport through the membrane.
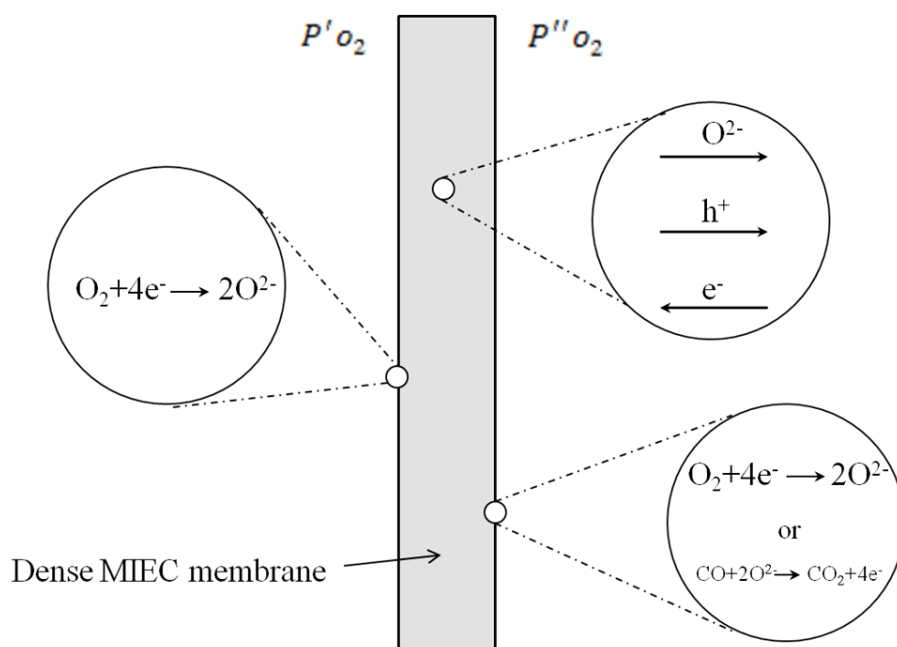
Figure 1.3 A schematic representation of surface reaction and transport mechanism across a mixed ion-electron conducting membrane [10].

At the side with high partial pressure of oxygen (P'_{O_2}), oxygen molecules are dissociated and converted into oxide ion species (O^{2-}). Hence, these oxide ions are incorporated into the oxygen lattice occupying at vacant sites as represented with following Kröger-Vink notation:

$$\frac{1}{2}O_2 + V_O^{\bullet\bullet} + 2e^- \rightarrow O_O^{\times} \tag{1.1}$$

Transportation by a hopping mechanism, the oxygen ions are transported from the high oxygen partial pressure to the low oxygen partial pressure. At this side, the recombination of oxygen ions to oxygen molecules occurs, subsequently desorbing into gas phase. Considering in terms of neutrality, the flux of oxygen ions is balanced by simultaneous electron transport.

Figure 1.4 represents a solid electrolyte coupled with two electrodes. The electrons pass through an external circuit, providing the electricity.
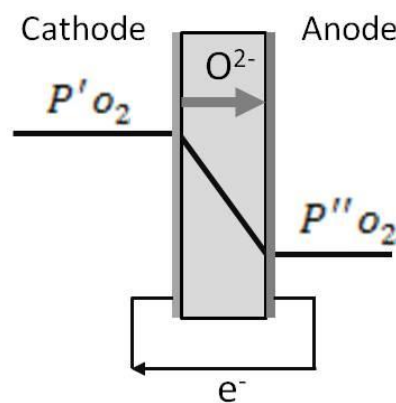
Figure 1.4 The representative oxygen ion conducting membranes for oxygen transport [11-12].

Therefore, solid electrolytes are one of the dense materials conducting only ionic species in solids as an electric charge carrier, exhibiting an ionic conductivity. They also exhibit to some extent the electronic conductivity in low level. In other words, oxide-ion electrolytes are oxides and the limitation on their

ability to remain electronic insulators related to each application. There are numerous application of solid electrolytes in various research fields such as solid oxide fuel cells (SOFCs), gas sensors, oxygen separation membranes, fast ion conductors, etc. The well-known electrolyte used in SOFCs is yttria-stabilized zirconia (YSZ) but it needs high operating temperatures (800-1,000°C) to obtain a sufficient ionic conductivity.

On the other hand, the general design requirements for the electrolyte materials are [12]:

- ionically conductive;
- electronically insulating;
- chemically stable at the operating temperatures;
- chemically stable in oxidizing and reducing atmosphere;
- gas tight/free of porosity;
- electrodes compatibility;
- inexpensive materials.

Hence, the development of the novel electrolyte which can operate at lower temperatures with high ionic conductivities became attractive. To reduce the operating temperature, firstly, the reduction of resistance of the electrolyte should be considered. One achieve approach is to use thin film of YSZ as electrolyte. Another alternative is to use other solid electrolytes with higher ionic conductivity. Perovskites family is one of the well-known solid electrolyte materials which have much attention because of their high ionic conductivity, stability in thermal and chemical atmospheres and exhibited higher ionic conductivity when compared with YSZ [11] which was further mentioned.

1.3.2 Electrodes

The sensing electrodes promote the electrochemical reactions on their surfaces. For gas sensors, the solid electrolytes are coated with the sensing electrodes as anode and cathode on each side. The electrochemical reaction occurs at anode is

the oxidation reaction, while the reduction reaction take places at cathode. The output of the electrochemical cell is directly related to the concentration or partial pressure of gaseous species. The general requirements of anode and cathode materials are summarized in Table 1.5.

Table 1.5 Design requirements for the anode and cathode [13].

Anode	Cathode
- electrically conductive; - high electrocatalytic activity; - avoid coke deposition; - stable in a reducing atmosphere; - chemically compatible with neighboring cell compartment; - fine particle size; - thin enough to avoid mass transfer losses but thick enough to provide area and distribute current.	- high electronic and ionic conductivity; - chemically compatible with neighboring cell compartment; - thin and porous; - stable in the oxidizing environment; - catalyze the dissociation of oxygen molecule; - adhesive to electrolyte surface.

1.3.2.1 Gas diffusion electrodes

In operating mode, electrodes have to be fixed on both sides of ion conducting membrane (solid electrolytes), not only closely contact to membrane but also to current collectors. These electronic current collectors are directly connected to the external circuits.

The electrodes functions are:
- catalysts for the electrochemical reactions;
- electronic conduction;
- ionic conduction;
- transport non-charged species towards the reaction sites via pore diffusion inside the electrode structure.
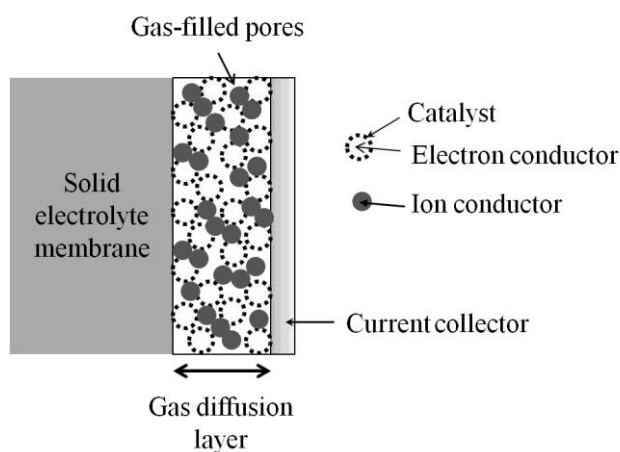
Figure 1.5 The representation of gas diffusion electrodes (GDE) [11].

A schematic illustration of a typical gas diffusion control is shown in Figure 1.5. The optimized GDE design requires a balance of the different functions. In general, it can be achieved via preparation of a mixture of particles of membrane materials, electron conducting particles and catalytic particles.

1.3.3 Types of electrochemical sensors

The highly sensitive and selective detection of various gases has become increasingly important especially for monitoring exhaust gases and environmental pollutants. Recently, various electrochemical gas sensors using solid electrolytes have been developed. These sensors are classified into three main groups based on the gas detection principles.

1.3.3.1 Equilibrium potentiometric sensors [14-19]

Usually, the galvanic cells consisting of a solid electrolyte and a couple of electronically conductive electrodes are used for potentiometric measurement. The electrodes are called the reference electrode and working or sensing electrode and chemical potentials are formed at electrode-electrolyte interfaces. When an equilibrium with the ambient gas is established, the chemical potentials are generated at the electrolyte-reference interface and at the electrolyte-sensing electrode interface.

The measured signal is the potential difference between the working and reference electrode known as an electromotive force (EMF) of the galvanic cell under condition of no current flow. The EMF is defined in term of gas partial pressure through Nernst equation:

$$EMF = E_0 + \frac{RT}{nF} ln \frac{P_w}{P^0}$$ (1.1)

where,

$E_0 =$ the EMF at a standard pressure,

$R =$ the gas constant,

$F =$ the Faraday constant,

$n =$ the number of electrons involved in the electrochemical reaction of the gas molecule,

$T =$ the absolute temperature,

$P_w =$ the gas partial pressure at the working electrode and

$P^0 =$ the standard pressure.

Generally, a working electrode's potential depends on the concentration of the investigated gas in contrast with a reference electrode [15].

The combination of various types of electrodes provides the different operating performances for the potentiometric electrochemical sensors. The group of these sensors can be further classified into three types: type I, type II and type III sensors from the electrochemical reactions between the solid electrolyte and the target gas following the classification of equilibrium potential-type sensors by Weppner [16].

- *Type I sensor* consists of two electrodes attached on the both sides of the solid ionic conductive electrolyte. The measured EMF is the chemical potential difference of neutral components which related

to the mobile ions in the solid electrolyte. Type I sensor is restricted to the detection of the species corresponding to the mobile ionic species in the solid electrolyte. The schematic representation of this type of potentiometric sensor was shown in Figure 1.6.
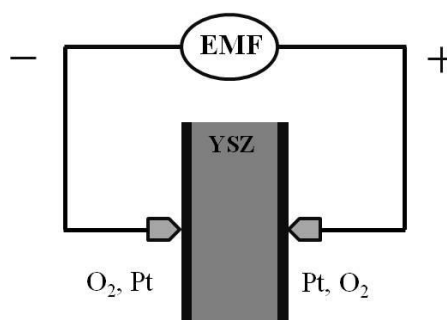
Figure 1.6 Schematic representation of type I sensor. $(-)O_2$, Pt | YSZ | Pt, $O_2(+)$

- *Type II sensor* provides the detection of the chemical species other than the mobile species in the solid electrolyte. The EMF is a measure of chemical potential of the immobile component. However, this type of sensor is confined by the limited number of appropriate solid ionic conductors corresponding to the immobile species with the known equilibrium reactions. Figure 1.7 displayed the schematic representation of type II potentiometric sensor.
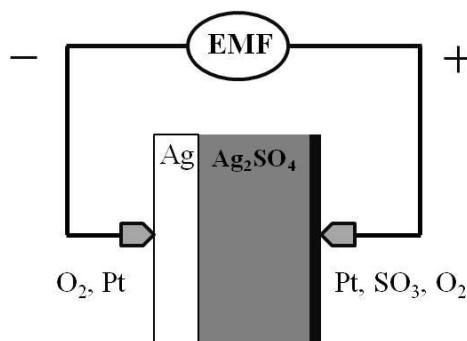
Figure 1.7 Schematic representation of type II sensor. $(-)$Ag, O_2, Pt | Ag_2SO_4 | Pt, SO_3, $O_2(+)$

- *Type III sensor* is consisted of the electrode and ionic junction between electrolyte and auxiliary phase. The ionic junction permits the measurement of the concentration of chemical species that does not present in the solid electrolyte. The auxiliary phase should be porous and is dispersed into the electrolyte at measuring side in order to provide the close contact of all phases for fast equilibration. This type of sensor provides more feasibility on various sensor designs between the different auxiliary materials and electrolytes. Figure 1.8 showed the schematic structure of type III potentiometric sensor.
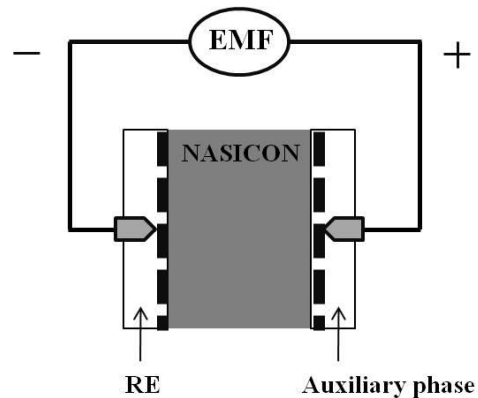
Figure 1.8 Schematic representation of type III sensor. (-)Na_2ZrO_3 + ZrO_2, Au ∣ NASICON ∣ Au, $NaNO_3$(+)

The typical cell structures of each divided equilibrium potentiometric sensor are shown in Table 1.6.

Table 1.6 Classification of equilibrium potentiometric sensors [17].

Sensing principle	Typical cell structure (RE|solid electrolyte[a]|SE)	Gas-sensing reaction
Type I	O_2,Pt | YSZ | Pt,O_2	$\frac{1}{2}O_2 + 2e^- \leftrightarrow O^{2-}$
Type II	CO_2 , O_2, Au | K_2CO_3 | Au, $CO_2 + O_2$	$2K^+ + CO_2 + \frac{1}{2}O_2 + 2e^- \leftrightarrow K_2CO_3$
Type III	O_2, Au | NASICON | $NaNO_2$ | Au, $NO_2 + O_2$	$Na^+ + NO_2 + e^- \leftrightarrow NaNO_2$

[a] YSZ: Yttria stabilized zirconia (oxygen ion conductor; O^{2-}), NASICON: $Na_3Zr_2Si_2PO_{12}$ (sodium ion conductor, Na^+), RE: Reference electrode, SE: Sensing electrode.

1.1.3.2 Non-equilibrium potentiometric (mixed potential) sensors [14, 17, 20-23]

The measured signal of mixed potential gas devices is not the equilibrium electromotive force (EMF) based on Nernst's equation. They measured mixed potential generating by the two electrochemical reactions which simultaneously take place in the opposite direction at the electrode-electrolyte interface. One is the electrochemical reaction of target gas so-called cathodic reaction of target gas. Another one is the electrochemical reaction of oxygen or anodic reaction of oxygen (oxygen reduction).

To understand the mixed potential mechanism, a typical representation of a mixed potential sensor is illustrated in Figure 1.9. A galvanic cell structure of this sensor type can be described as follows:

electrode 1 | solid electrolyte | electrode 2

where both electrodes are exposed to the gas mixture containing oxygen and an oxidizable or reducible gas. The different potentials develop on each electrode due to

the differences in electrokinetic redox rates of the electrodes. The devices response voltage is the difference in mixed potential attained by each electrode.
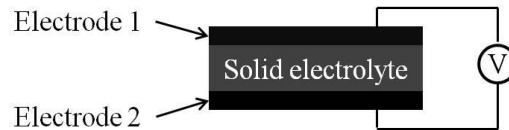
Figure 1.9 A schematic representation of a mixed potential sensor fabrication from a solid electrolyte coupled with porous electrode materials. Both electrodes are exposed to a mixture of oxidizable or reducible gas and oxygen.

The concept of mixed potential was introduced to describe non-ideal behavior of the typical oxygen sensor consisting of stabilized zirconia (YSZ) and Pt electrodes in the mixed gases of air and oxidizable gases by Fleming [24]. Fleming explained the deviation of ideal correlation between EMF and air-oxidizable gas ratio by investigation the chemical and electrochemical phenomenon occurring at Pt-sensing electrodes. Assuming a case where CO as an oxidizable gas mixed with oxygen as sample gas, the presence of CO could affect the oxygen sensor voltage in two ways.

First, CO may deplete the local concentration of O_2 at the Pt-sensing electrode surface according to the following chemical reaction. For this reaction, Pt electrode works as a catalyst.

$$CO' + \frac{1}{2}O_2' \rightarrow CO_2' \qquad (1.2)$$

Where O_2', CO' and CO_2' denote gases in the neighborhood of the three-phase interface. The cathodic reaction is

$$O_2' + 4e^- \rightarrow 2O^{2-} \qquad (1.3)$$

The sensor structure is simply an oxygen concentration cell as follows:

$$P'_{O_2}, \text{Pt} \mid \text{YSZ} \mid \text{Pt}, P_{O_2} \tag{1.4}$$

where P'_{O_2} is the partial pressure of O'_2 which presents after the completion of the reaction.

Second, the direct participation of CO in the following electrochemical process:

$$\text{CO}' + \text{O}^{2\text{-}} \rightarrow \text{CO}'_2 + 2e^- \tag{1.5}$$
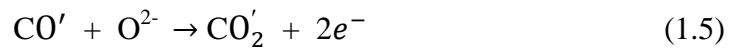
In this case, the sensor structure is

$$P'_{CO}, \text{Pt} \mid \text{YSZ} \mid \text{Pt}, P_{O_2} \tag{1.6}$$

At the sensing electrode surfaces, the electrochemical oxidation (1.5) and reduction (1.3) take place simultaneously and form a local cell. When the rates of these two reactions are equal to each other, the potential of the sensing electrodes is a mixed-potential.

In accordance with the Butler-Volmer equation, the cathodic and anodic currents densities can be expressed as Tafel-type behavior:

$$i_{O_2} = i^0_{O_2} \exp[\text{-}4\alpha_1 F(E - E^0_{O_2})/RT] \tag{1.7}$$

and

$$i_{CO} = i^0_{CO} \exp[2\alpha_2 F(E - E^0_{CO})/RT] \tag{1.8}$$

respectively, where $i^0_{O_2}$ and i^0_{CO} are the exchange current densities for cathodic and anodic reaction, respectively, α is transference coefficient, F is the Faraday constant,

E is the electrode potential, E^0 is the equilibrium electrode potential at a reference state, R is the gas constant and T is the absolute temperature. At equilibrium, the kinetic rates of reaction (1.7) and reaction (1.8) are the same. The difference between E^0_{CO} and $E^0_{O_2}$ can be expressed as

$$\Delta E^0 = -\frac{\Delta G^0}{2F} - \frac{RT}{2F} ln \frac{[CO_2]}{[CO][O_2]^{1/2}} \qquad (1.9)$$

where ΔG^0 is the standard Gibbs energy change of reaction (1.2). At equilibrium, the mixed potential is generated under the condition $i_{O_2} = i_{CO}$ from equation (1.7) and equation (1.8). It can be written as

$$E_{mix} = E^0 + \frac{RT}{2F} ln \frac{P_{CO}}{[O_2]} \qquad (1.10)$$

Hence, the mix potential is expected to have a logarithmic dependence on the concentration of CO for a constant concentration of O_2. Here, $E^0 = \alpha_1 E^0_{O_2} + \alpha_2 E^0_{CO}$ is assumed to be constant. Nevertheless, since the concentration of adsorbates on the real electrode can be a function of the overpotential ($\eta_{CO} = E_{mix} - E^0_{CO}$ or $\eta_{O_2} = E^0_{O_2} - E_{mix}$), the slope deviates from the theoretical value of $RT/2F$.

However, if E_{mix} is close to the equilibrium oxygen potential so that the anodic reaction of oxygen takes place at a low overpotential and the reduction reaction of CO occurs at a high overpotential, the kinetic rate of anodic reaction may be presented by the low overpotential linear approximation of Butler-Volmer equation can be written as

$$i_{O_2} = i^0_{O_2} 4\alpha_1 F(E - E^0_{O_2})/RT \qquad (1.11)$$

while the kinetic rate of cathodic reaction may be explained in case of a diffusion based mass transport limited reaction kinetics due to a high overpotential as

$$i_{CO} = 2FAD_{CO}\frac{P_{CO}}{RT\delta} \tag{1.12}$$

where A is the electrode area, D_{CO} is the diffusion coefficient of CO and δ is the diffusion boundary layer thickness. Combining equation (1.11) and equation (1.12) for $i_{O_2} = i_{CO}$ yields

$$E_{mix} = E_{O_2}^0 - \frac{AD_{CO}}{2i_{O_2}^0\alpha_1\delta}P_{CO} \tag{1.13}$$

and then gives a linear relationship between CO concentration and the mixed potential (E_{mix}).

In summary, there are two modes of dependence for concentration of reacting gas on mixed potential: logarithmic dependence and linear dependence. When kinetic are investigated by the electrochemical reaction occurs at the electrode, logarithmic dependence will appear. Conversely, if the mixed potential is determined by the simultaneously involved operation of both slow mass transport of chemical species toward electrode for one electrochemical reaction with a large overpotential and Tafel-type kinetics for another reaction with negligible overpotential, linear dependence will be met.

1.1.3.3 Amperometric sensors [9, 14-15, 23, 25-26]

Since a potentiometric sensor exhibits a logarithmic behavior to the gas concentration, its sensitivity at high concentration is rather low. Amperometric sensors feature a linear dependence of electrical output that is more suitable for detection of high gas concentrations.

In amperometric mode, a constant voltage is applied across the electrolyte to generate a current. The magnitude of current is limited by availability of the gaseous species for the electrochemical reaction on the electrolyte surface. A typical structure of an amperometric oxygen sensor with a hole as the diffusion barrier is illustrated in Figure 1.10

.
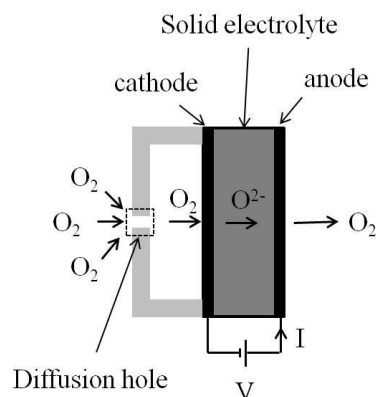
Figure 1.10 A schematic amperometric sensor based on oxygen pumping with a diffusion hole barrier [9, 14-15].

The sensor consists of a pumping cell and a diffusion hole barrier limiting the oxygen-transfer rate from the ambient atmosphere to the cathode. An external voltage is applied across the electrochemical cell.

In case of an oxygen ion conducting electrolyte, the following electrochemical reaction occurs at the cathode (negative terminal of the external voltage):

$$O_2(gas) + 4e^- \text{ (electrode) } \rightarrow 2O^{2-} \text{ (electrode)} \qquad (1.14)$$

The generated oxygen ion (O^{2-}) migrates across the electrolyte to the anode (positive terminal of the external voltage) where they recombine to give oxygen molecules (O_2) in an ambient gas:

$$2O^{2-} \text{ (electrode) } \rightarrow O_2 \text{ (gas) } + 4e^- \text{ (electrode)} \qquad (1.15)$$
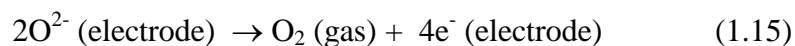
In other words, oxygen molecules are reduced to oxygen ions at the cathode, and then are pumped across the electrolyte to the anode where their re-oxidation to oxygen molecule occurs.

The typical *I-V* characteristic response of an amperometric sensor is shown in Figure 1.11. Depending on the ratio pumping rate to the oxygen diffusion flux through the aperture, there are three regions of *I-V* characteristics normally arise. The voltage *V* obeys a relation:

$$V = IR + \frac{RT}{4F} \ln \frac{P_{O_2}(ambient)}{P_{O_2}(cathode)} \tag{1.16}$$
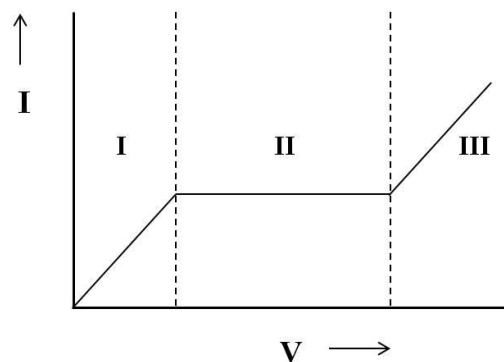
Figure 1.11 Typical *I-V* characteristic response of an amperometric sensor [14].

At region I (low voltage) where the pumping rate is less than diffusion flux, then $P_{O_2}(ambient) = P_{O_2}(cathode)$, the current increases linearly with the voltage as $V = IR$. When the pumping increases to exceed the diffusion flux of oxygen through the aperture, the current reaches a steady state (region II) that is determined by the rate of arrival of oxygen from the ambient atmosphere through the hole to the electrode written as:

$$J_{O_2} = \frac{i}{4F} = \frac{D_{O_2}[c_{O_2}(\delta) - c_{O_2}(0)]}{\delta} \approx \frac{[D_{O_2}P_{O_2}]}{RT\delta} \tag{1.17}$$

where δ relates to the effective diffusion distance for oxygen and $c_{O_2} = P_{O_2}/RT$ has been used. If the applied voltage is high enough (normally 0.5-1.5 V), the oxygen partial pressure at the cathode will decrease to nearly zero ($c_{O_2} \approx 0$) as shown in equation (1.17). Therefore, the pumping current at steady state depends linearly on the oxygen partial pressure in the ambient atmosphere. However, the increasing voltage is

compensated by the decreasing oxygen partial pressure at the cathode for a constant limiting current. When the voltage increases to region III, the electronic conduction gives rise a further increasing current. In general, the limiting current-type sensor is operated in the region II where the steady state current can be obtained.

Depending on the geometrical parameters of the diffusion barrier and oxygen concentration, the limiting current is defined by Fick's first law of diffusion, the ideal gas equation, and Faraday's law as:

$$I_{lim} = 4FJ_{O_2} = -\frac{4FD_{O_2}AP_T}{RTl}\ln\left(1 - x_{O_2}\right) \qquad (1.18)$$

where I_{lim} is the limiting current, F is the Faraday's constant, D_{O_2} is the diffusion coefficient of gaseous O_2 (bulk diffusivity), A is the area of the diffusion hole, P_T is the total pressure in the ambient, R is the gas constant, T is the operating temperature, l is the length of the diffusion hole, and x_{O_2} – the mole fraction of oxygen. For small values of oxygen mole fraction, the logarithm becomes linear and I_{lim} can be evaluated by:

$$I_{lim} = -\frac{4FD_{O_2}Ac_{O_2}}{l} \qquad (1.19)$$

where c_{O_2} is the oxygen concentration.

1.4 Perovskite oxides (ABO₃)

The mineral perovskite (CaTiO₃; calcium titanate) was first discovered from samples found in the Ural Mountains by Gustav Rose in 1839 and is named after a Russian mineralogist, Count Lev Aleksevich von Perovski (1792-1856). The name "Perovskite" is used to classify compounds having the same type of crystal structure as CaTiO₃ [27]. A large attention has been paid to the perovskite-type oxides because of their intriguing properties. These compounds are widely used as sensors and

catalyst electrodes in fuel cells application because they exhibit both electronic and ionic conductivities (mixed ionic-electronic conductors; MIECs)

1.4.1 Structure of perovskite oxides [28-29]

The ideal structure of perovskite oxides is cubic. The typical chemical formula is ABO_3. A is the larger cation occupying in the middle of the cube resulted in 12-fold coordination site with oxygen while B is smaller cation and formed three-dimensional network of corner sharing BO_6 octahedra. The ideal cubic perovskite structure is shown in Figure 1.12.
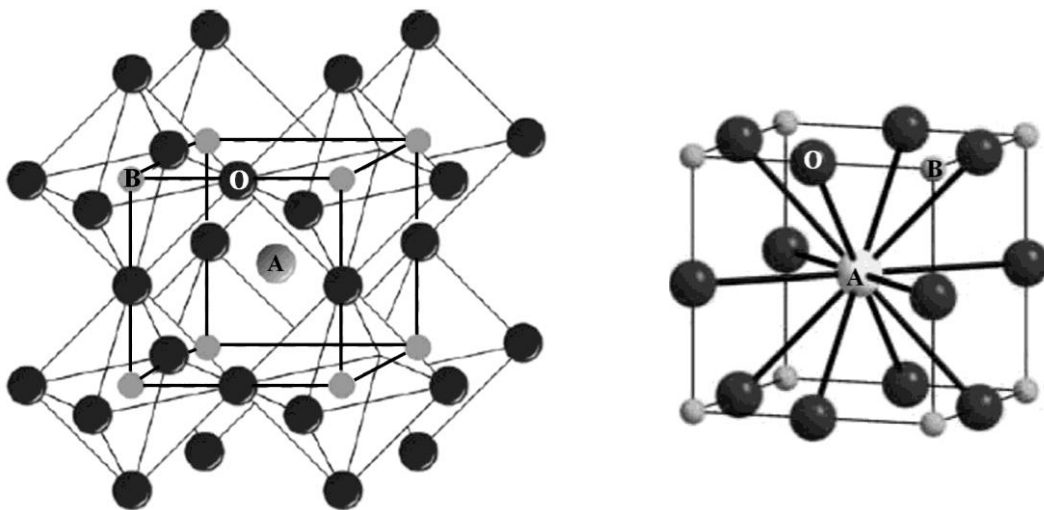
Figure 1.12 The ideal cubic perovskite structure ABO_3.

In this structure, the atoms are touching one another. The A-O distance is $a/\sqrt{2}$ where a is the cubic unit cell parameter while the B-O distance is equal to $a/2$ and the following relationship between the ionic radii holds is shown in equation (1.4)

$$r_A + r_O = a/\sqrt{2} \qquad (1.20)$$

$$r_B + r_O = a/2 \tag{1.21}$$

and

$$a = \sqrt{2}(r_A + r_O) = 2(r_B + r_O) \tag{1.22}$$

hence,

$$r_A + r_O = \sqrt{2}(r_B + r_O) \tag{1.23}$$

where r_A, r_B and r_O are relative ionic radii of the A and B cations and the oxygen ion, respectively.

The perovskite structure is known to be very flexible and the A and B cations can be varied by partial substitution with other cations (same or different in sizes and charges) leading to the large number of perovskite or related structures. Many perovskites are distorted from ideal cubic structure.

Goldschmidt proposed a tolerance factor (t) to evaluate the stability of perovskites. It is based on ionic radii and defined by the equation (1.24).

$$t = \frac{(r_A + r_O)}{\sqrt{2}(r_B + r_O)} \tag{1.24}$$

The ideal cubic perovskite structure is found in a few cases for t-values very close to 1.00 at high temperature. However, the cubic perovskite structure is also found for $0.95 \leq t \leq 1.04$. The lattice parameter a of cubic perovskite structure is determined by A and B atomic size and geometric structure characteristics.

The schematic view of the (110) plane section of ideal cubic ABO_3 perovskite structure with different tolerance factors is shown in Figure 1.13. From equation (1.24), in case of $t < 1$, the value of $\sqrt{2}(r_B + r_O)$ is greater than that of $(r_A + r_O)$ suggesting that the A cation is smaller than its cavity and/or the B cation is too large for its hole. Hence, the cubic lattice parameter can be described as $a = 2(r_B + r_O)$.

(a) $t < 1$

(b) $t = 1$

(c) $t > 1$
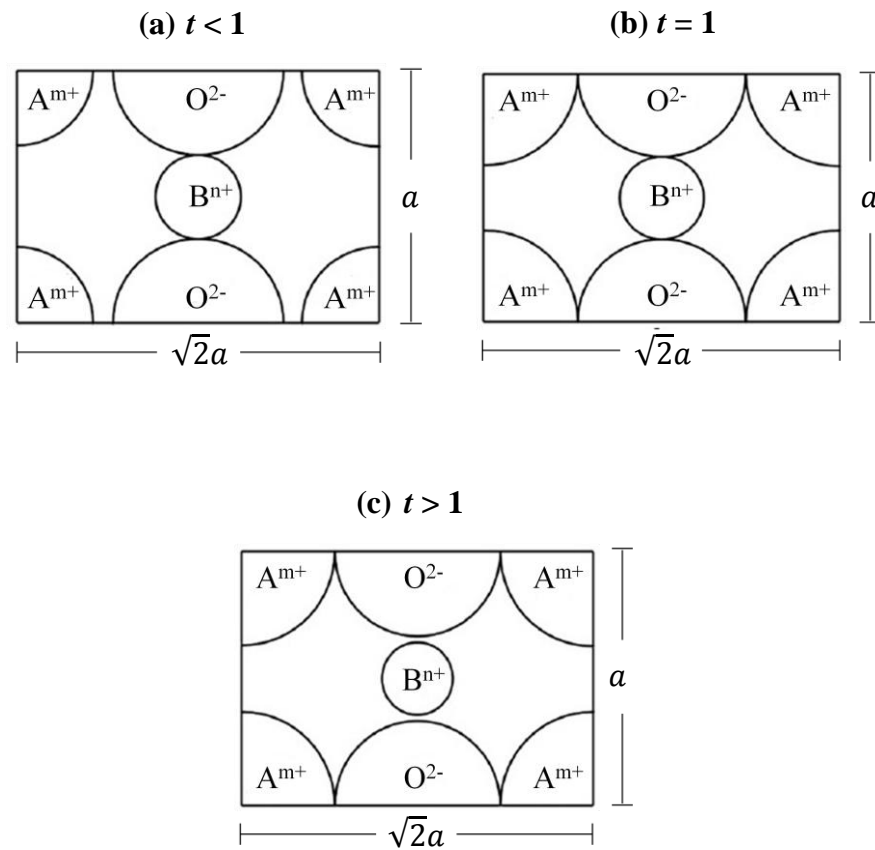
Figure 1.13 The section of the (110) plane of ideal cubic ABO_3 perovskite structure with different tolerance factors: (a) $t < 1$; (b) $t = 1$ and (c) $t > 1$ [29].

In a similar way, the cubic perovskite lattice parameter with $t > 1$ can be expressed as $a = \sqrt{2}(r_A + r_O)$. Table 1.7 shows the summary of the lattice parameter of cubic perovskite structure with different t-values.

Table 1.7 The summary of the lattice parameter of cubic perovskite structure with different tolerance factors [29].

Tolerance factor (t)	Lattice parameter; a
$t < 1$	$a = 2(r_B + r_O)$
$t = 1$	$a = \sqrt{2}(r_A + r_O) = 2(r_B + r_O)$
$t > 1$	$a = \sqrt{2}(r_A + r_O)$

In addition, lower values of tolerance factor will lower the crystal symmetry. This deviation gives rise to orthorhombic structure. If t-values are in the range $1.00 < t < 1.13$, the compositions will exhibit hexagonal symmetry.

1.4.2 Oxygen nonstoichiometry in perovskites [28]

The sum of charges of A and B cations equals to total charge of oxygen anion (electroneutrality) is one of the other requirements to be fulfilled apart from ionic radii conditions. This is achieved through the appropriate charge distribution of the form $A^{1+}B^{5+}O_3$, $A^{2+}B^{4+}O_3$ or $A^{3+}B^{3+}O_3$. Besides this, partial substitution of A and B ions is permitted yielding a plenty of perovskite-type compositions. Oxygen vacancies are achieved by substitution of cations with similar sizes but different valances. They are more ordinary than those involving cationic vacancies. Nevertheless, oxygen excess nonstoichiometry in perovskite oxides is not as usual as anion-deficient nonstoichiometry probably because introduction of interstitial oxygen in perovskite structure is thermodynamically unfavorable. In terms of a defect model, oxygen excess nonstoichiometry can be occurred based on two assumptions. First, because the trivalent cation vacancies result in a large electronic imbalance and local lattice distortion, they do not stay close to each other. Second, as the formation of cation vacancies, a nonbonding O2p level is formed by the oxide ions around the vacancies. This nonbonding O2p level serves as the hole-trap. Applying this structure, nonstoichiometry of the oxygen-deficient composition was explained by the random distribution of oxide-ion vacancies. The general formula of oxygen-deficient perovskite oxides is $A_nB_nO_{3n-1}$, in which the stacking manner depends on the size, electronic configurations and coordination numbers of A and B cations.

1.4.3 Ionic conduction in perovskite oxides

The perovskite-type oxides ABO_3 are stable because of their balanced geometrical array of element atoms and their valances. The deviation from ideal cubic perovskites is allowed keeping the original structure. Therefore, nonstoichiometric perovskite oxides, including oxygen-deficient $ABO_{3-\delta}$, A-deficient $A_{1-\delta}BO_3$ or

B-deficient $AB_{1-\delta}O_3$ occur, where δ denotes the number of deficient atoms per unit formula. In the first case, oxygen vacancy would be formed and the latter two cases, so-called cation nonstoichiometry, the formation of some defective lattice appeared because of deviation from stoichiometric composition (A:B = 1:1). Moreover, the partial substitution in A- or B-site with M atom results in the formation of $A_{1-x}M_xBO_3$ or $AB_{1-x}M_xO_3$. If the valence of M is different from A or B, lattice defects will be formed to maintain electroneutrality of the crystal.

Several kinds of ions have been found to be mobile in perovskite and perovskite-related compounds. Oxide ions and protons are the representative conducting ions in perovskite oxide found in many researches. Of these, oxide ion conductors are the best well-known and the conduction of oxide ion in various kinds of perovskite and perovskite-related compounds has been investigated. The most convenient method to confirm ionic conduction in the electrochemically conductive oxides is to examine the electromotive force (EMF) of an electrochemical oxygen concentration cell:

$$\text{Pt, O}_2 \ (P_{O_2}(1)) \ | \ \text{oxide sample} \ | \ \text{O}_2 \ (P_{O_2}(2)), \ \text{Pt} \qquad (1.25)$$

using oxygen-ion-conducting oxide as electrolyte. The schematic of the oxygen concentration cell is shown in Figure 1.14.
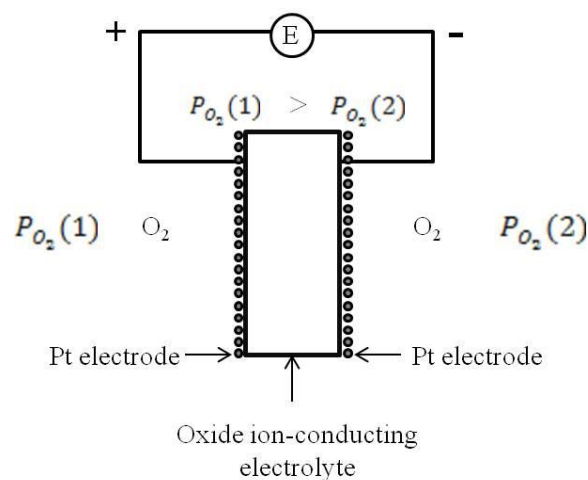
Figure 1.14 A schematic of an electrochemical oxygen concentration cell [30].

Figure 1.14 shows a schematic of an electrochemical oxygen concentration cell consisting of a dense ionic conductor as electrolyte with porous Pt electrode. When the two sides of the cell are exposed to different oxygen partial pressure $P_{O_2}(1)$ and $P_{O_2}(2)$ at elevated temperatures, an open-circuit develops between the Pt electrodes given by Nernst equation:

$$E_0 = \frac{RT}{4F} ln \frac{P_{O_2}(1)}{P_{O_2}(2)} \tag{1.26}$$

If the observed EMF is close to the theoretical value E_0, the oxide can be regarded as ionic conductor. When EMF is not zero but smaller than E_0, the observed value would be partially ionic and electronic.

As mentioned above, many perovskite-type oxides can deviate from their stoichiometric composition resulting in the formation of excess electrons or electron holes. This brings about n-type or p-type electronic conduction. Hence, it should be noted that perovskite-type oxides have electronic conduction and the ionic conduction is often accompanied by electronic conduction.

Generally, at elevated temperature, the electronic conductivity of oxide electrolyte is influenced by partial pressure of oxygen in the atmosphere. N-type electronic conductivity, σ_n, increases with decreasing oxygen partial pressure. On the contrary with p-type electronic conductivity, σ_p increases with increasing partial pressure of oxygen. The oxygen partial pressure P_{O_2} dependence of σ_n or σ_p is given by the following equation (1.27) and (1.28).

$$\sigma_n = \sigma_n^o \exp P_{O_2}^{-1/n} \tag{1.27}$$

and

$$\sigma_p = \sigma_p^o \exp P_{O_2}^{-1/n} \tag{1.28}$$

where n is natural number and σ_n^0 and σ_p^0 are the constants which are dependent of P_{O_2}. For many oxide electrolytes, the ionic conductivity σ_i is independent of partial pressure of oxygen. Thus, the total conductivity σ is expressed as in equation (1.29).

$$\sigma = \sigma_i + \sigma_n^0 \exp P_{O_2}^{-1/n} + \sigma_p^0 \exp P_{O_2}^{-1/n} \qquad (1.29)$$

The dependence of conductivity on partial pressure of oxygen is shown in Figure 1.15.
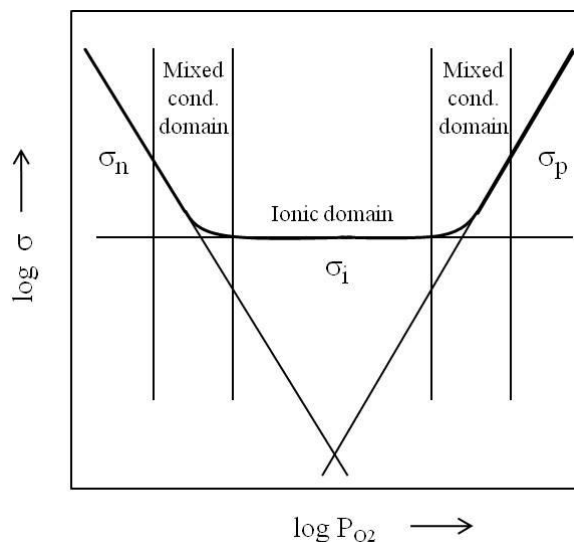
Figure 1.15 Dependence of conductivity on partial pressure of oxygen [30].

The hatched regions illustrate the mixed conduction domains and between them it is an ionic conduction domain. The outer sides of the mixed conduction domains are the electronic conduction regions.

1.4.4 Oxygen transport processes [31]

The perovskite oxides are found to be good mixed ionic electronic materials. Because of their mixed conducting property, these materials can be used as membranes for oxygen separation. Based on the difference in the partial pressure of

oxygen between the feed side and the permeate side, temperature and membrane's ambipolar conductivity, oxygen migrates from the feed side $(P'o_2)$ through a dense mixed conducting material to the permeate side $(P''o_2)$. The overall oxygen transport processes occurs in five steps as follows [31-32]:

(i)   mass transfer of gaseous oxygen from the $P'o_2$ feed stream inlet to the membrane surface (advection and diffusion)

(ii)   adsorption onto the membrane surface, dissociation and ionization of oxygen molecules and incorporation of the oxygen ions into the lattice vacancies (feed side surface-exchange reaction)

(iii) transport of lattice oxygen ions through the membrane (simultaneous bulk-diffusion of charged species and electron/electron holes in the bulk phase)

(iv)   recombination of lattice oxygen ions to oxygen molecules and desorption from the membrane surface into the gas phase (permeate side surface-exchange reaction)

(v)   gaseous oxygen mass transfer from the membrane surface to the $P''o_2$ permeate stream outlet (diffusion and advection)

The progressive steps involved in oxygen transport during oxygen permeation are shown in Figure 1.16.

Feed side (inlet)

Permeate side (outlet)
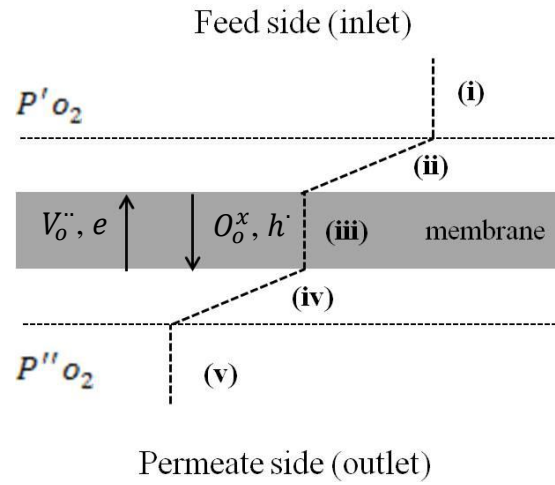
Figure 1.16 A multi-step mechanism of oxygen transport across the membrane: (i) gas phase mass transfer (diffusion from the high oxygen partial pressure-side); (ii) surface exchange (adsorption, ionization and incorporation); (iii) bulk diffusion; (iv) surface exchange (association and desorption) and (v) gas phase mass transfer (diffusion to the low oxygen partial pressure-side) [31].

The surface-exchange reactions occurred in step (ii) and (iv) can be described as follows:

$$\tfrac{1}{2}O_2 + V_o^{\cdot\cdot} \quad \rightarrow \quad O_o^x + 2h^{\cdot} \tag{1.30}$$

and

$$O_o^x + 2h^{\cdot} \quad \rightarrow \quad \tfrac{1}{2}O_2 + V_o^{\cdot\cdot} \tag{1.31}$$
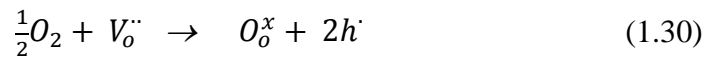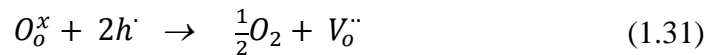
where $V_o^{\cdot\cdot}$ is the oxygen vacancy, O_o^x is the lattice oxygen ion, $h^{\cdot}$ is the electron holes. At steady state, the oxygen permeation flux can be expressed by the Wagner equation:

$$J_{O_2} = \frac{(RT\sigma_{amb})}{(4F)^2 L} \ln \frac{P'_{O_2}}{P''_{O_2}} \tag{1.32}$$

where J_{O_2} is the oxygen flux through unit area, R is the ideal gas constant, T is the absolute temperature, L is the membrane thickness, F is the Faraday's constant, P'_{O_2} is the high oxygen partial pressure at the feed side, P''_{O_2} is the low oxygen partial pressure at the permeate side. The ambipolar conductivity (σ_{amb}) is defined as:

$$\sigma_{amb} = \frac{\sigma_e \sigma_i}{(\sigma_e + \sigma_i)} \tag{1.33}$$

where σ_e and σ_i are the electronic and ionic contribution to the total conductivity, respectively.

When oxygen transport is limited by the rate of oxygen exchange on the surface of membrane, increasing surface area is an alternative to enhance the oxygen permeate flux. One of the successful enhancement is to polish the membrane surface resulted in the roughening surface which increases surface/volume ratio. Further effective method to enhance the surface area is coating the porous layer on the top of the dense mixed-conducting membrane. This option can promote the adsorption and dissociation of oxygen and enhance the oxygen permeate flux. In addition, under bulk diffusion control, the oxygen permeate flux can be correlated with the inverse of membrane thickness. Therefore, decreasing the membrane thickness can increase the oxygen flux when oxygen transport is limited by bulk diffusion.

1.5 Literature reviews

Rusmiati et al. [33] synthesized $La_{0.8}Sr_{0.2}Ga_{0.8}Mg_{0.2-x}Fe_xO_{3-\delta}$ with x = 0, 0.05, 0.1, 0.15 by solid state reaction at 1,450°C and the crystal structures of these compounds were analyzed using X-rays diffractometer. The crystal structure of all samples was cubic. The cell parameters of $La_{0.8}Sr_{0.2}Ga_{0.8}Mg_{0.2-x}Fe_xO_{3-\delta}$ (x = 0, 0.05, 0.1, 0.15) were a = 3.924(1), 3.9183(7), 3.9126(1), and 3.9061(3) Å, respectively. The decreasing cell parameter resulted in the decreasing cell volume due to the increasing substitution with smaller ionic size of Fe into Mg-site.

Ishihara et al. [34] explored mixed electronic–oxide ionic conductivity in $LaGaO_3$-based oxide doped with Fe, Co or Ni. The electrical conductivity was greatly increased by doping Fe, Co, or Ni for the Ga site of $La_{0.8}Sr_{0.2}GaO_3$. Compared to the conventional mixed electronic–ionic conductors such as $LaCoO_3$, these $LaGaO_3$-based oxides exhibited a lower electronic conductivity but higher oxide ion conductivity. In particular, Fe-doped $LaGaO_3$ exhibited a high oxygen permeation rate

and stability against reduction. Consequently, higher CH_4 conversion in the partial oxidation of CH_4 was attained by using $La_{0.8}Sr_{0.2}Ga_{0.6}Fe_{0.4}O_3$ in the place of the conventional candidate material, $La_{0.6}Sr_{0.4}Fe_{0.8}Co_{0.2}O_3$, for the oxygen permeation membrane. As a result, this study revealed that $LaGaO_3$-based oxide doped with Fe, Co or Ni for Ga site is a new family of mixed electronic–oxide ionic conductors.

Ishihara et al. [35] investigated the effects of small amounts of Fe doping for Ga site in $LaGaO_3$-based oxide on oxide ion conductivity. It was found that doping a small amount of Fe is effective for improving the oxide ion conductivity in $La_{0.8}Sr_{0.2}Ga_{0.8}Mg_{0.2}O_3$ (LSGM). The highest oxide ion conductivity was exhibited at $x= 0.03$ in $La_{0.8}Sr_{0.2}Ga_{0.8}Mg_{0.2-x}Fe_xO_3$ among the Fe-doped samples.

Shaula et al. [36] measured the oxygen permeability of perovskite-type $La_{1-x}Sr_xGa_{0.8-y}Mg_yM_{0.2}O_{3-\delta}$ (x = 0-0.2, y = 0.15-0.20, M = Fe, Co and Ni). For $La(Sr)Ga(Mg)O_{3-\delta}$ (LSGM) ceramics, the oxygen transport increased in the sequence Co < Fe < Ni. The highest permeation is observed for $La_{0.9}Sr_{0.1}Ga_{0.65}Mg_{0.15}Ni_{0.2}O_{3-\delta}$ perovskite membranes, which exhibited level of the oxygen permeability similar to that of $La(Sr)Fe(Co)O_{3-\delta}$ and La_2NiO_4-based solid solutions. The average thermal expansion coefficients (TECs) of $La(Sr)Ga(Mg,M)O_{3-\delta}$ ceramics in air are in range $(11.6–18.4) \times 10^{-6} K^{-1}$ at 373–1273 K.

Can et al. [37] studied zirconia oxygen sensor for detection of CO and found that the sensor was sensitive to a small amount of CO in an O_2-containing gas stream at operating temperature lower than 550°C and within ±50 mV of the equilibrium potential. They suggested that the sensing mechanism of the sensor was due to the reduction reaction of O_2 and the oxidation reaction of CO occurred simultaneously on the sensing electrode, then a local cell was formed.

Narducci et al. [38] developed the potentiometric solid state YSZ-based sensors for CO detection. Two sensors were prepared with general structure as: M, O_2, CO|YSZ|O_2, Pt, in which M was either Pt or RuO_2. The EMF measurements incorporated with temperatures presented a linear relationship for both sensors. The

optimal working temperature at which EMF values could be used to measure CO with an accuracy better than 50% was at 420°C. Unfortunately, response time at this temperature was sufficiently low. Then, it was difficult to predict that this sensor could be used as good CO-detected devices.

Barth et al. [39] prepared the potentiometric sensors consisting of oxygen-ion conducting solid electrolyte (YSZ) cells combined with Pt reference electrodes and Fe_2O_3-Sb_2O_4 working electrodes for studying the partial oxidation of propene. They found that the working electrode acted as both electrode and catalyst during the study. Considering the catalyst's behavior, there were two different forms of surface oxygen and EMF measurement indicated that the sensor was most sensitive to the more reactive adsorbed oxygen and not lattice oxygen. In other words, the sensor would be most sensitive to the most reactive forms of oxygen on the catalyst surface as these oxygen forms were probably the most reactive forms for the electrochemical reaction.

$LaGaO_3$ (LSGM) based solid electrolyte coupled with suitable electrodes was demonstrated to be a highly sensitive hydrocarbon (C_3H_6) sensor in the temperature range of 523-673 K which was reported in 2004 [40]. The sensors were studied in the amperometric mode. Keeping Pt as the active electrode, the various inactive electrode materials were studied. It was found that $La_{0.5}Sr_{0.5}CoO_3$ (LSC55) gave the best sensitivity among the studied $LaCoO_3$ catalysts. Furthermore, it was found that the performance of the sensor with $La_{0.5}Sr_{0.5}MnO_3$ (LSM55) showed the highest sensitivity ~600 μA/decade at 623 K among all the investigated perovskite oxides for an cathode. The sensitivity of all the sensors was fast, reversible, and the current linearly increased with increasing C_3H_6 concentration. Over a broad range of oxygen concentration, the C_3H_6 sensitivity was found unaltered.

Dutta et al. [41] studied various C_3H_6 oxidation electrodes of Pt-based alloy systems using $La_{0.5}Sr_{0.5}MnO_3$ as the oxygen reduction electrode. From this study, it was found that addition of Co and subsequently cermet $(CeO_2)_{0.8}(LaO_{1.5})_{0.2}$ (LDC) produced very high sensor response and improved the performance of the sensor with respect to that using only Pt paste as the electrode. The sensors were hardly

influenced by the oxygen concentration variation (0.5-5%). At the best operating temperature (623 K) the C_3H_6 sensitivity was above 800 µA/decade, and the lowest temperature of detection was 423 K. The sensors were fast, highly selective in the presence of coexisting gases, e.g., NO, NO_2, CO and H_2, in the exhaust, and stable. Further study was performed on Fe doping at Ga site to C_3H_6 sensitivity [42]. It was found that LSGF based electrochemical sensor exhibited very high sensitivity to propene and high selective to hydrocarbons except methane. This means that this sensor can be a promising candidate for low temperature applications.

Dutta and Ishihara [43] studied an amperometric NO sensor using a $LaGaO_3$-based solid electrolyte based on the difference of catalytic activity of the electrode. It was found that oxygen pumping current increased upon exposure to NO when $Sr_{0.6}La_{0.4}Mn_{0.8}Ni_{0.2}O_3$ and $La_{0.5}Sr_{0.5}MnO_3$ (LSM55) were used as anode and cathode for NO oxidation, respectively. Effects of electrolyte on the NO sensitivity were also investigated and the sensitivity to NO becomes higher with increasing oxide ion conductivity for electrolyte. By applying $LaGaO_3$ doped with Ni or Co, the sensitivity of the sensor becomes 1842 µA per decade of NO concentration at 823 K. The oxygen pumping current linearly increased with increasing NO concentration and the sensor responded NO and recovered to the original level within 1 min. Cross-sensitivity study revealed that NO in exhaust gas can be selectively detected in the presence of coexisting gases.

Dutta and Ishihara [44] studied an amperometric NO sensor based on $La_{0.8}Sr_{0.2}Ga_{0.8}Mg_{0.1}Ni_{0.1}O_3$ (LSGMN82811) electrolyte at operating temperature 500-700°C. For the optimization of the electrodes, LSM55 was fixed as the inactive electrode and combined with $La_{0.4}Sr_{0.6}Mn_{0.8}X_{0.2}O_3$ (X = Cu, Ni, Co, Fe and Mg). The NO sensing measurement was investigated. It was demonstrated that doping of transition metal to Mn-sites significantly influenced the NO sensitivity. The highest sensitivity was achieved at 550°C with Ni doping into Mn –sites. Therefore, the optimized LSMN4682 electrode was fixed as active and further studied. The 90% response time of the sensor was achieved within 90 sec. Therefore, the characteristics response of the LSGMN82811 combined with LSM55 and LSMN4682 is fast. On the

selectivity study, the sensor was tested with CO, CO_2, C_3H_6, NO_2 and H_2. It was demonstrated that the response to other gases was not significant. Hence, it can be summarized that this sensor was stable and fast operating in the temperature range 500-700°C and very high selective to NO.

Solid-state amperometric CH_4 sensor using $LaGaO_3$-based electrolyte was investigated by Bi et al. [45]. The different electrolytes were used to study sensitivity to CH_4. It was found that the sensor sensitivity is affected by influence of electrolyte materials in the order $La_{0.9}Sr_{0.1}Ga_{0.8}Mg_{0.2}O_3$ (LSGM) = $La_{0.8}Sr_{0.2}Ga_{0.8}Mg_{0.15}Co_{0.05}O_3$ (LSGMC) > $Sm_{0.2}Ce_{0.8}O_2$ (SDC) > $Y_{0.16}Zr_{0.84}O_2$ (YSZ). Hence, LSGM was used as electrolyte and further studied on optimization of electrode materials by addition of metal mixed with La-doped CeO_2. From this study, it revealed that the CH_4 sensitivity increased in the order RuO_2 > Pd > Rh > Pt. Other study was continued on the effect of different types of oxides mixed with Pd on the sensitivity of CH_4. It was evidenced that ITO mixed with Pd displayed very large current change. Therefore, Pd-ITO was the most suitable active electrode for CH_4 sensors. The effect of inactive electrode materials on the sensitivity to CH_4 was investigated and the results showed that the sensitivity increased in the order Co_3O_4 < Ag < Au < RuO_2. It was well-known that Co_3O_4 is normally active to oxidation reaction but low level of sensitivity could be explained that CH_4 oxidation occurred on the active and inactive electrodes.

Li and Kale [46] investigated the sensing properties of the planar mixed potential CO sensor coupled with ITO as the sensing electrode. It was shown that the sensing properties of the fabricated sensor ITO/ScSZ/Pt could be greatly influenced by the thickness of the ITO sensing film. As the thickness of ITO sensing layer is reduced to micrometer range, the sensitivity of the sensor to CO was significantly enhanced. However, if the thickness is decreased further to submicrometer scale (i.e. ~0.5 μm), the sensor showed much lower sensitivity and sluggish response to CO. The possible reason could be related to the decrease of the effective area of the triple phase boundary and higher charge carrier transport resistance due to the much thinner porous ITO film.

Lee et al. [47] studied the oxygen-permeating property of $La_{0.7}Sr_{0.3}Ga_{0.6}Fe_{0.4}O_{3-\delta}$ (LSGF) membranes. They found that LSGF exhibited the limited oxygen permeation flux but it could be enhanced by coating on both sides of membrane with porous $La_{0.6}Sr_{0.4}CoO_{3-\delta}$ (LSC). These increasing oxygen fluxes resulted from increasing of the effective surface area and surface activity to dissociation and association reaction of oxygen. Moreover, the phase analysis of LSGF before and after the oxygen permeation was investigated by XRD. It was found that both XRD patterns exhibited only perovskite phases which confirmed the phase stability of LSGF membrane [48].

Ishihara et al. [49] studied an amperometric CO sensor using a solid oxide electrolyte. From this study, it can be concluded that the $LaGaO_3$-based oxide electrolyte combined with $Au10wt\%$-$In_{1.9}Sn_{0.1}O_3$ and RuO_2-$La_{0.6}Sr_{0.4}CoO_3$ as the inactive and active electrode catalysts, respectively could be used for CO detection. Moreover, doping Fe into Ga sites in $LaGaO_3$-based perovskite oxide is also effective for achieving high sensitivity and selectivity to CO.

1.6 The objectives of this research

Since the semiconductor SnO_2 type is popularly used to detect CO but it is sensitive with other coexisting gases, in particular with H_2. Many researches were focused on the development of materials for CO sensor with high sensitivity and selectivity. From our previous work [49], we studied the CO sensitivity of $LaGaO_3$-based electrolyte and found that Fe-doped LSGM sensor exhibited the highest CO sensitivity and selectivity comparing with other interference gases. In this research, further studies were performed on the effect of Fe dopant into lanthanum gallate ($LaGaO_3$)-based electrolytes including with the effect of temperature, modified anode materials and cross-sensitivities on CO sensitivities.

Therefore, the objectives of this research are:
1. To synthesize Fe-doped $LaGaO_3$-based electrolytes for carbon monoxide sensor.

2. To synthesize anode materials for carbon monoxide sensor.

3. To evaluate sensing properties and selectivity of the synthesized electrolytes coupled with electrodes.

1.7 The scopes of this research

This research focuses on the following studies:

1. Effect of Fe dopant into $LaGaO_3$-based electrolyte on CO sensitivity

2. Effect of temperature dependence on CO sensitivity

3. Cross-sensitivities of CO sensor for CO_2, CH_4 and H_2 and

4. Effect of metal additives into $La_{0.6}Sr_{0.4}CoO_3$ electrode on sensing measurements

Firstly, $La_{0.8}Sr_{0.2}Ga_{0.8}Mg_{0.2-x}Fe_xO_3$ (x = 0.05, 0.10, 0.15, 0.20) oxides and $La_{0.8}Sr_{0.2}Ga_{1-x}Fe_xO_3$ (x = 0.10, 0.15, 0.20, 0.30) oxides are prepared. The synthesized perovskite compounds were characterized by using X-ray diffractometer. For sensing measurement, all samples are coupled with $Au10wt\%$-$In_{0.95}Sn_{0.05}O_{1.5}$ (ITO955) and RuO_2-$La_{0.6}Sr_{0.4}CoO_3$ (LSC64) as the inactive and active electrodes, respectively and expose to CO at the operating temperature ranging from 300-500°C.

Secondly, the cross-sensitivities of the sensors are studied by exposing the coexisting gases such as CO_2, CH_4 and H_2 into the reactor chamber.

Lastly, RuO_2-transition metal doped $La_{0.6}Sr_{0.4}O_3$ electrode are synthesized by impregnation of $Pt1wt\%$ and $Pd10wt\%$+$Pt5wt\%$ and characterized by using X-ray diffractometer. The sensing measurements are studied by using the optimized electrolyte coupled with the synthesized active electrodes while inactive electrode is fixed.

CHAPTER II

EXPERIMENTAL

The chemical, apparatus and experimental procedures including processing of perovskite powders synthesis, perovskite disc preparation and characterization of materials, are described as below:

2.1 Chemicals

The chemicals listed in Table 2.1, were used without further purification.

Table 2.1 The chemicals used in this research.

Chemicals	Name	Purity%	Company
La_2O_3	Lanthanum oxide	99.99	Wako
$SrCO_3$	Strontium carbonate	99.99	Wako
Ga_2O_3	Gallium oxide	99.99	Kishida
MgO	Magnesium oxide	99.9	Wako
Fe_2O_3	Ferric oxide	99.5	Kishida
In_2O_3	Indium oxide	99.99	Wako
SnO_2	Tin oxide	99.99	Wako
8YSZ	Yttria stabilized zirconia	99.0	Tosoh
15SDC	Samaria doped ceria	99.9	Daiichi Kigenso
$HAuCl_4 \cdot 4H_2O$	Gold chloride acid	99.0	Chameleon
$La(CH_3COO)_3 \cdot 1.5H_2O$	Lanthanum acetate	99.9	Kishida
$Sr(CH_3COO)_2 \cdot 0.5H_2O$	Strontium acetate	99.9	Kishida
$Co(CH_3COO)_2 \cdot 4H_2O$	Cobalt acetate	99.9	Kishida
H_2PtCl_6	Platinic acid	99.0	Wako
$Pd(CH_3COO)_2$	Palladium acetate	99.9	Kishida

2.2 Synthesis of perovskite powder

All components in Table 2.2 were synthesized by solid state reaction method (SSR).

Table 2.2 The components of all samples

Dopant	Substituted site	Compounds	Abbreviation
		$La_{0.8}Sr_{0.2}Ga_{0.8}Mg_{0.2}O_{3-\delta}$	LSGM8282
Fe	Mg	$La_{0.8}Sr_{0.2}Ga_{0.8}Mg_{0.15}Fe_{0.05}O_{3-\delta}$	LSGMF828155
		$La_{0.8}Sr_{0.2}Ga_{0.8}Mg_{0.1}Fe_{0.1}O_{3-\delta}$	LSGMF82811
		$La_{0.8}Sr_{0.2}Ga_{0.8}Mg_{0.15}Fe_{0.05}O_{3-\delta}$	LSGMF828515
		$La_{0.8}Sr_{0.2}Ga_{0.8}Fe_{0.2}O_{3-\delta}$	LSGF8282
	Ga	$La_{0.8}Sr_{0.2}Ga_{0.9}Fe_{0.1}O_{3-\delta}$	LSGF8291
		$La_{0.8}Sr_{0.2}Ga_{0.85}Fe_{0.15}O_{3-\delta}$	LSGF828515
		$La_{0.8}Sr_{0.2}Ga_{0.8}Fe_{0.2}O_{3-\delta}$	LSGF8282
		$La_{0.8}Sr_{0.2}Ga_{0.7}Fe_{0.3}O_{3-\delta}$	LSGF8273

The perovskite oxides $La_{0.8}Sr_{0.2}Ga_{0.8}Mg_{0.2-x}Fe_xO_{3-\delta}$ (x = 0.05, 0.10, 0.15, 0.20) and $La_{0.8}Sr_{0.2}Ga_{1-x}Fe_xO_{3-\delta}$ (x = 0.10, 0.15, 0.20, 0.30) were prepared by using solid state reaction. La_2O_3, $SrCO_3$, Ga_2O_3, MgO and Fe_2O_3 were used as the starting materials. All of raw materials except La_2O_3 powder which was pre-calcined before use at 1000°C for 3 hours, were used without any purification. The starting oxides in proper ratio (to ensure to the composition of synthesized perovskites in 10 g) were mixed and ground thoroughly in an Al_2O_3 mortar. The mixed powders were red resulting from dark red powder of Fe_2O_3 and calcined in air at 1000°C for 6 hours within a furnace in order to achieve pure phase compounds. At this stage, the calcined powder turned grey. The calcination condition of the $LaGaO_3$-based perovskite powders was set as follows:

1000°C, 6 h

5 h

Room temperature
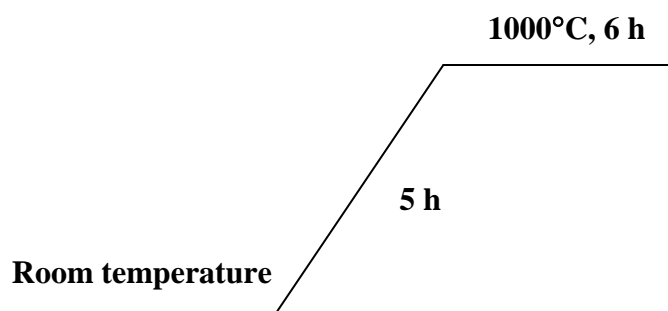
Scheme 2.1 The condition of calcination for perovskite oxide.

2.3 Preparation of perovskite discs

The calcined perovskite powder was ground in the mortar. Subsequently, 2 g of grinding powder was loaded into the cavity of die and they were pressed into discs by using KBr die.

Sample disc
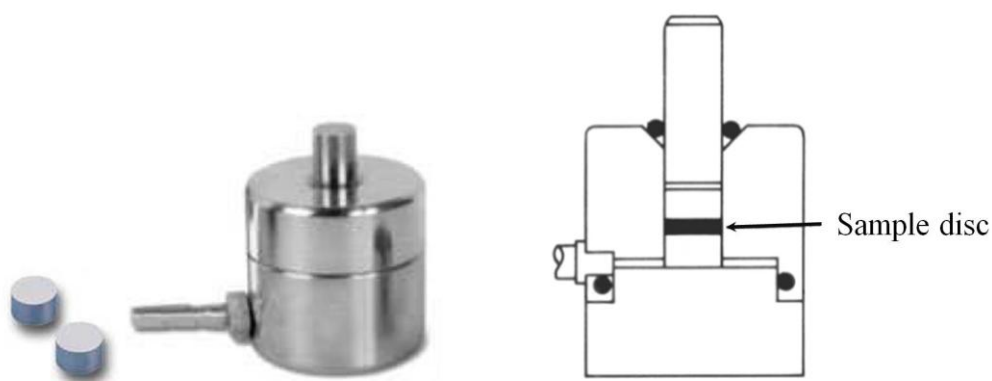
Figure 2.1 The KBr die.

The holder with perovskite powder was pressed by the uniaxial pressing machine. The pressure was released after 5 min and a green disc was obtained with 1 mm of thickness and 16 mm diameter. Ten grams of the starting materials can provide 4 pellets. Then, the discs were sintered in air at 1500°C for 6 hours.

Finally, the black discs were obtained. The condition of sintering of perovskite disk was exhibited in scheme 2.2.

1500°C, 6 h

5 h

1000°C, 6 h

5 h

Room temperature
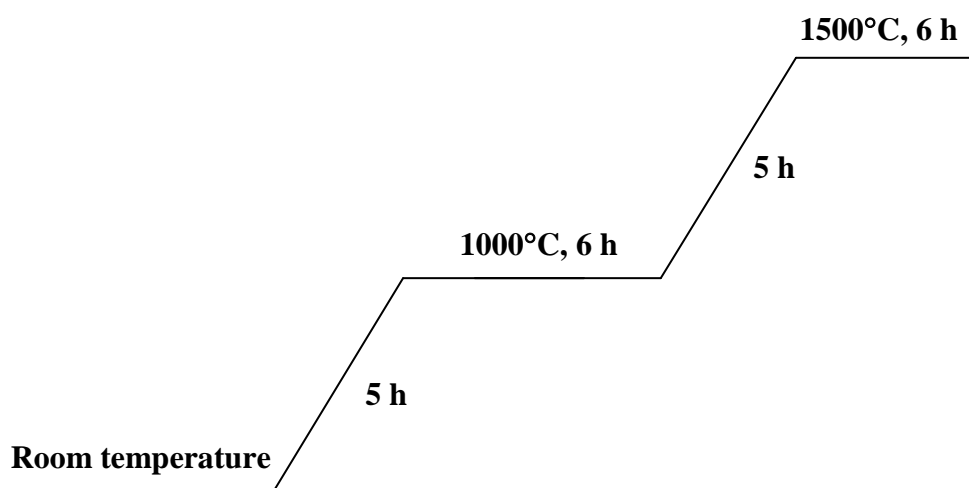
Scheme 2.2 The condition of sintering process for perovskite oxide.

2.4 Synthesis of electrodes

2.4.1 Au10wt%-In$_{0.95}$Sn$_{0.05}$O$_{1.5}$ powder

In$_{0.95}$Sn$_{0.05}$O$_{1.5}$ oxide was prepared by solid state reaction of In$_2$O$_3$ and SnO$_2$. The staring materials were used without any purification. The starting oxides in proper ratio were mixed by ball mill mixer in ethanol. After dried, it was calcined in a furnace. The calcination condition of the In$_{0.95}$Sn$_{0.05}$O$_{1.5}$ powders was set as displayed in Scheme 2.3.

1000°C-1400°C, 6 h

5 h

Room temperature
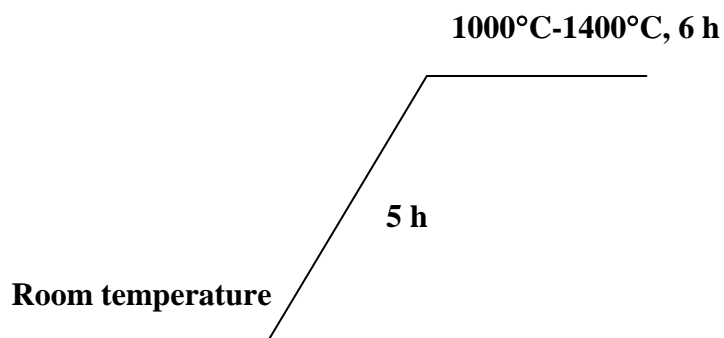
Scheme 2.3 The condition of calcination for $In_{0.95}Sn_{0.05}O_{1.5}$ powder.

Afterwards, $In_{0.95}Sn_{0.05}O_{1.5}$ powder was impregnated with 10wt% aqueous solution of $HAuCl_4 \cdot 4H_2O$. Subsequently, the impregnated solution was heated until dried and calcined at 400°C for 3 h. Finally, the pale yellow-green powder of Au10wt%-ITO955 was obtained. The calcination step of Au10wt%-$In_{0.95}Sn_{0.05}O_{1.5}$ powders was illustrated in Scheme 2.4.

400°C, 3 h

40 min

Room temperature
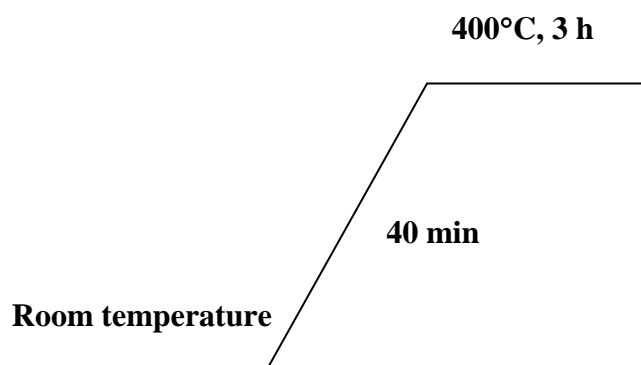
Scheme 2.4 The condition of calcination for Au10wt%-$In_{0.95}Sn_{0.05}O_{1.5}$ powder after impregnation of Au solution into $In_{0.95}Sn_{0.05}O_{1.5}$ powder.

2.4.2 RuO_2-$La_{0.6}Sr_{0.4}CoO_3$ powder

The perovskite powder $La_{0.6}Sr_{0.4}CoO_3$ was prepared by dissolving an appropriate mixture of $La(CH_3COO)_3 \cdot 1.5H_2O$, $Sr(CH_3COO)_2 \cdot 0.5H_2O$ and $Co(CH_3COO)_2 \cdot 4H_2O$ with 1M acetic acid and heated until dried. The dried compound was calcined at 400°C for 2 h and ground in Al_2O_3 mortar. The calcination condition of the $La_{0.6}Sr_{0.4}CoO_3$ powders was set as displayed in Scheme 2.5.

400°C, 2 h

40 min

Room temperature
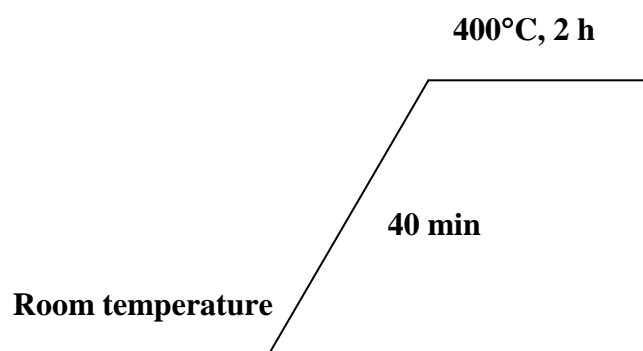
Scheme 2.5 The condition of calcination for the dried mixture compound of $La_{0.6}Sr_{0.4}CoO_3$ oxide.

Subsequently, the powder was calcined at 1000°C for 6 h and then reground. The black powder of $La_{0.6}Sr_{0.4}CoO_3$ was obtained and mixed with RuO_2 (weight ratio 1:9) by ball milling in ethanol. The resulting compound was then dried to obtain RuO_2-$La_{0.6}Sr_{0.4}CoO_3$ powder. The calcination condition of the RuO_2-$La_{0.6}Sr_{0.4}CoO_3$ powder was set as shown in Scheme 2.6.

1000°C, 6 h

5 h

Room temperature
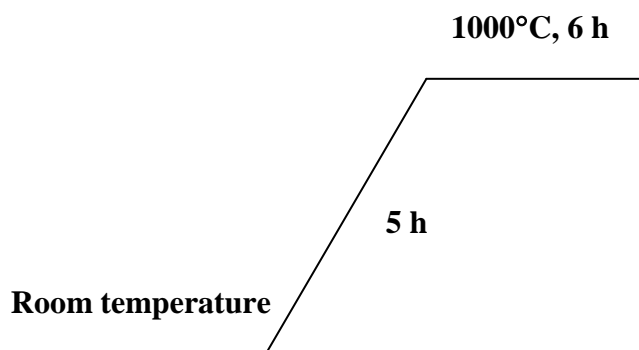
Scheme 2.6 The condition of calcination for $La_{0.6}Sr_{0.4}CoO_3$ powder.

2.4.3 RuO_2-(Pt1wt%)$La_{0.6}Sr_{0.4}CoO_3$ powder

The $La_{0.6}Sr_{0.4}CoO_3$ powder was prepared as mentioned above. Afterwards, impregnation of 1wt% aqueous solution of H_2PtCl_6 was required and heated until dried. Subsequently, the mixed compound was ground and calcined at various temperatures ranging from 900°C to 1000°C for 3h. The calcination process of (Pt1wt%)$La_{0.6}Sr_{0.4}CoO_3$ powders was illustrated in Scheme 2.7.

900°C -1000°C, 3 h

5 h

Room temperature
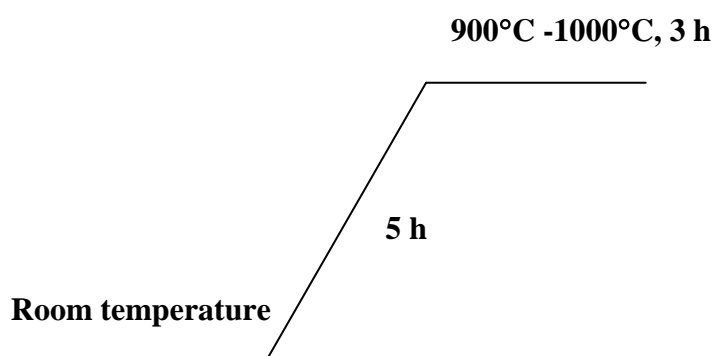
Scheme 2.7 The condition of calcination for (Pt1wt%)$La_{0.6}Sr_{0.4}CoO_3$ powder.

After (Pt1wt%)$La_{0.6}Sr_{0.4}CoO_3$ powder was obtained, RuO_2 powder was then mixed with weight ratio 9:1 by ball milling in ethanol. The mixed compound was dried to obtain RuO_2-(Pt1wt%)$La_{0.6}Sr_{0.4}CoO_3$ powder.

2.4.4 RuO_2-(Pd10wt%+Pt5wt%)$La_{0.6}Sr_{0.4}CoO_3$ oxide

$Pd(CH_3COO)_2$ was dissolved in distilled water and added few drops of acetic acid into the solution. The 10wt% of palladium solution was impregnated into $La_{0.6}Sr_{0.4}CoO_3$ powder and heated until dried. Then, a H_2 reduction was operated at 300°C for 3 h followed by calcination in air at 500°C for 3 h. Subsequently, a 5wt% aqueous solution of H_2PtCl_6 was added and stirred. The Pd-Pt mixture was heated until dried and ground in Al_2O_3 mortar followed by calcination in air at 500°C for 3 h. The (Pd10wt%+Pt5wt%)$La_{0.6}Sr_{0.4}CoO_3$ powder was obtained and mixed with RuO_2 at ratio 1:9 by using ball mill mixer. The resulting compound was then dried to obtain RuO_2-(Pd10wt%+Pt5wt%)$La_{0.6}Sr_{0.4}CoO_3$ powder. The calcination process in this preparation was illustrated in Scheme 2.8.

500°C, 3 h

50 min

Room temperature
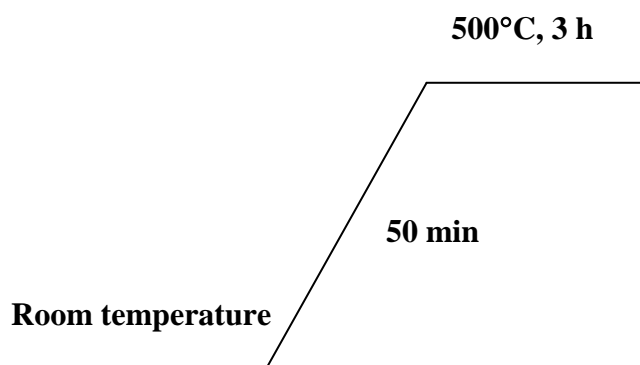
Scheme 2.8 The condition of calcination for (Pd10wt%)$La_{0.6}Sr_{0.4}CoO_3$ and (Pd10wt%+Pt5wt%)$La_{0.6}Sr_{0.4}CoO_3$ powder.

2.5 Preparation of slurry coating membranes

The synthesized powder of electrodes was dispersed into butyl acetate solution and mixed thoroughly in mortar. The slurry of each electrode was then painted on electrolyte membrane and calcined at 800°C for 1 h (with YSZ and SDC electrolytes) or 1000°C for 1 h (with Fe-doped $LaGaO_3$ electrolytes). The calcination conditions of slurry coating membranes were shown in Scheme 2.9.

800°C (or 1000°C), 1 h

3 h

Room temperature
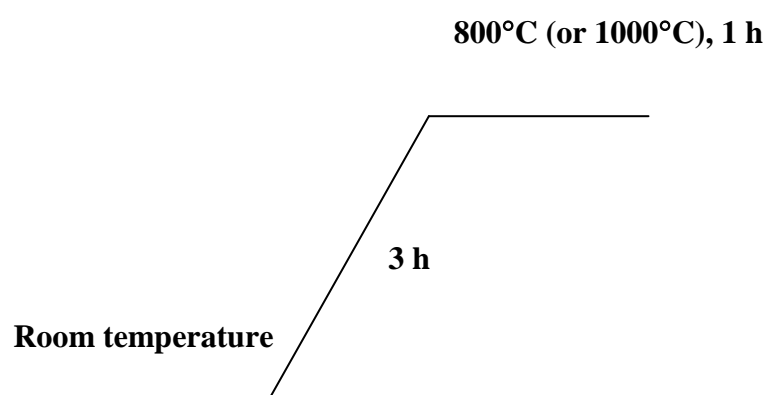
Scheme 2.9 The condition of calcination for slurry coated membranes.

2.6 Characterization of the perovskite oxides

2.6.1 X-ray diffractrometry (XRD)

The XRD patterns were taken by using Rigaku, DMAX 2002 Ultima Plus X-Ray powder diffractometer equipped with a monochromator and a Cu-target X-ray tube (40 kV, 30 mA) and angles of 2θ ranged from 20-70 degree (step time 0.5 sec., scan step 0.020 degree) at Department of Chemistry, Faculty of Science, Chulalongkorn University, Thailand and Rigaku (Rinto type 2500) at Department of Applied Chemistry, Faculty of Engineering, Kyushu University, Japan.

2.6.2 Scanning electron microscopy (SEM)

The morphology of the sintered disc was carried out using a SEM (Keyence) with EDX (Edax) at Department of Applied Chemistry, Faculty of Engineering, Kyushu University, Japan.

2.7 Sensing measurement

All electrolyte discs were polished with a diamond wheel to reduce thickness to 0.4 mm. The slurry of Au10 wt%-ITO955 was painted on one face of electrolyte disc as the inactive electrode in a 6 mm diameter area. On the other side, the slurry of RuO_2-LSC64 was painted as the active electrode with the same size. Subsequently, the painted disc was fired at 800°C for 1 h (YSZ and SDC electrolytes) or 1000°C for 1 h (for LSGMF and LSGF series). Afterward, Au mesh connected with Au wire and Pt mesh with Pt wire (used as current collectors) were attached on the painted area of inactive (Au10 wt%-ITO955) and active (RuO_2-LSC64) electrodes, respectively and set on the painted disc using commercial Au and Pt pastes, respectively. The sensor element was shown in Figure 2.2.
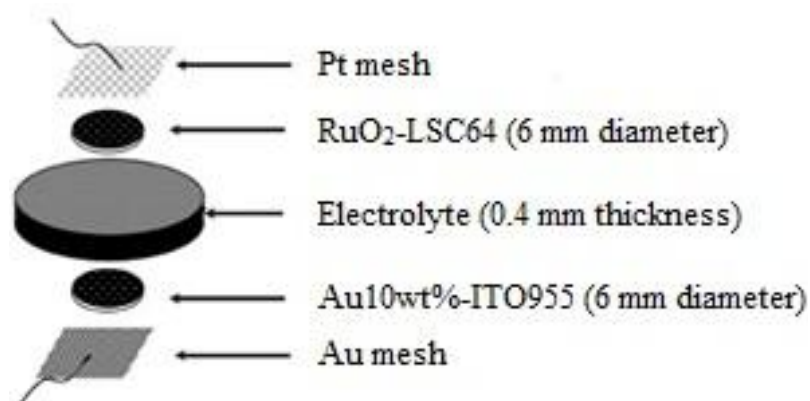
Figure 2.2 A schematic view of the planar sensor element.

The fabricated sensor was then placed inside a ceramic tube which was attached with a gas flow assembly and external electrical contacts. The tube was put

inside a furnace, and the temperature near the sensor was controlled with a temperature controller and varied in the temperature range from 300°C to 500°C. Reference air was fed into the sensor system during the time of study. The sample gas from gas mixed-chamber was CO in ppm mixed with air and it was fed at 100 ml/min. The change in current was measured by the dc two-probe method. In the amperometric mode, dc 1 V was always applied using a potentiostat/galvanostat as the active electrode was always a positive one. The current was measured with a digital electrometer. The sensor setup was illustrated in Figure 2.3. All of the sensing measurements were repeated twice.
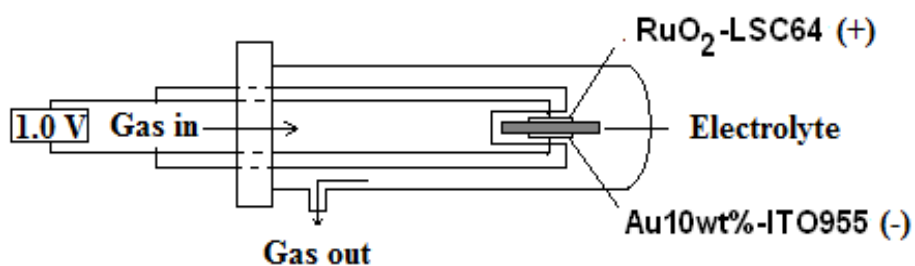
Figure 2.3 A planar sensing equipment.

CHAPTER III

RESULTS AND DISCUSSION

Since the synthesized perovskite oxides lanthanum gallate (LaGaO$_3$) using as electrolytes were doped with different contents of metal ion into A-site (Sr) and B-site (Mg and Fe), then each perovskite compound is expressed by the abbreviation of the initial letters of each metal in A- and B-sites following by the corresponding number of each proportional metal composition sequentially. For example, La$_{0.8}$Sr$_{0.2}$Ga$_{0.8}$Mg$_{0.2}$O$_{3-\delta}$ and La$_{0.8}$Sr$_{0.2}$Ga$_{0.8}$Mg$_{0.15}$Fe$_{0.05}$O$_{3-\delta}$ are abbreviated as LSGM8282 and LSGMF828155, respectively.

In this chapter, the results were divided into four topics as follows:
- Preparation and characterization of electrolytes;
- Preparation and characterization of cathode (inactive electrode);
- Preparation and characterization of anodes (active electrodes);
- Sensing properties of the sensor elements.

3.1 Preparation and characterization of electrolytes

3.1.1 La$_{0.8}$Sr$_{0.2}$Ga$_{0.8}$Mg$_{0.2-x}$Fe$_x$O$_{3-\delta}$ (x = 0.05, 0.10, 0.15) or LSGMF series

3.1.1.1 Preparation of LSGMF series

All of the LSGMF perovskite oxides were prepared by using solid state reaction of the compounds La$_2$O$_3$, SrCO$_3$, Ga$_2$O$_3$, MgO and Fe$_2$O$_3$. All of the mixed samples were red resulting from dark red powder of Fe$_2$O$_3$ and calcined at 1000°C for 6 h. Subsequently, all discs were sintered in air at 1500°C for 6 h in order to make them more uniform. Finally, the black discs were obtained.

3.1.1.2 XRD characterization of LSGMF series

The structures of synthesized LSGMF compounds were characterized by XRD which used to indicate the formation of the perovskite phase. The diffraction peaks of perovskites were observed within angles of 2θ ranging from 20-70 degree. The XRD patterns of LSGMF series are shown in Figure 3.1.
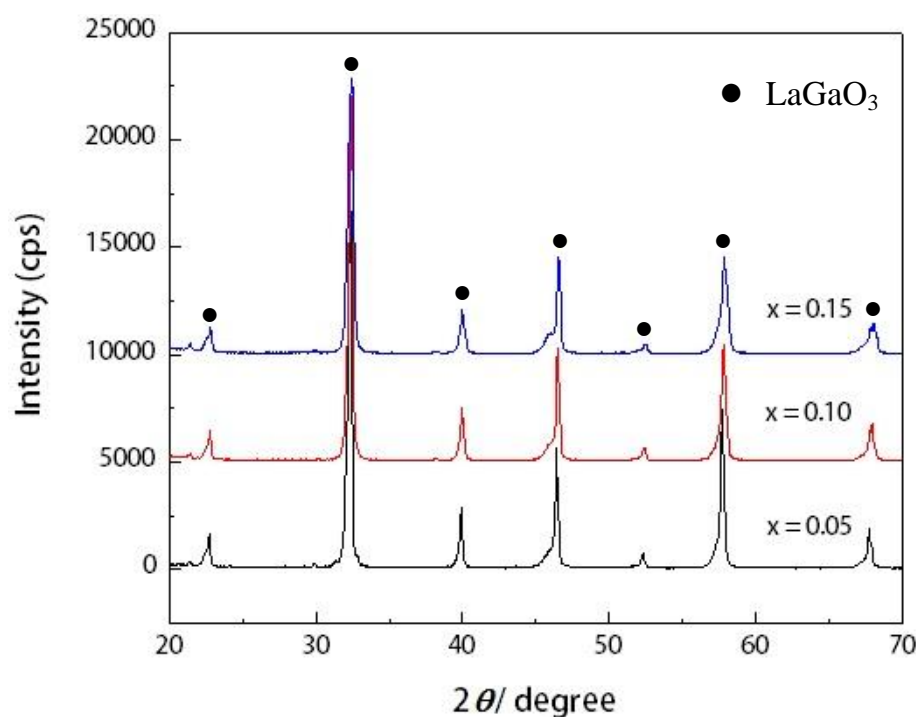
Figure 3.1 XRD patterns of $La_{0.8}Sr_{0.2}Ga_{0.8}Mg_{0.2-x}Fe_xO_{3-\delta}$ (x = 0.05, 0.10, 0.15) perovskite compounds.

The XRD patterns of $La_{0.8}Sr_{0.2}Ga_{0.8}Mg_{0.2-x}Fe_xO_{3-\delta}$ compounds where x = 0.05, 0.10 and 0.15 revealed the pure phase of a cubic structure of ABO_3 perovskite oxides. It was illustrated that the XRD patterns are shifted toward the higher angle as Fe contents in $La_{0.8}Sr_{0.2}Ga_{0.8}Mg_{0.2-x}Fe_xO_{3-\delta}$ are increased as shown in Figure 3.2 corresponding to the lattice shrinkage.
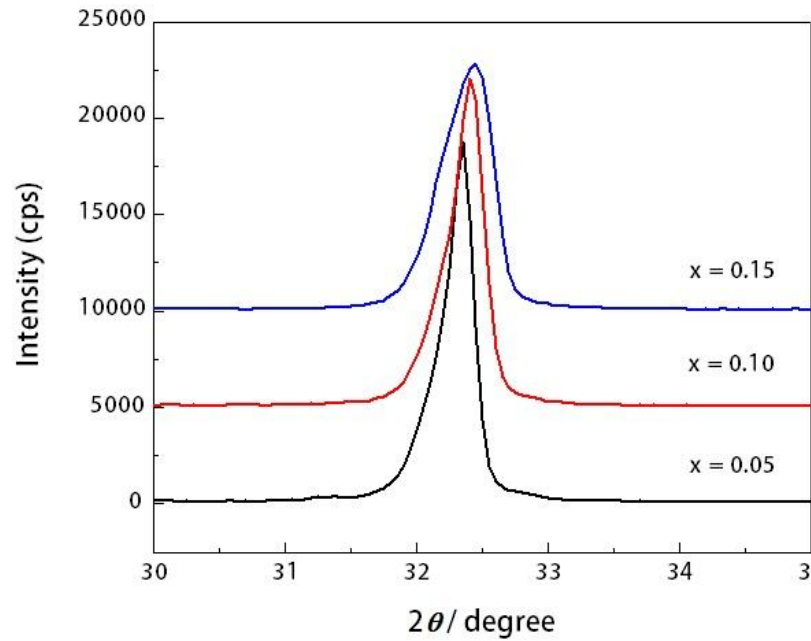
Figure 3.2 Partial XRD patterns of $La_{0.8}Sr_{0.2}Ga_{0.8}Mg_{0.2-x}Fe_xO_{3-\delta}$ (x = 0.05, 0.10, 0.15) perovskite compounds.

This shift indicated that some of the Mg^{2+} ions ($r_{Mg^{2+}}$ = 0.72 Å) with six-fold coordination were substituted by smaller Fe^{3+} ions ($r_{Fe^{3+}}$ = 0.645 Å). The XRD result in this work also shown same trend corresponding to the report of Rusmiati et al.[33]. The lattice shrinkages of LSGMF oxides were shown in Figure 3.3. Their lattice parameters were calculated by Jade software as shown in Table 3.1. Due to smaller ionic radius of Fe^{3+} with respect to Mg^{2+}, doping of $La_{0.8}Sr_{0.2}Ga_{0.8}Mg_{0.2}O_{3-\delta}$ with iron at magnesium-site leads to smaller unit cell volume with increasing Fe contents.
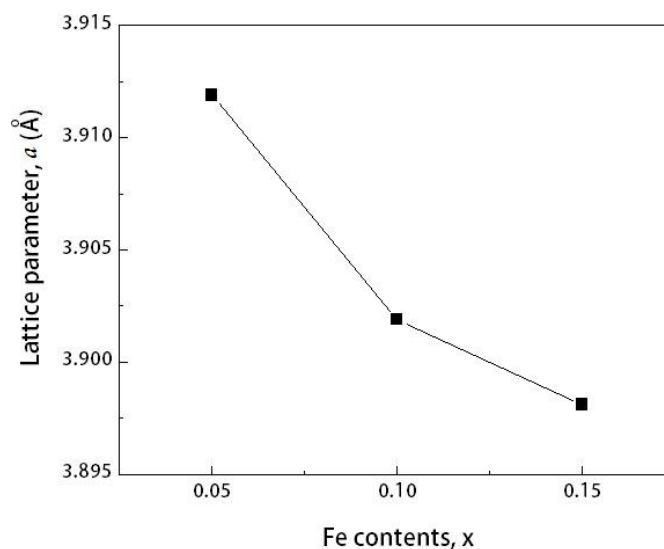
Figure 3.3 Plot of the lattice parameter, a against Fe contents, x of $La_{0.8}Sr_{0.2}Ga_{0.8}Mg_{0.2-x}Fe_xO_{3-\delta}$ oxides (x = 0.05, 0.10, 0.15).

Table 3.1 The lattice parameters of cubic $La_{0.8}Sr_{0.2}Ga_{0.8}Mg_{0.2-x}Fe_xO_{3-\delta}$ oxides (x = 0.05, 0.10, 0.15).

Ratio	Lattice parameter; a (Å)	
	This work	**Ref. [33]**
x = 0.05	3.9119	3.9183
x = 0.10	3.9019	3.9126
x = 0.15	3.8981	3.9061

3.1.1.3 Tolerance factors of the synthesized LSGMF series

The perovskite structure was known to be stable only for $0.95 \leq t \leq 1.04$ and was cubic in this range. As shown in Table 3.2, the tolerance numbers of Fe doping into Mg-site of $La_{0.8}Sr_{0.2}Ga_{0.8}Mg_{0.2}O_3$ oxides were close to 1. It is confirmed that structures of the samples were cubic perovskite–type.

Table 3.2 The tolerance factors of Fe doping into Mg-site of $La_{0.8}Sr_{0.2}Ga_{0.8}Mg_{0.2}O_3$ oxides.

Compounds	Abbreviations	Tolerance factor (t)
$La_{0.8}Sr_{0.2}Ga_{0.8}Mg_{0.2}O_3$	LSGM8282	0.962
$La_{0.8}Sr_{0.2}Ga_{0.8}Mg_{0.15}Fe_{0.05}O_3$	LSGMF828155	0.964
$La_{0.8}Sr_{0.2}Ga_{0.8}Mg_{0.1}Fe_{0.1}O_3$	LSGMF82811	0.966
$La_{0.8}Sr_{0.2}Ga_{0.8}Mg_{0.05}Fe_{0.15}O_3$	LSGMF828515	0.968

From this table, the various amounts of Fe doping at Mg-sites resulted in the change of tolerance factors. It is shown that partial substitution of smaller Fe^{3+} ions into larger Mg^{2+} ions caused the increase of tolerance factor. Even though the contents of Fe increased, the t values are still in the range 0.96-0.97.

3.1.2 $La_{0.8}Sr_{0.2}Ga_{1-x}Fe_xO_{3-\delta}$ (x = 0.10, 0.15, 0.20, 0.30) or LSGF series

3.1.2.1 Preparation of LSGF series

All of the LSGF perovskite oxides were prepared by using solid state reaction of the compounds La_2O_3, $SrCO_3$, Ga_2O_3 and Fe_2O_3 as mentioned previously. Lastly, the black LSGF discs were obtained.

3.1.2.2 XRD characterization of LSGF series

The structures of synthesized LSGF compounds were characterized by using XRD as shown in Figure 3.4.
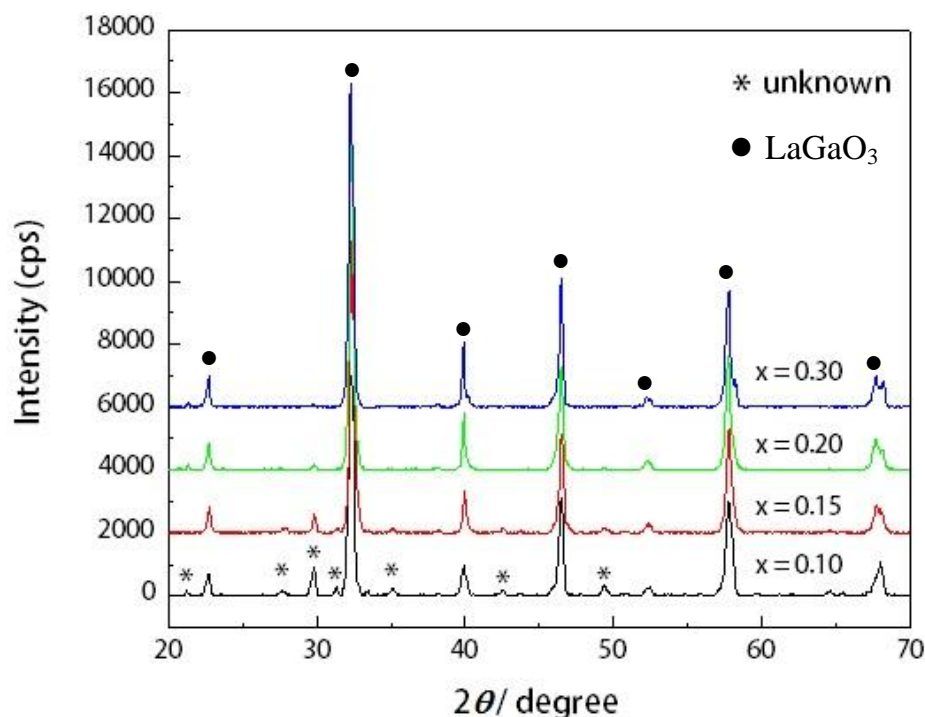
Figure 3.4 XRD patterns of $La_{0.8}Sr_{0.2}Ga_{1-x}Fe_xO_{3-\delta}$ (x = 0.10, 0.15, 0.20, 0.30) perovskite compounds.

The XRD patterns of $La_{0.8}Sr_{0.2}Ga_{1-x}Fe_xO_{3-\delta}$ compounds where x = 0.10, 0.15, 0.20 and 0.30 revealed the main phase of a cubic structure of ABO_3 perovskite oxides and some weak peaks from unknown impurities. Moreover, the secondary phases decreased with increasing Fe concentration in the compounds.

Because the ionic radii of Fe^{3+} ($r_{Fe^{3+}} = 0.645$ Å, CN = 6) is higher and that of Ga^{3+} ($r_{Ga^{3+}} = 0.62$ Å, CN = 6), the expansion of M-O (M = $Ga_{1-x}Fe_x$) bond length in a MO_6 octahedron illustrates the Fe substitution into Ga-site corresponding to the diffraction peaks shift to lower angle as shown in Figure 3.5.
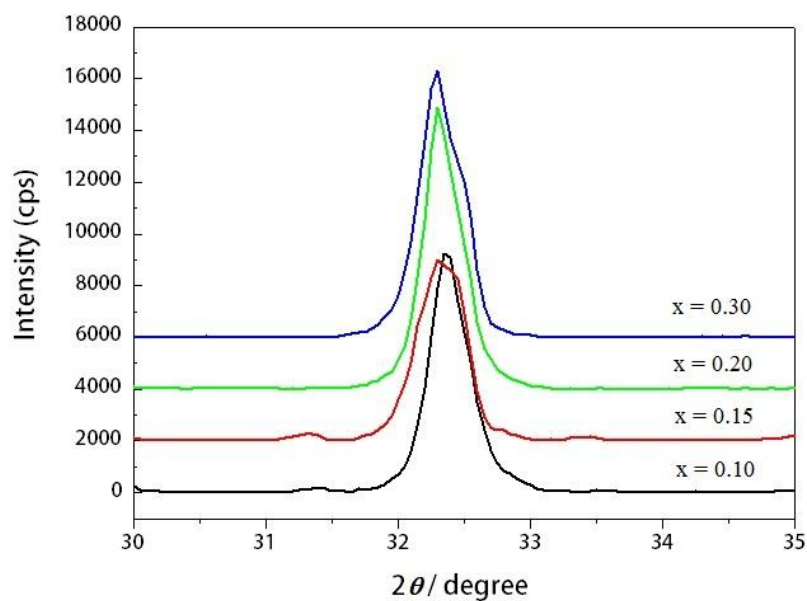
Figure 3.5 Partial XRD patterns of $La_{0.8}Sr_{0.2}Ga_{1-x}Fe_xO_{3-\delta}$ (x = 0.10, 0.15, 0.20, 0.30) perovskite compounds.

The unit cell parameters correlated with Fe contents in LSGF series were demonstrated in Figure 3.6 and calculated by Jade software as shown in Table 3.3.
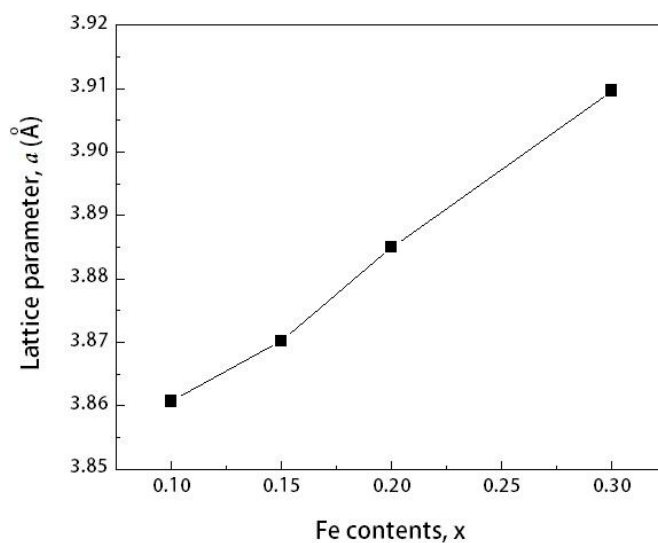
Figure 3.6 The lattice parameter, a against Fe contents, x of $La_{0.8}Sr_{0.2}Ga_{1-x}Fe_xO_{3-\delta}$ oxides (x = 0.10, 0.15, 0.20, 0.30).

Table 3.3 The lattice parameters of cubic $La_{0.8}Sr_{0.2}Ga_{1-x}Fe_xO_{3-\delta}$ (x = 0.10, 0.15, 0.20, 0.30)

Ratio	Lattice parameter; a (Å)
x = 0.10	3.8607
x = 0.15	3.8702
x = 0.20	3.8850
x = 0.30	3.9097

From Table 3.3, the substitutions of Fe into Ga-site have an effect on the enhancement of unit cell parameters and therefore the structures with increasing Fe dopant into Ga-site are also expanded.

3.1.2.3 Tolerance factors of the synthesized LSGF series

The calculated tolerance factors for LSGF series were listed in Table 3.4. It is seen that the tolerance factors of Fe-doped LSG was close to 1 and in the range $0.95 \leq t \leq 1.04$.

Table 3.4 The tolerance factors of Fe doping into Ga-site of $La_{0.8}Sr_{0.2}GaO_3$ oxides.

Compounds	Abbreviations	Tolerance factor (t)
$La_{0.8}Sr_{0.2}Ga_{0.9}Fe_{0.1}O_3$	LSGF8291	0.971
$La_{0.8}Sr_{0.2}Ga_{0.85}Fe_{0.15}O_3$	LSGF828515	0.970
$La_{0.8}Sr_{0.2}Ga_{0.8}Fe_{0.2}O_3$	LSGF8282	0.969
$La_{0.8}Sr_{0.2}Ga_{0.7}Fe_{0.3}O_3$	LSGF8273	0.968

From this table, the various amounts of Fe doping at Mg-sites resulted in the change of tolerance factors. In other words, the partial substitution with a small different ionic size between Fe^{3+} and Ga^{3+} ions caused increasing tolerance factors. In

spite of, the contents of Fe increased, the t values are still in the range 0.96-0.97. These confirm that the structure of synthesized perovskites are stable.

3.2 Preparation and characterization of cathode (inactive electrode)

3.2.1 Au10wt%-In$_{0.95}$Sn$_{0.05}$O$_{1.5}$ powder

3.2.1.1 Preparation of In$_{0.95}$Sn$_{0.05}$O$_{1.5}$

ITO955 was synthesized by using solid state reaction of stoichiometric mixtures of In$_2$O$_3$ and SnO$_2$ as mention in Chapter II. It was calcined at various temperatures ranging from 1000°C to 1400°C and phase formation was confirmed by XRD analysis.

3.2.1.2 XRD characterization of In$_{0.95}$Sn$_{0.05}$O$_{1.5}$

The XRD patterns of ITO955 at various calcinating temperatures were shown in Figure 3.7. The XRD patterns of ITO955 powder which were calcined at temperatures ranging from 1000°C to 1300°C showed main phase of indium oxide with the secondary phase of SnO$_2$. Increasing the calcination temperatures resulted in increasing the intensities of the characteristic peaks of indium oxide and decreasing that of secondary phase. When the calcination temperature up to 1400°C, XRD pattern exhibited only pure phase of indium oxide structure matching with In$_2$O$_3$ from XRD database. This is illustrated that ITO955 can be achieved by calcinating an appropriate mixture of SnO$_2$ and In$_2$O$_3$ at 1400°C for 6 h.
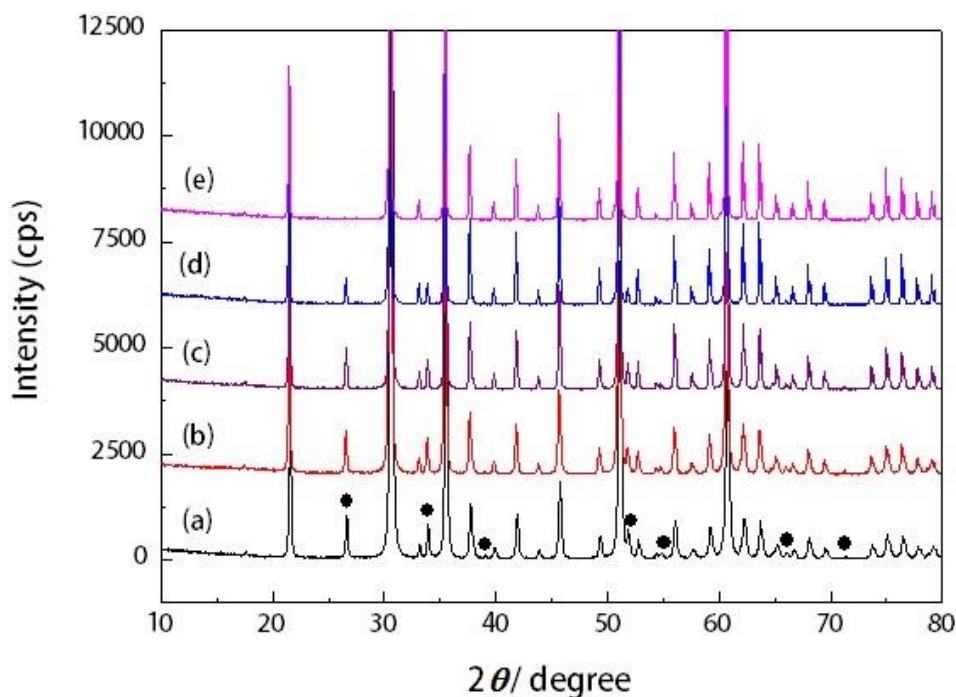
Figure 3.7 XRD patterns of $In_{0.95}Sn_{0.05}O_{1.5}$ oxides after calcinations at (a) 1000°C, (b) 1100°C, (c) 1200°C, (d) 1300°C and (e) 1400°C for 6 hours. Black dots expressed SnO_2 phase.

3.2.1.3 Preparation of Au10wt%-$In_{0.95}Sn_{0.05}O_{1.5}$ by conventional impregnation

ITO955 powder was impregnated with 10wt% aqueous solution of $HAuCl_4 \cdot 4H_2O$. Subsequently, the impregnated solution was heated until dried and calcined at 400°C for 3 h. Finally, the pale yellow-green powder of Au10wt%-ITO955 was obtained.

3.2.1.4 XRD characterization of Au10wt%-$In_{0.95}Sn_{0.05}O_{1.5}$

The formation of calcined Au10wt%-ITO955 powder was investigated by XRD as shown in Figure 3.8.
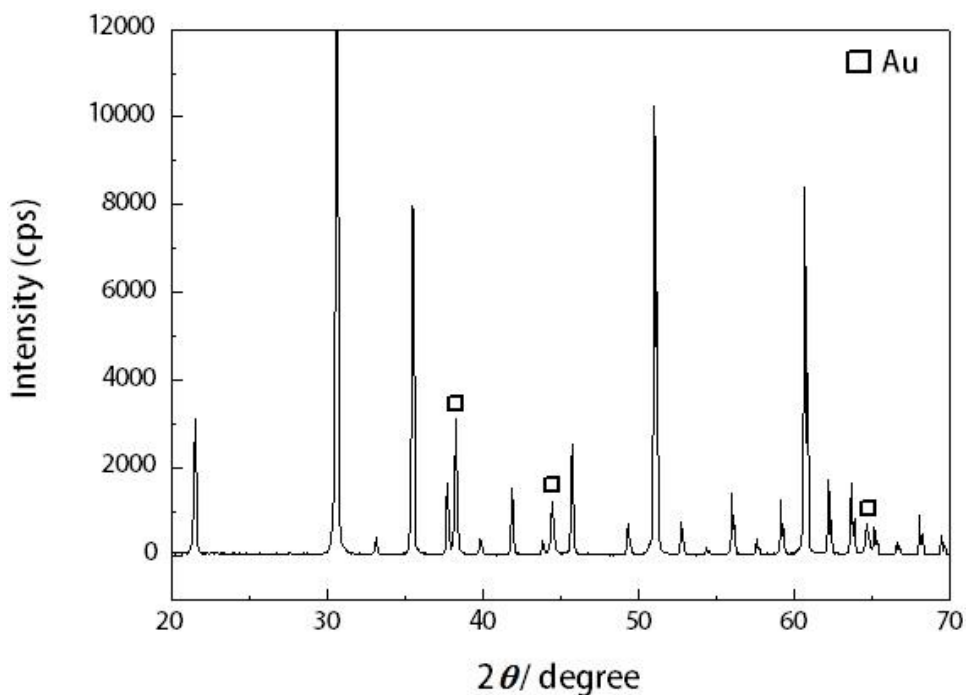
Figure 3.8 XRD pattern of Au10wt%-$In_{0.95}Sn_{0.05}O_{1.5}$ after calcined at 400°C for 3 hours.

This XRD pattern shows the mixed pure phase of Au and In_2O_3 without any secondary phase peak. Considering the peaks strength, the particle size of Au seems to be small and highly dispersed state is obtained.

3.3 Preparation and characterization of anodes (active electrodes)

3.3.1 RuO_2-$La_{0.6}Sr_{0.4}CoO_3$ powder

3.3.1.1 Preparation of RuO_2-$La_{0.6}Sr_{0.4}CoO_3$

Firstly, the perovskite powder LSC64 was prepared and mixed with RuO_2 with weight ratio 1:9 as mentioned in Chapter II. The resulting compound was then dried to obtain RuO_2-LSC64 powder and phase formation was confirmed by XRD analysis.

3.3.1.2 XRD characterization of RuO$_2$- La$_{0.6}$Sr$_{0.4}$CoO$_3$

The formation of RuO$_2$-LSC64 was studied by using XRD as shown in Figure 3.9.
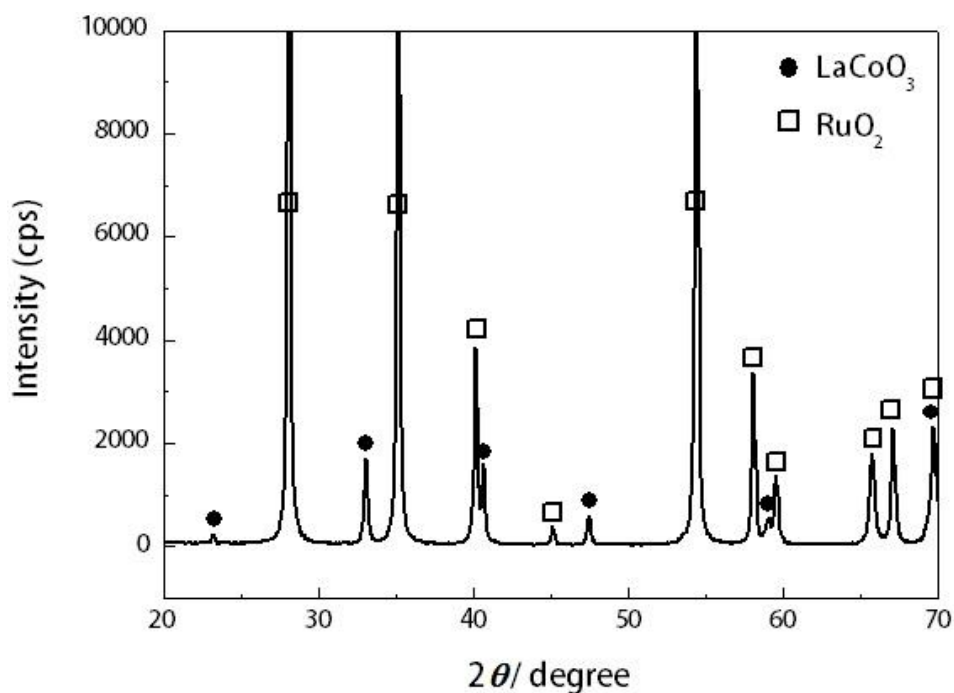
Figure 3.9 XRD pattern of RuO$_2$-La$_{0.6}$Sr$_{0.4}$CoO$_3$ powder prepared by ball milling.

From XRD pattern, it showed the mixed pure phase of RuO$_2$ and LaCoO$_3$ perovskite oxide with no impurity peak which confirmed the composite of RuO$_2$ and LSC64 powder. Moreover, the particle size of RuO$_2$ corresponding to the peak strength seems to be small and highly dispersed state is obtained.

3.3.2 RuO_2-(Pt1wt%)$La_{0.6}Sr_{0.4}CoO_3$ powder

3.3.2.1 Preparation of (Pt1wt%)$La_{0.6}Sr_{0.4}CoO_3$

The (Pt1wt%)$La_{0.6}Sr_{0.4}CoO_3$ powder was firstly prepared LSC64 and subsequently added 1wt% of Pt solution as mentioned in Chapter II. The structure was confirmed by XRD analysis.

3.3.2.2 XRD characterization of (Pt1wt%)$La_{0.6}Sr_{0.4}CoO_3$

The formation of Pt1wt%-$La_{0.6}Sr_{0.4}CoO_3$ was investigated by using XRD as shown in Figure 3.10.
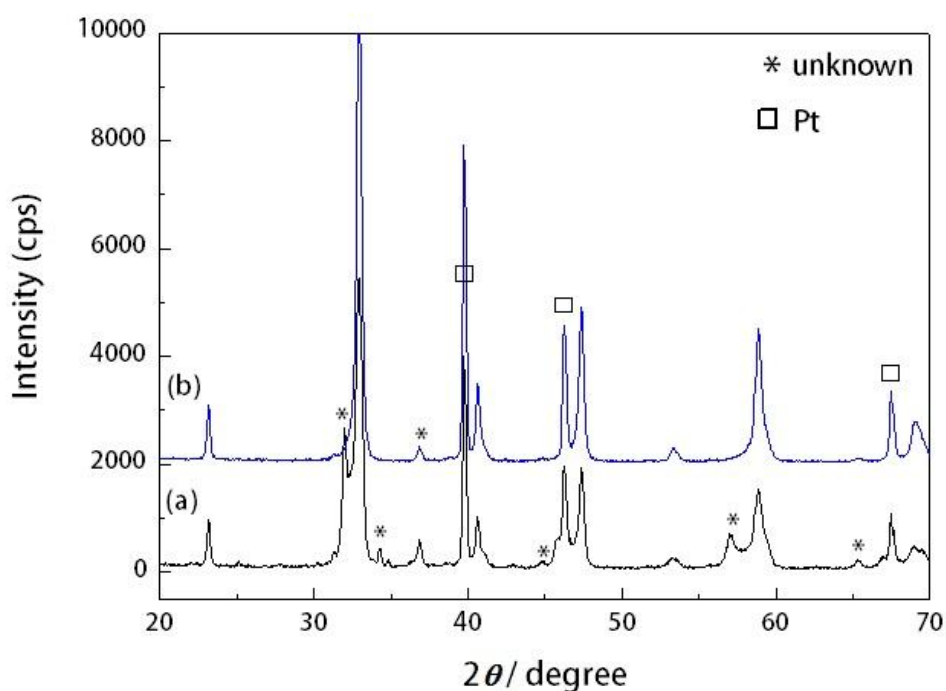
Figure 3.10 XRD patterns of (Pt1wt%)$La_{0.6}Sr_{0.4}CoO_3$ after calcined at (a) 900°C and (b) 1000°C for 3 hours.

It was illustrated that XRD pattern of the compound calcined at 900°C exhibited intense secondary phase of unknown mixing with Pt metal and LSC64

phase. Increasing calcinations temperature up to 1000°C revealed the decreasing of impurity peak strength and showed the mixed pure phase of Pt metal and LSC64 perovskite oxide. Considering the peak strength, the particle size of Pt seems to be small and highly dispersed state is obtained. This can be confirmed the composite of Pt and LSC64 powder achieving after calcined at 1000°C for 3 h.

3.3.2.3 Preparation of RuO_2-(Pt1wt%)$La_{0.6}Sr_{0.4}CoO_3$

After (Pt1wt%)LSC64 powder was obtained, RuO_2 powder was then mixed with ratio 9:1 by ball milling in ethanol. The mixed compound was dried to obtain RuO_2-(Pt1wt%)LSC64 powder and phase formation was confirmed by XRD analysis.

3.3.2.4 XRD characterization of RuO_2-(Pt1wt%)$La_{0.6}Sr_{0.4}CoO_3$

The formation of RuO_2-(Pt1wt%)$La_{0.6}Sr_{0.4}CoO_3$ was investigated by using XRD as shown in Figure 3.11. The XRD pattern showed the mixed pure phase of RuO_2, Pt and LSC64 perovskite oxide with no other phase peak which confirmed the composite of RuO_2, Pt and LSC64 powder. The particle size of RuO_2 corresponding to the peak strength seems to be small and highly dispersed state is obtained which is similar to that of RuO_2-LSC64.
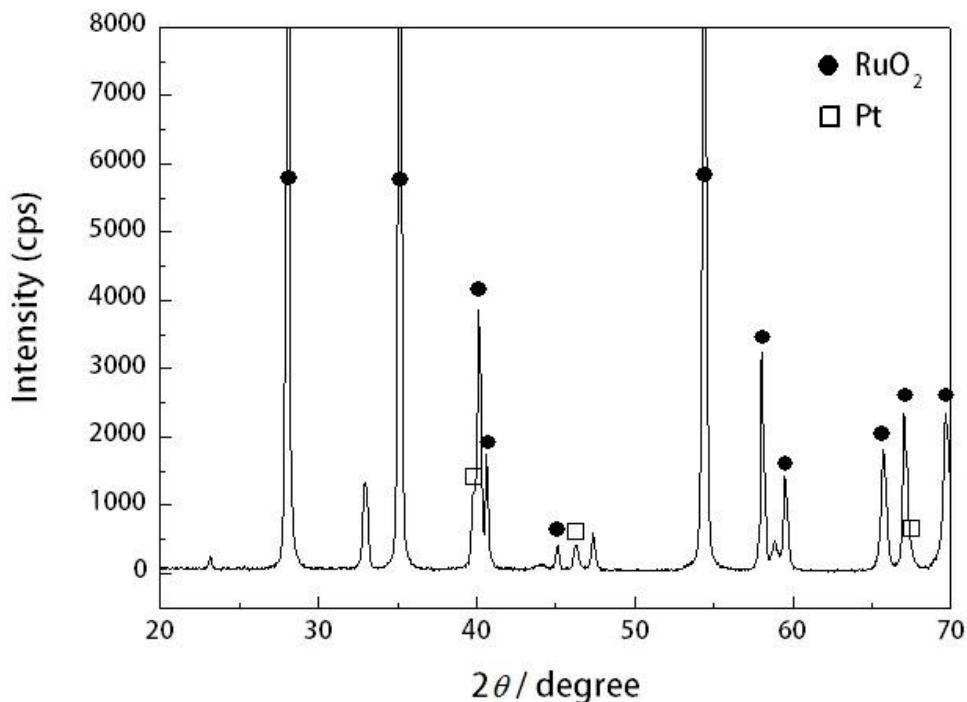
Figure 3.11 XRD pattern of RuO_2-(Pt1wt%)$La_{0.6}Sr_{0.4}CoO_3$ oxide after ball milling.

3.3.3 RuO_2-(Pd10wt%+Pt5wt%)$La_{0.6}Sr_{0.4}CoO_3$ powder

3.3.3.1 Preparation of RuO_2-(Pd10wt%+Pt5wt%)$La_{0.6}Sr_{0.4}CoO_3$

Firstly, (Pd10wt%+Pt5wt%)$La_{0.6}Sr_{0.4}CoO_3$ was prepared as mentioned in Chapter II and mixed with RuO_2 at ratio 1:9 by using ball mill mixer. The resulting compound was then confirmed its structure by XRD analysis.

3.3.3.2 XRD characterization of RuO_2-(Pd10wt%+Pt5wt%) $La_{0.6}Sr_{0.4}CoO_3$

Phase analysis of this compound was studied by X-ray diffraction. The XRD result was shown in Figure 3.12. From XRD pattern, it showed the mixed phase of RuO_2, PdO, Pt and LSC64 perovskite oxide with small weak peak of unknown. This can be confirmed the composite of RuO_2, PdO, Pt and LSC64 powder.
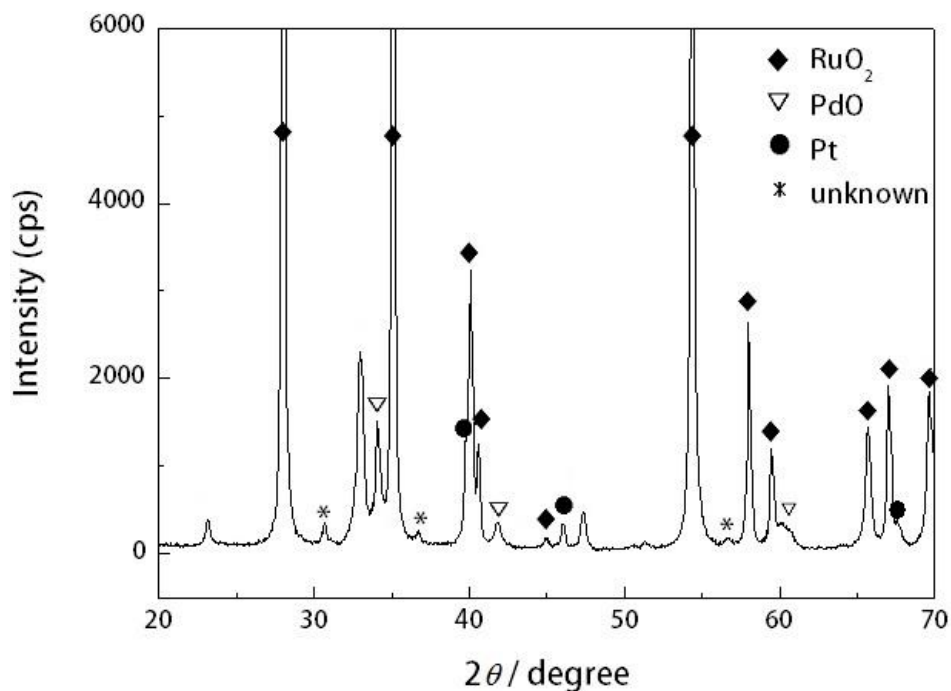
Figure 3.12 XRD pattern of RuO_2-(Pd10wt%+Pt5wt%)$La_{0.6}Sr_{0.4}CoO_3$ after ball milling.

3.4 Sensing properties of the sensor elements

From previous study [49], the amperometric CO sensor on the basis of the oxide ion pumping current changes in a $LaGaO_3$-based oxide was investigated. This perovskite-based sensor showed high sensitivity and good selectivity to CO compared to that against the coexisting gases such as CO_2 and CH_4 by a combination of the inactive and active electrode catalysts, Au10wt%-ITO955 and RuO_2-LSC64, respectively. Moreover, the sensitivity to CO could be further improved by addition of small amount (5 mol%) of Fe into Mg sites of LSGM8282. Therefore, the further studies in this work were focused on the effect of Fe dopant into $LaGaO_3$-based electrolytes including with the study of their cross-sensitivities and the effect of temperature dependence on CO sensitivity.

3.4.1 SEM images of Au10wt%-ITO955 inactive and RuO$_2$-LSC64 active electrodes of the sensor element

Before sensing study, the morphologies of both electrode catalysts painted on each side of Fe-doped LaGaO$_3$ membrane surface were shown in Figure 3.13.

Cross section   **Surface**
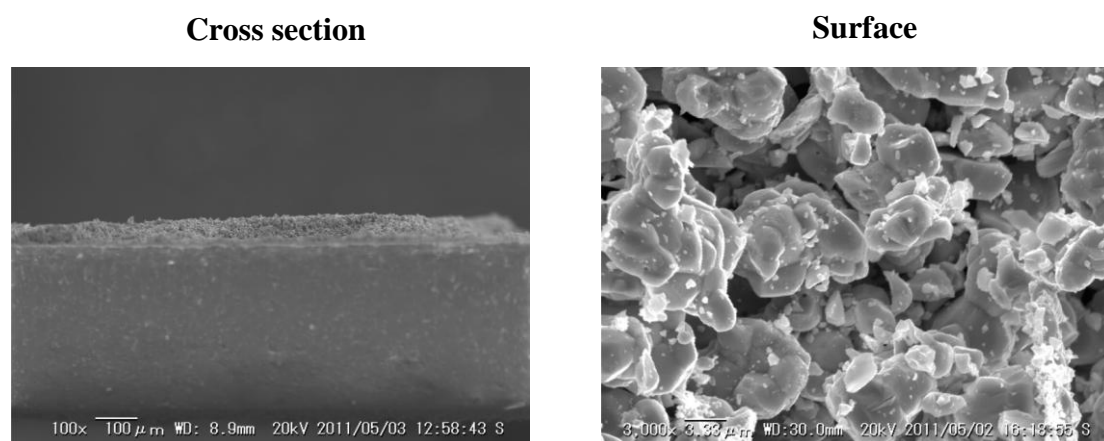
(a) Au10wt%-In$_{0.95}$Sn$_{0.05}$O$_{1.5}$ inactive electrode

Cross section   **Surface**
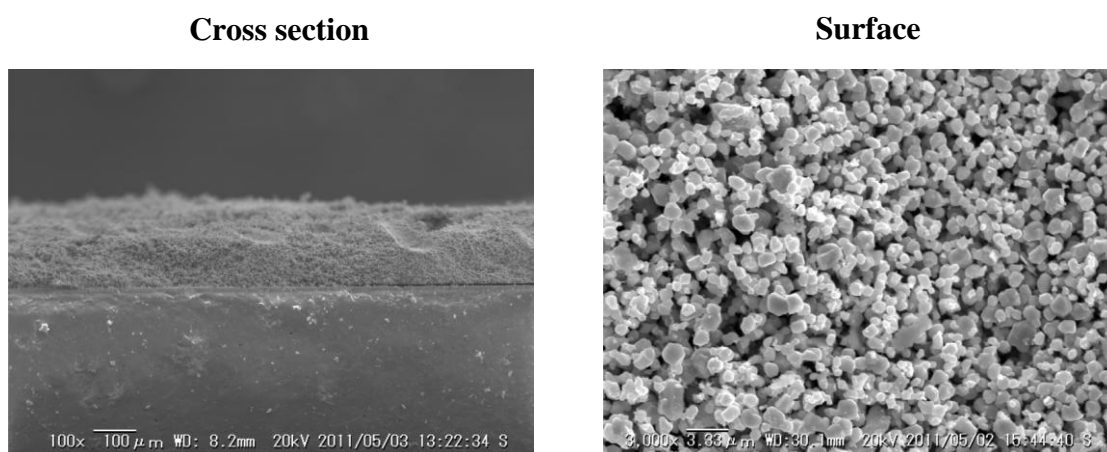
(b) RuO$_2$-La$_{0.6}$Sr$_{0.4}$CoO$_3$ active electrode

Figure 3.13 SEM images of cross section and surface of (a) Au10wt%-ITO955 inactive and (b) RuO$_2$-LSC64 active electrode.

Since our sensor was a sandwich type where an electrolyte coupled with two different electrode materials, these electrodes under the sensing study were exposed

with the same gas environment. The same electrochemical reactions could be possibly occurred on both sides of sensor. Thus, the morphology and catalytic property of these two electrodes played important role to sensing mechanism of the sensor. Due to RuO_2-LSC64 was connected to the positive terminal of external voltage source, this electrode had to be active to CO oxidation based on the oxygen pumping principle [25]. Therefore, the particle size and thickness of electrodes have to be considered. In case of active electrode (active to oxidation reaction), the smaller particle size and thicker electrode thickness than inactive one (inactive to CO oxidation) are required in order to increase the active electrode surface and catalytic activity to CO oxidation.

From Figure 3.13, the large differences in particle size and thickness of electrode between both electrodes were observed. Evidently, the particle size of Au10wt%-ITO955 electrode is larger than 6 μm, but that of RuO_2-LSC64 is ca. 1 μm. The thickness of electrodes is ca. 60 and 100 μm for Au10 wt%-ITO955 and RuO_2-LSC64, respectively. Therefore, the particle size and thickness of electrode are acceptable from the chemical activity requirements for oxidation of CO.

At the beginning of this study, the CO sensing measurement was investigated with different types of oxide ion electrolytes: 8YSZ, 15SDC and LSGMF828155 coupled with the same combination of electrodes as mentioned above. In case of 8YSZ and 15SDC, both of them were used by no purification and pressed into pellets. The sensing performances of these sensors were studied by exposure of sample gas (CO mixed with air) with 25, 50, 500 and 1000 ppm of CO gas concentration into the chamber at 500°C and recorded the current change from base gas to sample gas. Their response curves versus various CO concentrations were demonstrated in Figure 3.14. It was shown that the current outputs of the sensor increased quickly upon switching from the reference gas (air) to the sample gas and the response increases with increasing CO concentration.
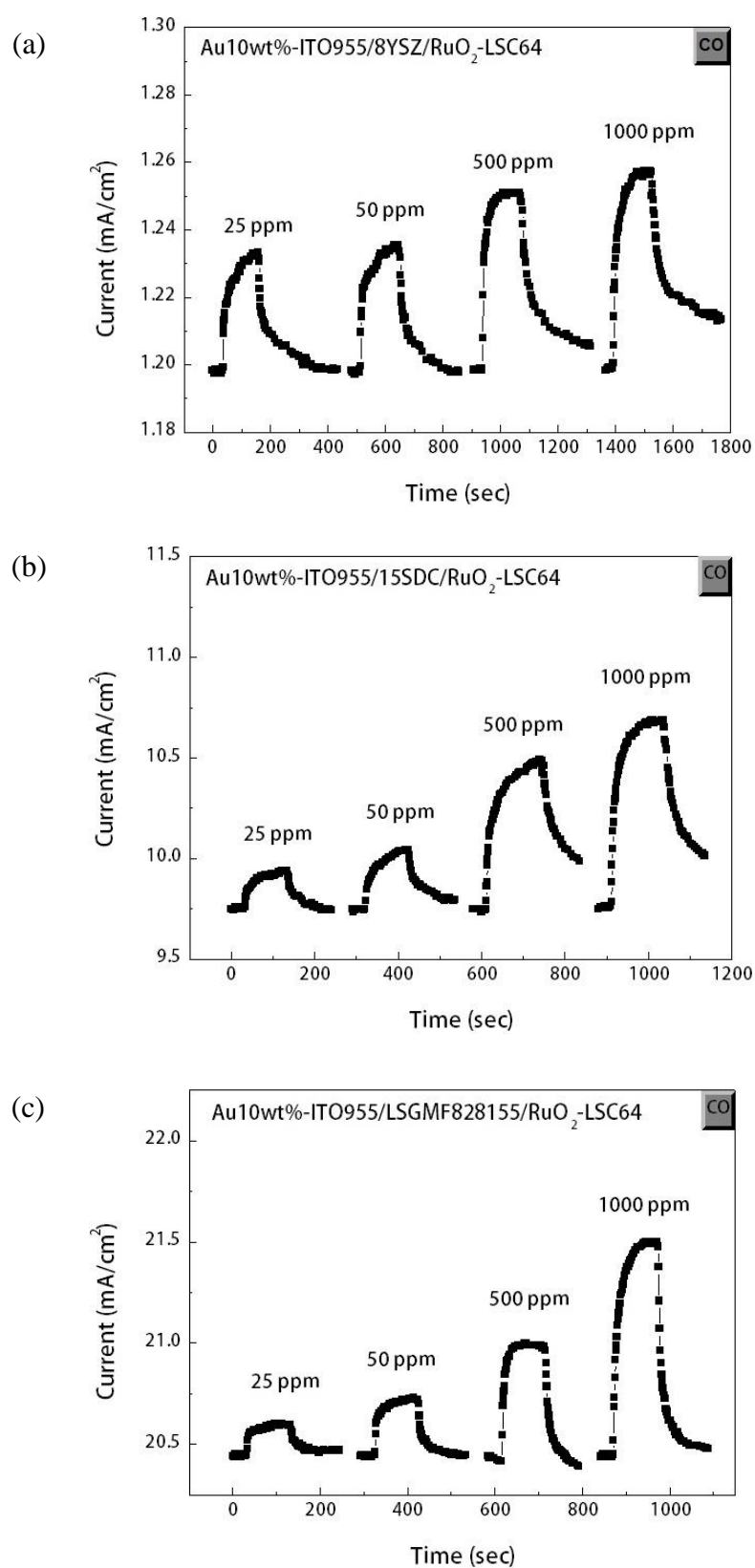
Figure 3.14 The response curves corresponding to various CO concentrations of sensors using (a) 8YSZ, (b) 15SDC and (c) LSGMF828155 as electrolyte at 500°C.
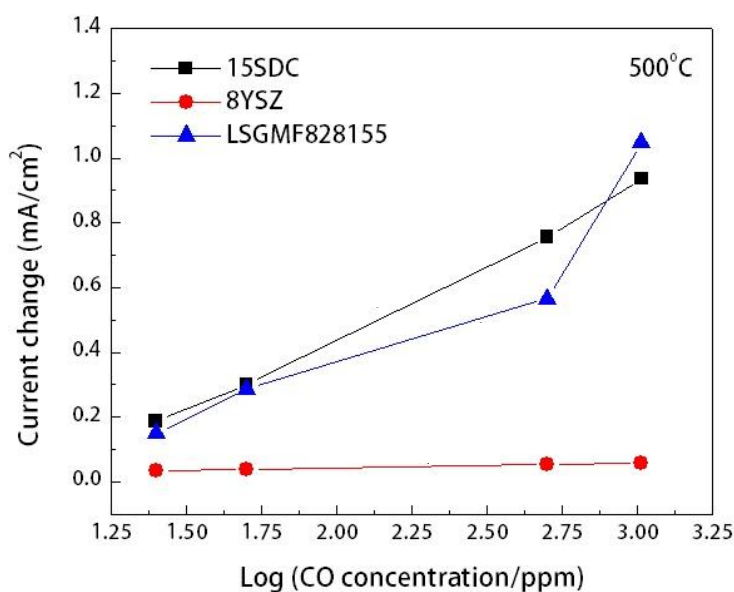
Figure 3.15 The current changes against CO concentration of the sensor with different types of electrolytes at 500°C.

The current changes of each electrolyte were plotted against log CO concentration as shown in Figure 3.15. This figure shows a nearly linear relationship between the current change and log CO concentration. The CO sensitivities of the sensors at 500°C were listed in Table 3.5.

Table 3.5 The CO sensitivity of the sensors with different types of electrolytes coupled with a combination of RuO_2-LSC64 and Au10wt%-ITO955 as active and inactive electrode, respectively at 500°C.

Electrolytes	CO sensitivity (mA/decade) at 500°C
8YSZ	0.01
15SDC	0.46
LSGMF828155	0.48

From this measurement, it is indicated that the sensitivity to CO of the sensors is dependent on the type of electrolyte materials. The CO sensitivity increases in the order LSGMF828155 > 15SDC > 8YSZ. The higher sensitivity of the sensor is obtained by the use of an electrolyte with the higher ionic conductivity. In other words, the ionic conductivity of LSGMF828155 electrolyte is higher than 15SDC and 8YSZ [45]. Since LSGMF828155 exhibits the highest CO sensitivity, the effect of various Fe substitutions into Mg-sites of LaGaO$_3$-based electrolyte on CO sensitivity was subsequently studied.

3.4.2   Optimization of electrolytes

Previous study [49] showed that Fe substitution (5 mol%) into Ga site of LSGM electrolyte exhibited the highest sensitivity to CO compared with that substituted with Co, Ni and Ru. Due to the sensing signal is the oxide ion pumping current through the electrolyte, the effect of Fe content was further investigated.

3.4.2.1 Effect of Fe dopant into LaGaO$_3$-based electrolyte on CO sensitivity with a combination of Au10wt%-ITO955 as cathode and RuO$_2$-LSC64 as anode

La$_{0.8}$Sr$_{0.2}$Ga$_{0.8}$Mg$_{0.2-x}$Fe$_x$O$_{3-\delta}$ oxides (x = 0.05, 0.10, 0.15, 0.20) were synthesized by conventional SSR in order to use as electrolytes of the sensing cell. The synthesized electrolyte discs were named as LSGMF828155, LSGMF82811, LSGMF828515 and LSGF8282 which is the highest amount of Fe substitution in this series. All the synthesized discs were polished with a diamond wheel in order to reduce the thickness to 0.4 mm. Afterwards, cathode catalyst (Au10wt%-ITO955) was painted on one side and another side was painted by anode (RuO$_2$-LSC64). The sensor element was then annealed at 1000°C for 1 h and set up with Au mesh and Pt mesh, respectively. The CO sensing measurements of each electrolyte were performed at the operating temperatures ranging from 300°C to 500°C. The results were shown in Figure 3.16 and summarized in Table 3.6.
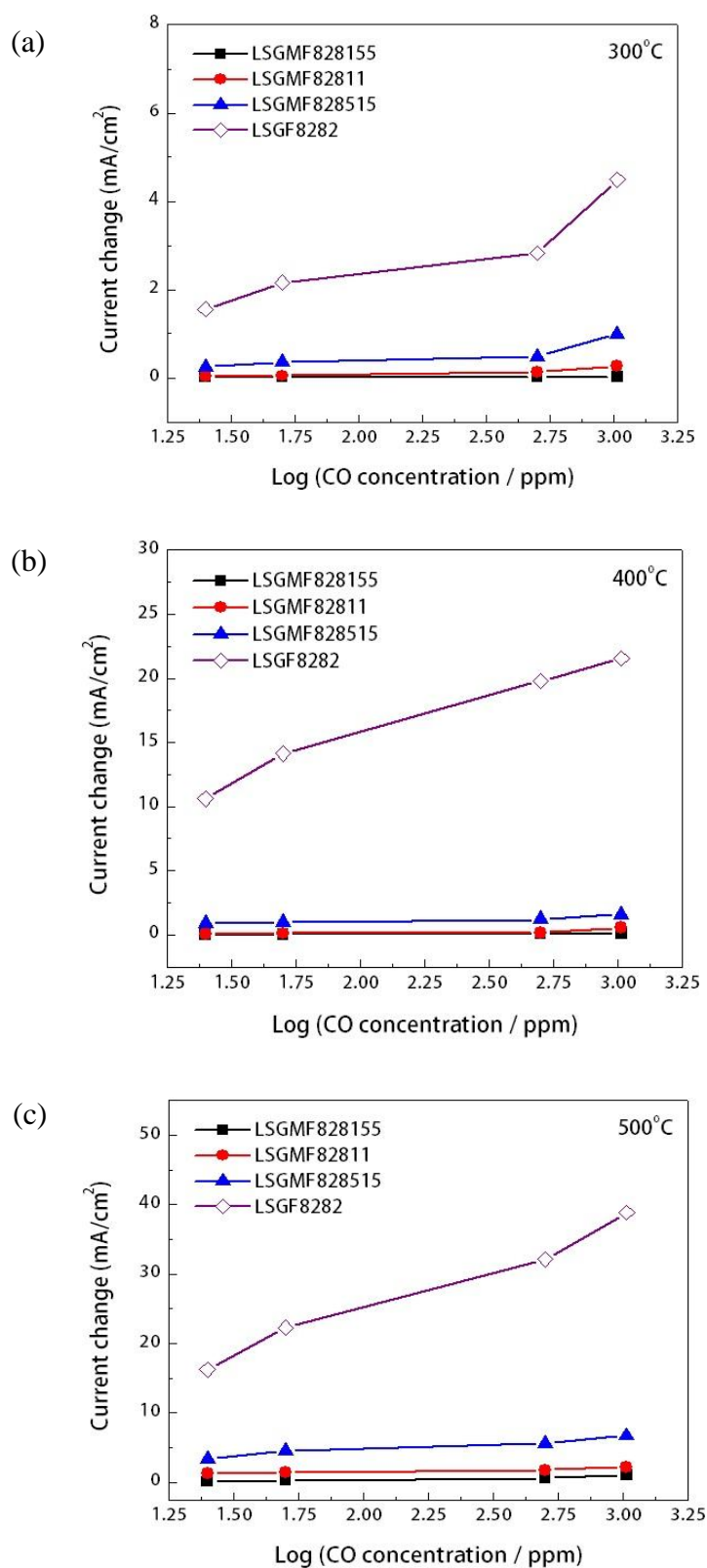
Figure 3.16 Plot of current changes with various CO concentration of $La_{0.8}Sr_{0.2}Ga_{0.8}Mg_{0.2-x}Fe_xO_3$ (x = 0.05, 0.10, 0.15, 0.2) sensor at operating temperatures (a) 300°C, (b) 400°C and (c) 500°C.

Table 3.6 Summary of CO sensitivity of $La_{0.8}Sr_{0.2}Ga_{0.8}Mg_{0.2-x}Fe_xO_3$ (x = 0.05, 0.10, 0.15, 0.20) sensors at operating temperatures ranging from 300°C to 500°C. The CO concentrations are in the range 25 ppm to 1000 ppm.

$La_{0.8}Sr_{0.2}Ga_{0.8}Mg_{0.2-x}Fe_xO_3$ electrolytes	CO sensitivity (mA/decade)		
	300°C	400°C	500°C
x = 0.05	0.01	0.05	0.48
x = 0.10	0.13	0.24	0.50
x = 0.15	0.37	0.38	1.80
x = 0.20	1.50	6.47	12.87

Table 3.6 revealed that Fe contents in LSGMF series have an effect on CO sensitivity of the sensor at each operating temperature. With increasing the amounts of Fe substitution in Mg-site of LSGM8282 electrolytes, the sensitivities to CO and their response times increase (as presented in Appendix B). Doping with maximum ratio at 20 mol% of Fe into Mg-site (LSGF8282) showed the highest sensitivity to CO. In other words, the sensitivity increased with increasing of Fe amount. Figure 3.17, the correlation between CO sensitivity, 90% response time and Fe contents at 400°C of LSGMF series was represented and the data was listed in Table 3.7.
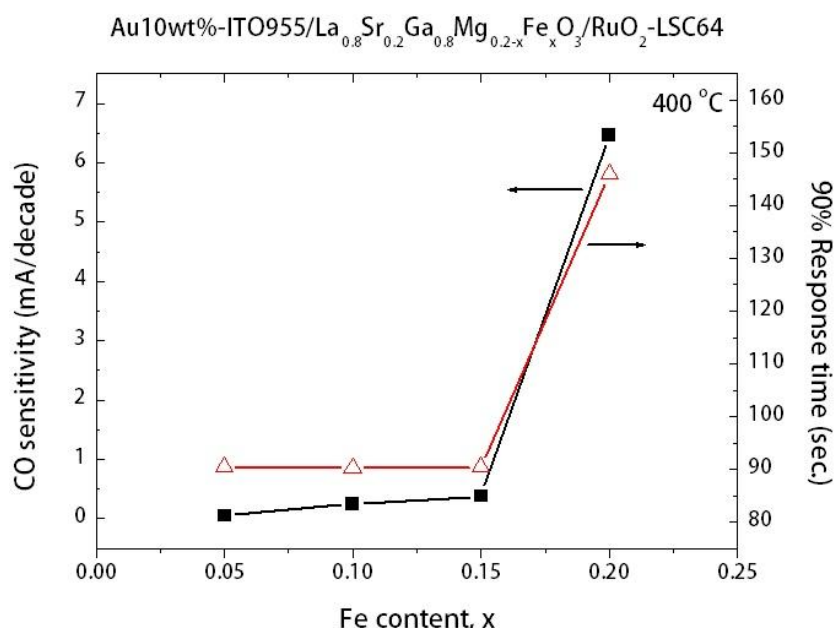
Figure 3.17 The CO sensitivity and 90% response time as a function of Fe content in $La_{0.8}Sr_{0.2}Ga_{0.8}Mg_{0.2-x}Fe_xO_3$ (x = 0.05, 0.1, 0.15, 0.2) electrolytes at 400°C.

Table 3.7 The CO sensitivity and 90% response time as a function of Fe content in $La_{0.8}Sr_{0.2}Ga_{0.8}Mg_{0.2-x}Fe_xO_3$ (x = 0.05, 0.1, 0.15, 0.2) electrolytes to CO concentration ranging from 25 ppm to 1000 ppm at 400°C.

Fe contents, x	Abbreviations	CO sensitivity (mA/decade) at 400°C	T_{90} (sec)
x = 0.05	LSGMF828155	0.05	90.41
x = 0.10	LSGMF82811	0.24	90.19
x = 0.15	LSGMF828515	0.38	90.37
x = 0.20	LSGF8282	6.47	145.98

This table revealed that the CO sensitivity increases in the order LSGF8282 > LSGMF828515 > LSGMF82811 > LSGMF828155. As mentioned above, the higher sensitivity of the sensor is obtained by the use of an electrolyte with the higher ionic conductivity [45]. In other words, the ionic conductivity of LSGF8282 electrolyte is higher than that of LSGMF ones. In addition, Ishihara et al.

have reported that the substitution of Fe^{3+} at Mg^{2+} site in LSGM could be improved the ionic conductivity [35]. Even though, the substitution of Mg^{2+} with Fe^{3+} resulted in the decreased content of oxygen vacancies. The improved ionic conductivity could be explained by the improved mobility of the oxide ions as reported by Yoo et al. [50]. Therefore, increasing amount of Fe content into LSGM tends to increase the ionic conduction of LSGMF series. From the result of this study, it is shown that LSGF8282 exhibits the highest CO sensitivity, further study on CO sensing performances was continued by varying Fe contents in Ga-site of $La_{0.8}Sr_{0.2}GaO_3$ as electrolytes.

Figure 3.18 illustrated the plot of current changes as a function of CO concentration of $La_{0.8}Sr_{0.2}Ga_{1-x}Fe_xO_3$ (x = 0.10, 0.15, 0.20, 0.30) sensor at operating temperatures (a) 300°C, (b) 400°C and (c) 500°C and the data was summarized in Table 3.8.
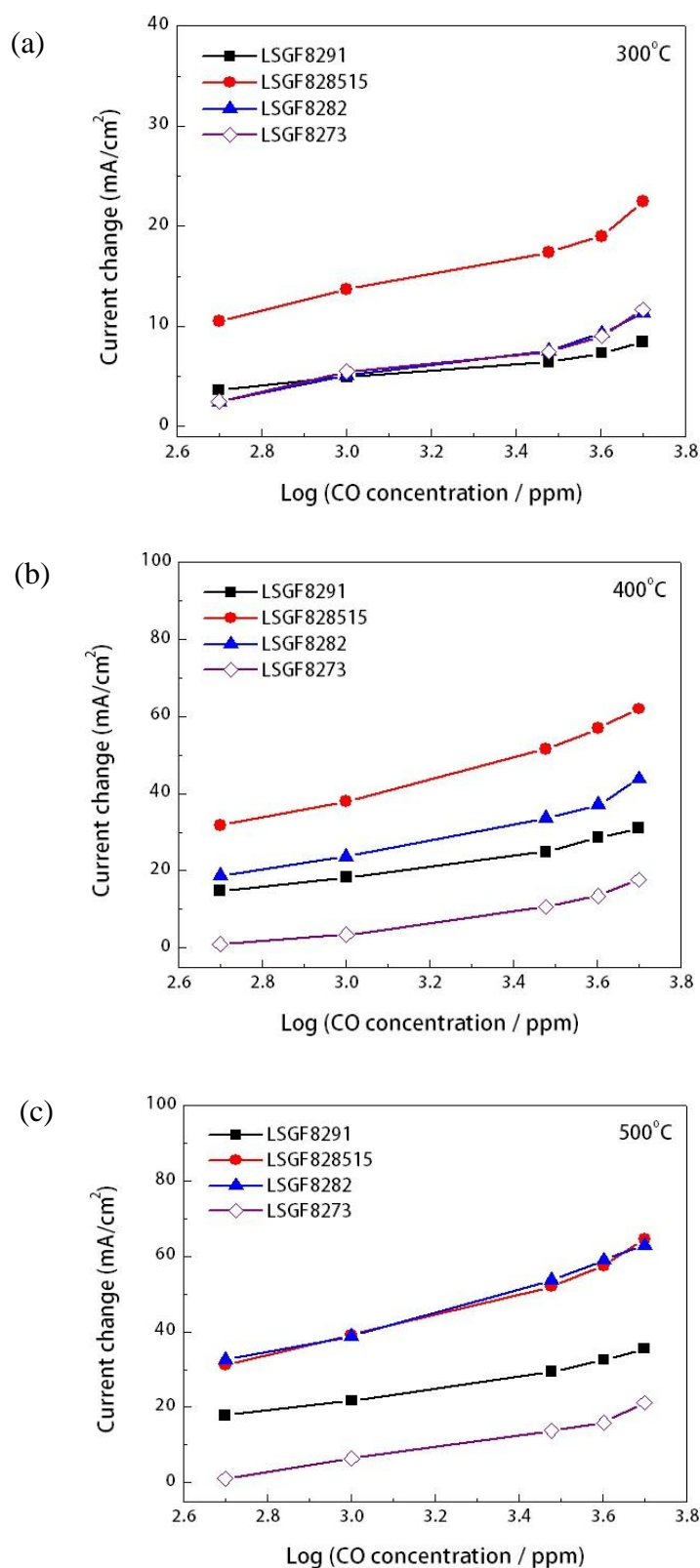
Figure 3.18 Plot of current changes with CO concentration of $La_{0.8}Sr_{0.2}Ga_{1-x}Fe_xO_3$ (x = 0.10, 0.15, 0.20, 0.30) sensor at operating temperatures (a) 300°C, (b) 400°C and (c) 500°C.

Table 3.8 Summary of CO sensitivity of $La_{0.8}Sr_{0.2}Ga_{1-x}Fe_xO_3$ (x = 0.10, 0.15, 0.20, 0.30) sensors at operating temperatures ranging from 300°C to 500°C. The CO concentrations are in the range 500 ppm to 5000 ppm.

$La_{0.8}Sr_{0.2}Ga_{1-x}Fe_xO_3$ electrolytes	CO sensitivity (mA/decade)		
	300°C	400°C	500°C
x = 0.10	4.35	15.79	17.20
x = 0.15	10.59	29.55	31.47
x = 0.20	7.92	23.19	30.52
x = 0.30	7.81	15.91	18.32

Table 3.8 revealed that all of LSGF sensors exhibited the higher sensitivities to CO than that of LSGMF ones. Moreover, the amounts of Fe in LSGF series had an effect on CO sensitivity of the sensor and exhibited the same trends at each operating temperature. The sensitivities increase with increasing of Fe concentration up to 15 mol% in Ga-site (LSGF828515). Above x > 0.15, the sensitivities to CO decrease. This could be explained that LSGF compounds with large amount of Fe exhibited the lower ionic conductivities. This resulted from the partial formation of Fe^{4+} ($r_{Fe^{4+}}$ = 0.585 Å) within LSGF membranes [42] which decreased the content of oxygen vacancies. Figure 3.19 represented the correlation between CO sensitivity and 90% response time corresponding to Fe contents at 400°C.
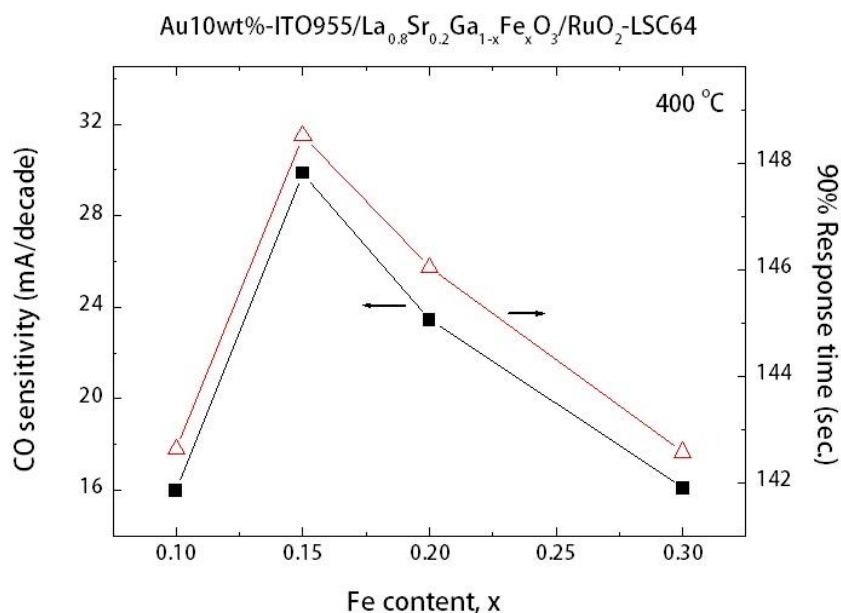
Figure 3.19 The CO sensitivity and 90% response time as a function of Fe content in $La_{0.8}Sr_{0.2}Ga_{1-x}Fe_xO_3$ (x = 0.10, 0.15, 0.20, 0.30) electrolytes at 400°C.

It can be seen that LSGF828515 exhibits the highest CO sensitivity compared with that of other compositions in this series. The detail of this figure was listed in Table 3.9.

Table 3.9 The CO sensitivity and 90% response time as a function of Fe content in $La_{0.8}Sr_{0.2}Ga_{1-x}Fe_xO_3$ (x = 0.10, 0.15, 0.20, 0.30) electrolytes to CO concentration ranging from 500 ppm to 5000 ppm at 400°C.

Fe contents, x	Abbreviations	CO sensitivity (mA/decade)	T_{90} (sec)
x = 0.10	LSGF8291	15.79	142.62
x = 0.15	LSGF828515	29.55	148.51
x = 0.20	LSGF8282	23.19	146.03
x = 0.30	LSGF8273	15.91	142.57

From this table, it was shown that LSGF sensors exhibits high response to CO. The 90% response of current value was achieved within 2-3 min including the time for exchanging the gas atmosphere inside the measurement

chamber. Therefore, the response time of these sensors are a little longer. Nevertheless, it is reasonable to confirm that the observed responses of Fe-doped LaGaO$_3$ are fast for CO detection. The reproducible response characteristics curves at each concentration of CO can be seen in both LSGMF and LSGF series.

To explain the sensing mechanism in both LSGMF and LSGF series, the planar amperometric sensor attached with two different types of electrodes which are Au10wt%-ITO955 (cathode) and RuO$_2$-LSC64 (anode) form the electrochemical cell as follows:

$$\text{Air, Au10wt\%-ITO955} \mid \text{LSGMF or LSGF} \mid \text{RuO}_2\text{-LSC64, CO} \qquad (3.1)$$

The left side of the cell is an oxygen-sensitive half-cell and the right side of the cell is a CO-sensitive half-cell in which the electrode potential depends on the CO concentration. The electrochemical reactions occur at the three-phase boundary of electrode (Au10wt%-ITO955 or RuO$_2$-LSC64), electrolyte (LSGMF or LSGF) and gas phase as the following two electrochemical reactions.

The oxidative reaction: $\qquad CO + 2O^{2-} \leftrightarrow CO_2 + 4e^-$ $\qquad\qquad\qquad$ (3.2)

The reductive reaction: $\qquad O_2 + 4e^- \leftrightarrow 2O^{2-}$ $\qquad\qquad\qquad\qquad$ (3.3)
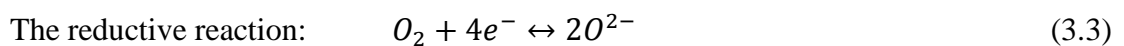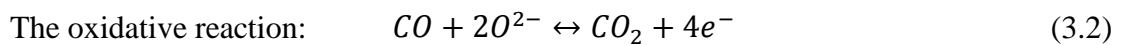
Since this is a planar sensor design, both electrodes of each sensor are exposed to a homogenous environment. These two reactions will occur at each electrode. From the previous work [49], it is found that RuO$_2$-LSC64 is highly sensitive to CO oxidation and Au10wt%-ITO955 is an oxygen-sensitive electrode related to dissociation of oxygen molecule to oxide ion. Hence, it can be expected that reaction (3.1) and (3.2) are dominant on RuO$_2$-LSC64 and Au10wt%-ITO955, respectively as illustrated in Figure 3.20.
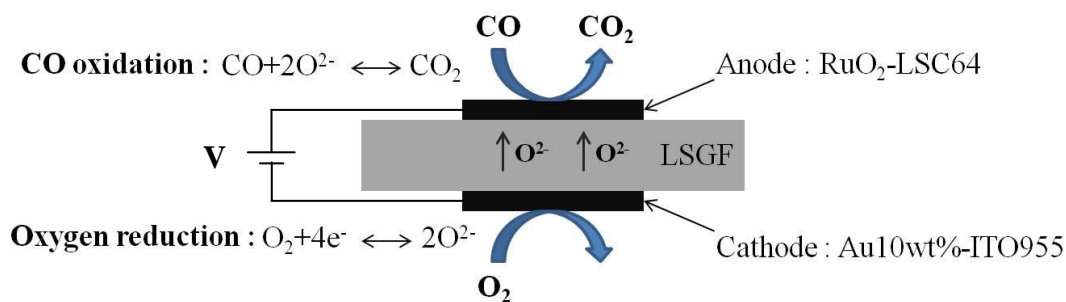
Figure 3.20 The expected reaction mechanism of Au10wt%-ITO955|LSGF|RuO$_2$-LSC64.

Because a local oxygen gradient will be formed, the presence of CO concentration in the amperometric sensor has an effect on the oxygen pumping current. With increasing CO concentration, the oxygen pumping current increases. Since RuO$_2$-LSC64 electrode is always positive, the oxygen concentration on this electrode is always smaller than that on Au10wt%-ITO955 electrode. This suggests that the RuO$_2$-LSC64 is more active to CO oxidation. Therefore, the CO oxidation reaction takes place at anode (RuO$_2$-LSC64) and the oxygen reduction occurs at cathode (Au10wt%-ITO955) as we expected.

3.4.2.2 XRD Characterization of sensing elements

It is necessary to investigate the sensor stability under the sensing condition; hence the XRD analysis of the sensor before and after sensing measurement was studied. Figure 3.21(a) and Figure 3.21(b) showed the XRD pattern of RuO$_2$-LSC64 and Au10wt%-ITO955 coated on LSGF828515 electrolyte before and after sensing measurement, respectively. From this figure, there is no any additional phase which displayed the interaction between electrode and electrolyte taken place after sensing measurement. It is evident that the LSGF828515 is quite stable under sensing condition.
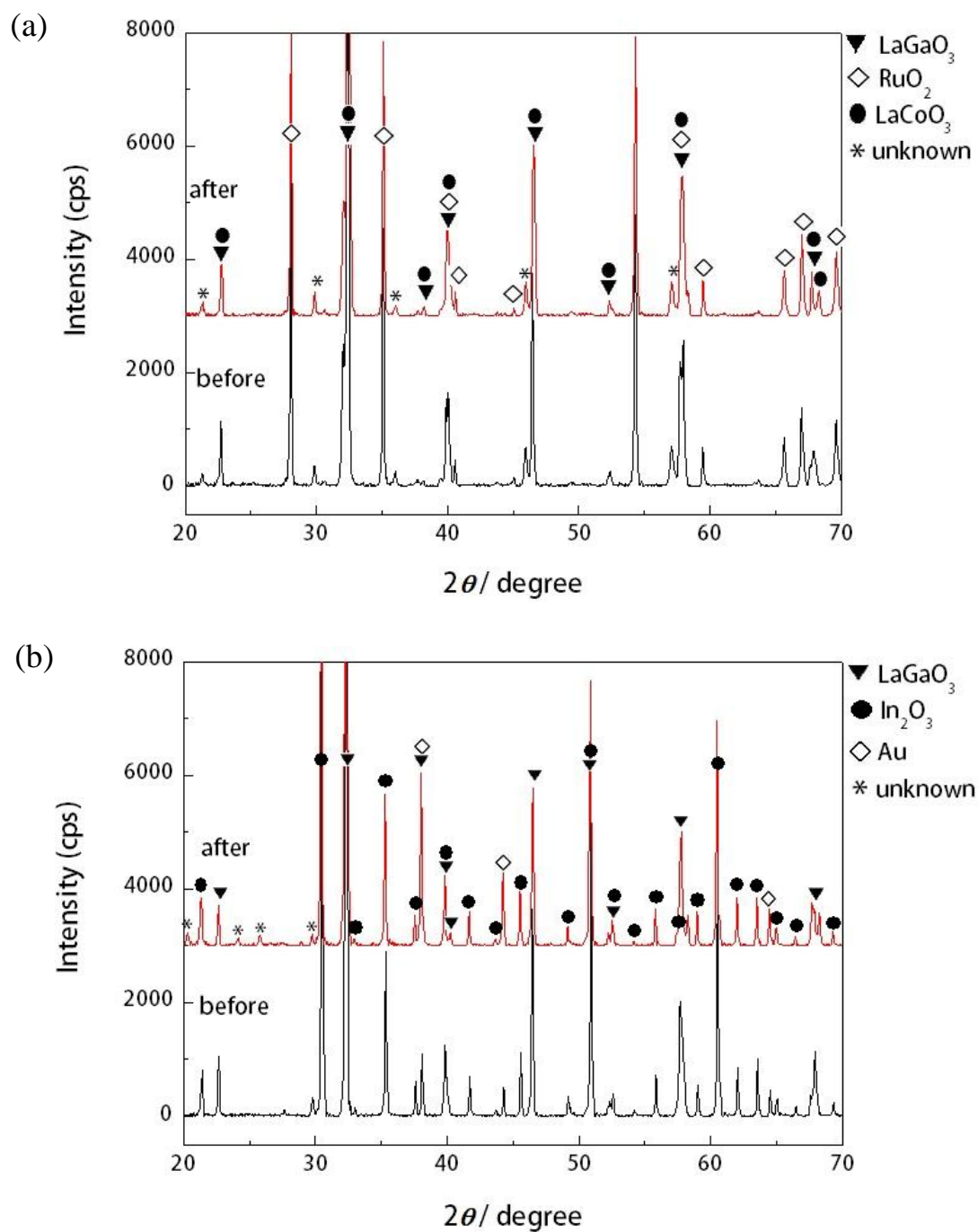
Figure 3.21 XRD pattern of (a) LSGF828515 electrolyte painted with RuO$_2$-LSC64 and (b) LSGF828515 painted with Au10wt%-ITO955, before and after sensing.

3.4.3 Effect of temperature dependence on CO sensitivity of the sensing element

The effect of operating temperature on the sensitivity to CO of the sensors was also investigated. As shown in Figure 3.22, the CO sensitivities of all sensors coupled with Au10wt%-ITO955 and RuO_2-LSC64 increased with elevating the operating temperatures.
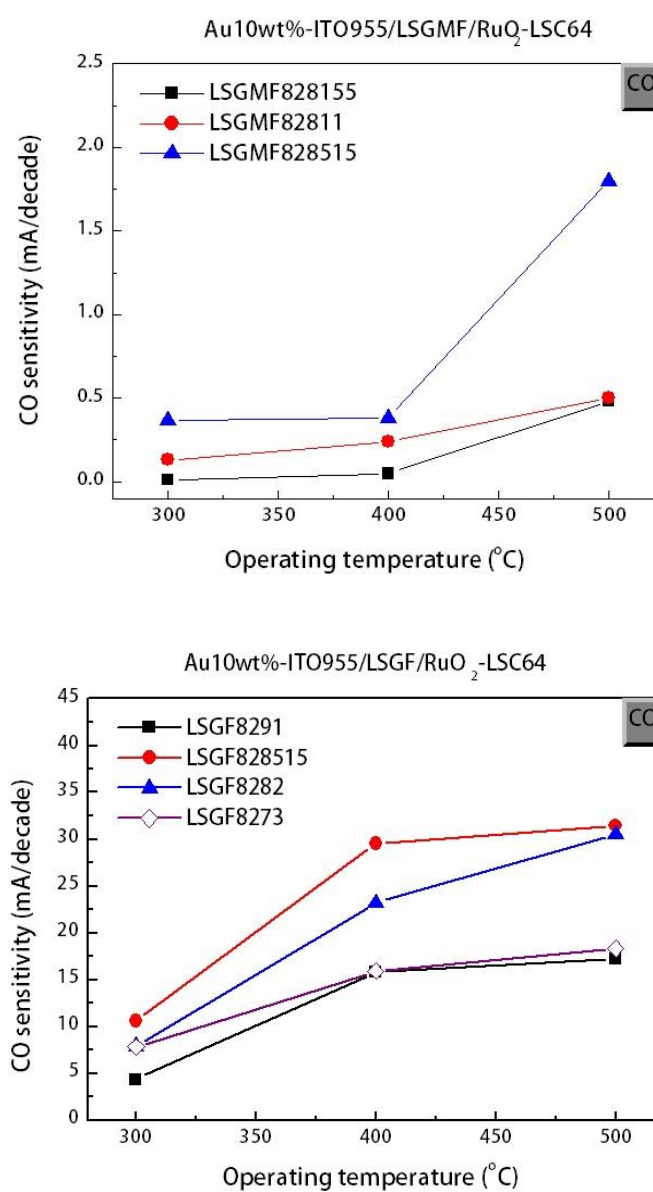
Figure 3.22 Temperature dependence on CO sensitivity of the measurement cells using (Top) LSGMF series and (Bottom) LSGF series as electrolytes.

From this figure, it was shown that the sensitivity to CO increased with increasing temperature from 300°C to 500°C. This can be explained by the following reason: at the higher operating temperature, the electrode reaction proceeds much faster [15, 40]. In other words, the catalytic activity of anode to the oxidation reaction increases with the increasing temperature. Thus, it is evident that the increasing CO sensitivity of all sensors with elevating temperature of operation was affected by the higher catalytic activity of the active RuO_2-LSC64 electrode to CO oxidation at higher temperature.

3.4.4 Cross-sensitivities of CO sensor for CO_2, CH_4 and H_2 of the optimized sensing element

In the exhaust gas, there is not only carbon monoxide, but also other coexisting gases such as carbon dioxide, hydrocarbons, etc. Therefore, effect of these interference gases to sensor response is including investigated. The cross-sensitivities of LSGF828515 sensor for CO_2, CH_4 and H_2 were monitored in this study.
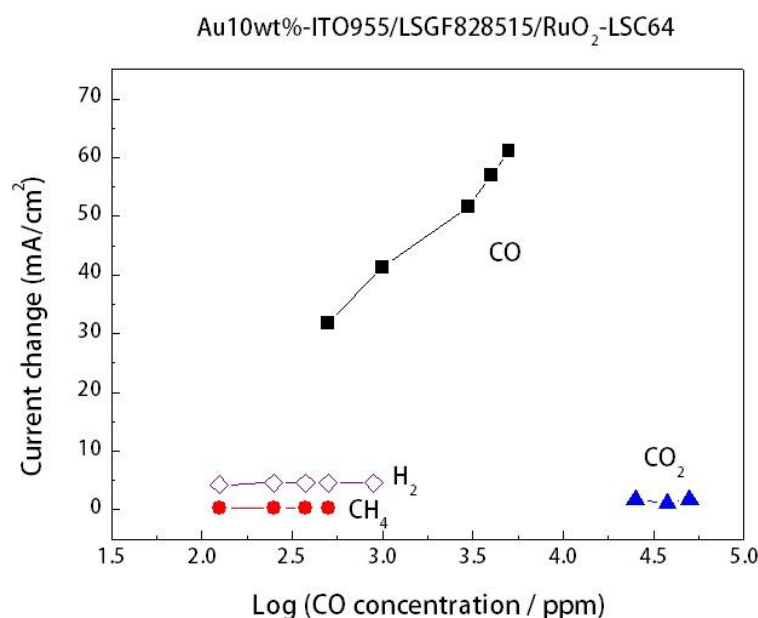
Figure 3.23 Cross-sensitivity of LSGF828515-based sensor to various coexisting gases at 400°C.

Figure 3.23 displayed the sensitivities of the sensor to the interference gases. From this figure, the sensitivity to CO is obviously high compared with H_2, CH_4 and CO_2, respectively. In other words, the sensor exhibited the very high response to CO and almost no response to other gases at the same condition. The sensitivity and selectivity of this sensor were listed in Table 3.10.

Table 3.10 Sensitivity and selectivity to various gases of LSGF828515 sensor at the operating temperature 400°C.

| Gases	Concentration (ppm)	Sensitivity (mA/decade) at 400°C	Selectivity
CO	500-5000	27.79	1.00
CO_2	25000-50000	-0.26	0.01
CH_4	125-500	0	0.00
H_2	125 - 890	0.38	0.01

It is clear that this LSGF828515 sensor with a combination of inactive Au10wt%-ITO955 and active RuO_2-LSC64 is very suitable to detect carbon monoxide.

In addition, other additional work of this research on the improvement active electrodes on CO sensitivity was investigated along with the sensing measurements of the optimized sensor. That was the modification of anode electrode to enhance its catalytic activity by addition of other additives into LSC64 and study the sensor response using LSGMF828155 as electrolyte at that time.

3.4.5 Effect of additives into LSC64 electrode on sensing measurements of the sensor

It is well-known that both Pt and Pd are active for the oxidation reaction, they were then used as additives to modify active electrode. The (Pt1wt%) and (Pd10wt%+Pt5wt%)LSC64 were firstly prepared, subsequently mixing with RuO_2 by ball milling was done. Pt or Pd-Pt electrode was coated on the anode side of LSGMF828155 electrolyte and Au10wt%-ITO955 which was fixed as cathode was

painted on another side. The sensor responses to CO of these sensors were monitored (as shown in Appendix B) and CO sensitivities of each sensor were shown in Figure 3.24 and summarized in Table 3.11.
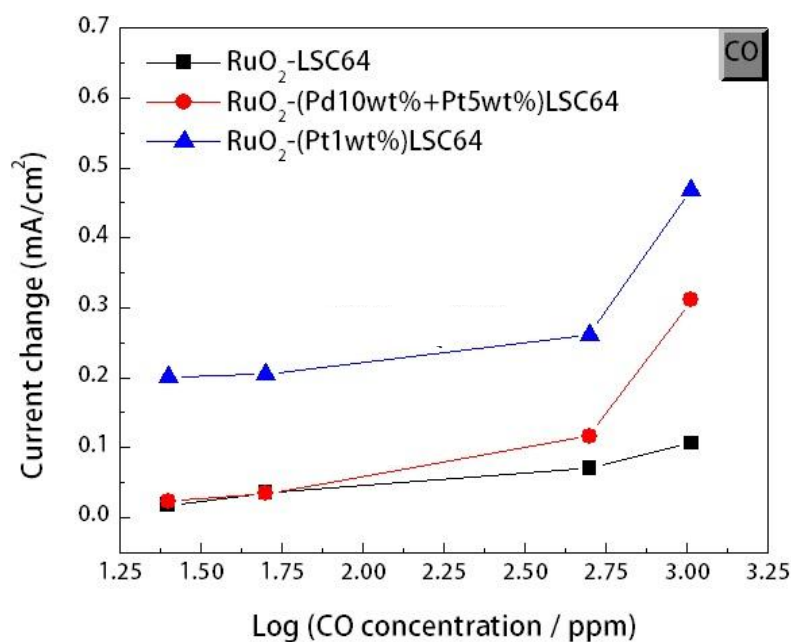
Figure 3.24 Oxygen pumping current change of the CO sensor with undoped and additives-doped active electrodes. The Au10wt%-ITO955 was fixed as inactive electrode and the operating temperature was 400°C.

Table 3.11 The CO sensitivity of LSGMF828155 sensors with the combinations of various anode materials as active electrode by fixing Au10wt%-ITO955 as inactive electrode at 400°C.

Anode materials	CO sensitivity (mA/decade) at 400°C
RuO_2-LSC64	0.05
RuO_2-(Pt1wt%)LSC64	0.13
RuO_2-(Pd10wt%+Pt5wt%)LSC64	0.15

From this table, both modified anodes influenced to the sensitivity to CO. The addition of small amount of additives to LSC64 was improved the catalytic activity of anode to CO oxidation and increasing amount of additive to LSC64 was further enhanced the CO sensitivity. As seen in Table 3.11, the sensitivity became three times larger compared with non-additives one. It is clear that the sensitivity to CO can also be further enhanced by improving the oxidation activity of anode.

CHAPTER IV

CONCLUSIONS

4.1 Conclusions

The planar-type amperometric electrochemical sensors based on Fe-doped lanthanum gallate electrolyte were mainly studied in this work and their sensing property is described and following results are obtained.

(1)   The Fe-doped $LaGaO_3$-based perovskites were successfully synthesized and operated in the amperometric mode as electrolytes in this study. Sensors coupled with a combination of the optimized electrode catalysts were stable and showed fast responses in the operating temperatures range from 300°C to 500°C. It is revealed that the highest sensitivity to CO can be achieved when $La_{0.8}Sr_{0.2}GaO_3$ was doped with 15 mol% Fe into Ga-site (denoted as LSGF828515).

(2)   Increasing operating temperatures from 300°C to 500°C can further improved the sensitivity to CO. In other words, the CO sensitivity increases with increasing the operating temperature. The highest sensitivity was obtained at 500°C.

(3)   The optimized sensor also showed very high selectivity to CO and independent response to other typical interference gases.

(4)   The additions of additives into $La_{0.6}Sr_{0.4}CoO_3$ (LSC64) can further improved CO sensitivity. The Pt and Pd-Pt doped LSC64 were successfully prepared by conventional impregnation method. In addition, increasing amounts of additives into LSC64 were also effective for enhancing CO sensitivity.

It can be concluded that the enhancement of CO sensitivity of the sensor seems to be influenced from:

(i)   the amounts of Fe dopant into $LaGaO_3$ electrolyte,

(ii)   the operating temperatures and

(iii)   the modification of LSC64 anode.

4.2 Suggestions for future work

From the experiment results, the additional works should be further done in order to improve the sensing performance of the CO sensor and make them more widely useful which are shown as follows:

1. Sensing performance of other modified anodes and other types of anode materials.
2. Sensing performance of other types of oxygen ion conducting electrolytes.
3. Effect of sensor structure for miniaturization.
4. Long term stability under humidified condition.

REFERENCES

[1] Raub, J.A., Mathieu-Nolf, M., Hampson, N.B., and Thom, S.R. Carbon monoxide poisoning – a public health perspective. Toxicology 145 (2000): 1-14.

[2] Wikipedia. Carbon Monoxide Poisoning. [Online]. (n.d.). Available from: http://en.wikipedia.org/wiki/Carbon_monoxide_poisoning.html [2012, February 23]

[3] Thomson, J.L., and Kardel, T. Intoxication at home due to carbon monoxide production from gas water heaters. Forensic Science International 36 (1988): 69-72.

[4] Osawa, M., Horiuchi, H., Yoshida, K., Tada, T., and Harada, A. A death in a stationary vehicle whilst idling: unusual carbon monoxide poisoning by exhaust gases. Legal Medicine 5 (2003): S132-S134.

[5] Chang, W.R., and Cheng, C.L. Carbon monoxide transport in an enclosed room with sources from a water heater in the adjacent balcony. Building and Environment 43 (2008): 861-870.

[6] Cadi, M.A.E., Khabbal, Y., and Idrissi, L. Carbon monoxide poisoning in Morocco during 1999-2007. Journal of Forensic and Legal Medicine 16 (2009): 385-387.

[7] Wikipedia. Sensor. [Online]. (n.d.) Available from: http://en.wikipedia.org/wiki/Sensor.html [2012, February 25]

[8] Nemov, T.G., Yordanov, S.P. in Ceramic Sensors. Technology and Applications. Technomic Publishing Co., Lancaster-Basel (1996).

[9] Capone, S., Forleo, A., Francioso, L., Rella, R., Siciliano, P., Spadavecchia, J., Presicce, D.S., and Taurino, A.M. Solid state gas sensors: state of the art and future activities. Journal of Optoelectronics and advanced materials 5 (2003): 1335-1348.

[10] Römer, E. Amperometric NO_x-sensor for combustion exhaust gas control. Ph.D. thesis, University of Twente, 2001.

[11] Sundmacher, K., Rihko-Struckmann, L.K., Galvita, V. Solid electrolyte membrane reactors: status and trends. Catalysis Today 104 (2005): 185-199.

[12] Sunarso, J., Baumann, S., Serra, J.M., Meulenberg, W.A., Liu, S., Lin, Y.S., and Diniz da Costa, J.C. Mixed ionic-electronic conducting (MIEC) ceramic-based membranes for oxygen separation. Journal of Membrane Science 320 (2008): 13-41.

[13] Wincewicz, K.C., and Cooper, J.S. Taxonomies of SOFC material and manufacturing alternatives. Journal of Power Sources 140 (2005): 280-296.

[14] Park, C.O., Fergus, J.W., Miura, N., Park, J., and Choi, A. Solid-state electrochemical gas sensors. Ionics 15 (2009): 261-284.

[15] Jasiṅki, P. Solid-state electrochemical gas sensors. Materials Science-Poland 24 (2006): 269-278.

[16] Weppner, W. Solid-state electrochemical gas sensors. Sensors and Actuators 12 (1987): 107-119.

[17] Miura, N., Lu, G., and Yamazoe, N. Progress in mixed-potential type devices based on solid electrolyte for sensing redox gases. Solid State Ionics 136-137 (2000): 533-542.

[18] Moos, R., Sahner, K., Fleischer, M., Guth, U., Barson, N., and Weimar, U. Solid state gas sensor research in Garmany − a status report. Sensors 9 (2009): 4323-4365.

[19] Shoemaker, E.L., Vogt, M.C., and Dudek, F.J. Cyclic voltammetry applied to an oxygen-ion-conducting solid electrolyte as an active electrocatalytic gas sensor. Solid State Ionics 92 (1996): 285-292.

[20] Göpel, W., Reinhardt, G., and Rösch, M. Trends in the development of solid state amperometric and potentiometric high temperature sensors. Solid State ionics 136-137 (2000): 519-531.

[21] Garzon, F.H., Mukundan, R., and Brosha, E.L. Solid-state mixed potential gas sensors: theory, experiments and challenges. Solid State Ionics 136-137 (2000): 633-638.

[22] Plashnitsa, V. Characterization of the CO sensitivity of electrode materials by solid electrolyte galvanic cells. Dissertation, University Stuttgart, 2004.

[23] Fergus, J.W. Solid electrolyte based sensors for the measurement of CO and hydrocarbon gases. Sensors and Actuators B 122 (2007): 683-693.

[24] Fleming, W. Physical principles governing nonideal behavior of the Zirconia Oxygen Sensor. Journal of the Electrochemical Society 124 (1977): 21-28.

[25] Logothetis, E.M., Visser, J.H., Soltis, R.E., and Rimai, L. Chemical and physical sensors based on oxygen pumping with solid-state electrochemical cells. Sensors and Actuators B 9 (1992): 183-189.

[26] Stetter, J.R. Amperometric gas sensors − a review. Chemical Reviews 108 (2008): 352-366.

[27] Wikipedia. Perovskite (structure). [Online]. (n.d.). Available from: http://en. wikipedia.org /wiki/Perovskite_(structure).html [2012, March 6]

[28] Peña, M.A., and Fierro, J.L.G. Chemical Structures and Performance of Perovskite Oxides. Chemical Reviews 101 (2001): 1981-2017.

[29] Xu, N., Zhao, H., Zhou, X., Wei, W., Lu, X., Ding, W., Li, F. Dependence of critical radius of the cubic perovskite ABO_3 oxides on the radius of A- and B-site cations. International Journal of Hydrogen Energy 35 (2010): 7295-7301.

[30] Iwahara, H. Ionic conduction in perovskite-type compounds in Perovskite Oxide for Solid Oxide Fuel Cells T. Ishihara, ed. (Springer Science+Business Media: New York, 2009) p. 45-49.

[31] Hong, J., Kirchen, P., and Ghoniem, A.F. Numerical simulation of ion transport membrane reactors: oxygen permeation and transport and fuel conversion. [Online]. (n.d.). Available from: http://web.mit.edu/rgd/www/Papers/James 2012ITM.pdf [2012, March 5]

[32] Chang, S.C., Stetter, J.R., Cha, C.S. Amperometric gas sensors. Talanta 40 (1993): 461-477.

[33] Rusmiati, Prijamboedi, B., and Ismunandar. Synthesis and structural properties of Fe doped $La_{0.8}Sr_{0.2}Ga_{0.8}Mg_{0.2}O_{3-\delta}$ (LSGM) as solid electrolyte for solid oxide fuel cell. in: International Conference on Neutron and X-Ray Scattering., Proceeding. A. Ikram, eds. (Indonesia: American Institute of Physics, 2008) p. 172-175.

[34] Ishihara, T., Yamada, T., Arikawa, H., Nishiguchi, H., Takita, Y. Mixed electronic-oxide ionic conductivity and oxygen permeating property of Fe-, Co- or Ni-doped $LaGaO_3$ perovskite oxide. Solid State Ionics 135 (2000): 631-636.

[35] Ishihara, T., Shibayama, T., Honda, M., Nishiguchi, H., Takita, Y. Intermediate temperature solid oxide fuel cells using LaGaO$_3$ electrolyte. II. Improvement of oxide ion conductivity and power density by doping Fe for Ga site of LaGaO$_3$. Journal of the Electrochemical Society 147 (2000): 1332-1337.

[36] Shuala, A.L., Yaremchenko, A.A., Kharton, V.V., Logvinovich, D.I., Naumovich, E.N., Kovalevsky, A.V., Frade, J.R., and Marques, F.M.B. Oxygen permeability of LaGaO$_3$-based ceramic membranes. Journal of Membrane Science 221 (2003): 69-77.

[37] Can, Z.Y., Narita, H., Mizusaki, J., and Tagawa, H. Detection of carbon monoxide by using zirconia oxygen sensor. Solid State Ionics 79 (1995): 344-348.

[38] Narducci, D., Ornaghi, A., and Mari, C.M. CO determination in air by YSZ-based sensors. Sensors and Actuators B 18-19 (1994) 566-568.

[39] Barth, D., Sahibzada, M., Mantzavinos, D., and Metcalfe, I.S. Solid electrolyte sensor for studying the behavior of a partial oxidation catalyst. Solid State Ionics 136-137 (2000): 621-627.

[40] Dutta, A., Ishihara, T., Nishiguchi, H., Takita, Y. Amperometric solid-state gas sensor using LaGaO$_3$ based perovskite oxide electrolyte for detecting hydrocarbon in exhaust gas. II. Improvement of inactive electrode performance. Journal of the Electrochemical Society 151 (2004): H122-H127.

[41] Dutta, A., Ishihara, T., and Nishiguchi, H. An amperometric solid-state gas sensor using a LaGaO$_3$-based perovskite oxide electrolyte for detecting hydrocarbon in exhaust gas. A bimetallic anode for improving sensitivity at low temperature. Chemistry of Materials 16 (2004): 5198-5204.

[42] Dutta, A., Nishiguchi, H., Takita, Y., Ishihara, T., Amperometric hydrocarbon sensor using La(Sr)Ga(Fe)O$_3$ solid electrolyte for monitoring in exhaust gas. Sensors and Actuators B 108 (2005): 368-373.

[43] Dutta, A., and Ishihara, T. Amperometric NO$_x$ sensor based on oxygen pumping current by using LaGaO$_3$-based solid electrolyte for monitoring exhaust gas. Sensors and Actuators B 108 (2005): 309-313.

[44] Dutta, A. and Ishihara, T. An amperometric solid state NO sensor using a LaGaO$_3$ electrolyte for monitoring exhaust gas. <u>Materials and Manufacturing Processes</u> 21 (2006): 225-228.

[45] Bi, Z., Matsumoto, H., and Ishihara, T. Solid-state amperometric CH$_4$ using LsGaO$_3$-based electrolyte. <u>Solid State Ionics</u> 179 (2008): 1641-1644.

[46] Li, X. and Kale, G.M. Influence of thickness of ITO sensing electrode film on sensing performance of planar mixed potential CO sensor. <u>Sensors and Actuators B</u> 120 (2006): 150-155.

[47] Lee, S., Lee, K.S., Woo, S.K., Kim, J.W., Ishihara, T., and Kim, D.K. Oxygen-permeating property of LaSrBFeO$_3$ (B=Co, Ga) perovskite membrane surface-modified by LaSrCoO$_3$. <u>Solid State Ionics</u> 158 (2003): 287-296.

[48] Lee, K.S., Lee, S., Kim, J.W., and Woo, S.K. Enhancement of oxygen permeation by La$_{0.6}$Sr$_{0.4}$CoO$_{3-\delta}$ coating in La$_{0.7}$Sr$_{0.3}$Ga$_{0.6}$Fe$_{0.4}$O$_{3-\delta}$ membrane. <u>Desalination</u> 147 (2002): 439-444.

[49] Ishihara, T., Phawachalotorn, A., Kadowaki, R., and Sanguanruang, O. Solid oxide amperometric CO sensor for monitoring exhaust gas from water heater. <u>Sensors and Materials</u> 22 (2010): 183-192.

[50] Yoo, J.S., Lee, S., Yu, J.H., Woo, S.K., Park, H., Kim, H.G. Fe doping effects on phase stability and conductivity of La$_{0.75}$Sr$_{0.25}$Ga$_{0.8}$Mg$_{0.2}$O$_{3-\delta}$. <u>Journal of Power Sources</u> 193 (2009): 593-597.

[51] Shannon, R.D. Revised effective ionic radii and systematic studies of interatomic distances in halides and chalcogenides. <u>Acta Crystallographica</u> A32 (1976): 751-767.

APPENDICES

APPENDIX A

Tolerance number

Goldschmidt (1926) defined the tolerance limits of the size of ions through a tolerance factor, *t* as equation (A.1)

$$t = \frac{(r_A + r_O)}{\sqrt{2}(r_B + r_O)}$$
(A.1)

where r_A, r_B, and r_O are the radii of respective ions. For the substituted perovskite at A and B site, $A_{1-x}A'_xB_{1-y}B'_yO_{3-\delta}$, r_A and r_B were calculated from the sum of each metal at A site and B site, respectively, time its compositions. The atomic weight, ionic charge, coordination number, and ionic radius of all concerned metals were shown in Table A.1

Table A.1 Ionic charge, coordination number (CN) and ionic radius of related ions in LSGMF and LSGF systems [51].

Site in ABO_3	Element	Charge	CN	Ionic radius (Å)
A site	La	3+	12	1.36
	Sr	2+	12	1.44
B site	Ga	3+	6	0.62
	Mg	2+	6	0.72
	Fe	3+	6	0.645
Oxygen	O	2-	6	1.40

Therefore, as equation A.1 the tolerance number of perovskite compounds such as LSGF8282 was calculated as below.

Tolerance number of LSGF8282 $= \dfrac{(1.36 \times 0.8) + (1.44 \times 0.2) + 1.40}{\sqrt{2}[(0.62 \times 0.8) + (0.645 \times 0.2) + 1.40]} = 0.969$

APPENDIX B

Sensitivity

Sensitivity of the sensor is a change in current against a one-order-of-magnitude change in CO concentration (current change unit/decade) which is calculated by a linear fit analysis using Microcal Origin program. The slope of equation: $y = mx + c$ is the sensitivity of the sensor related to gas concentration.
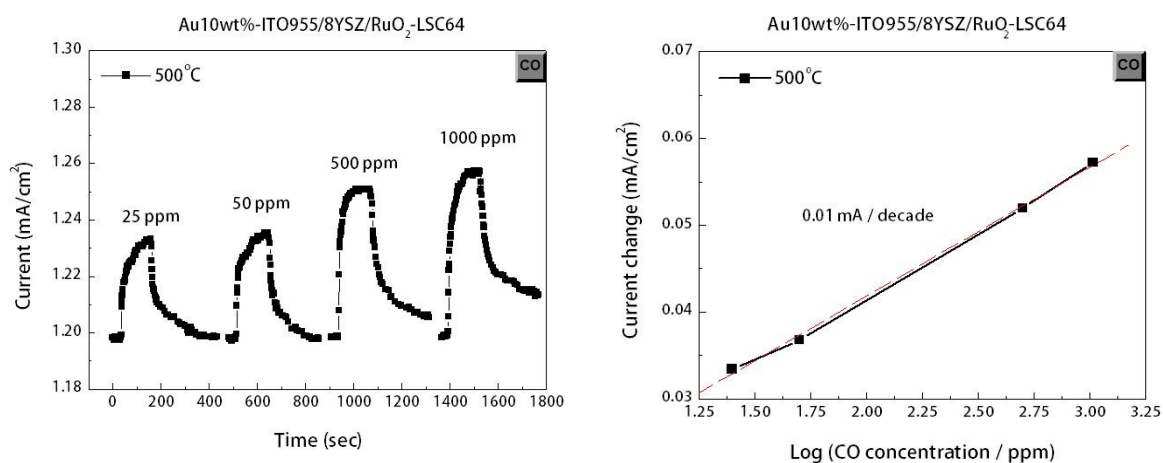

Figure B.1 The response curves and current change against CO concentration of the sensor using 8YSZ as electrolyte at 500°C.
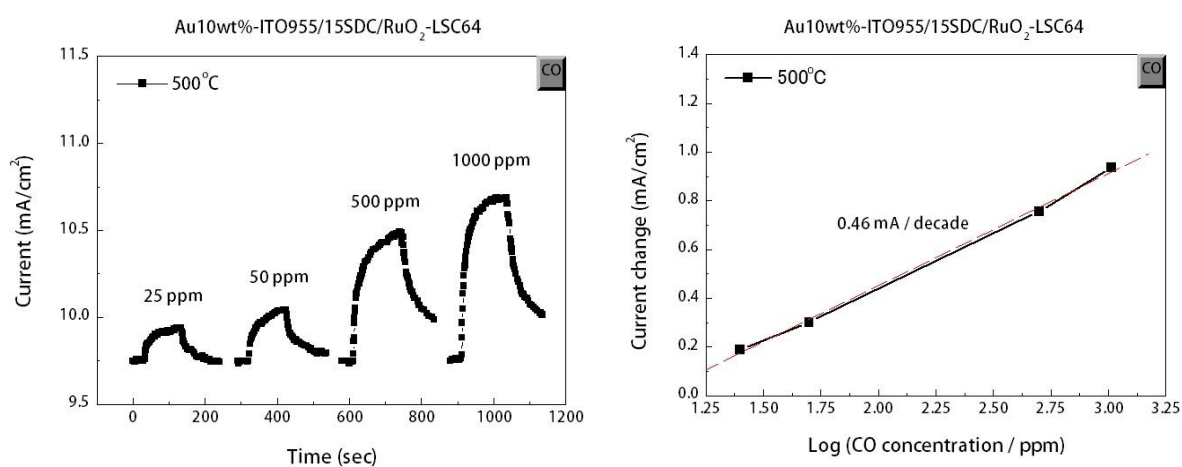

Figure B.2 The response curves and current change against CO concentration of the sensor using 15SDC as electrolyte at 500°C.
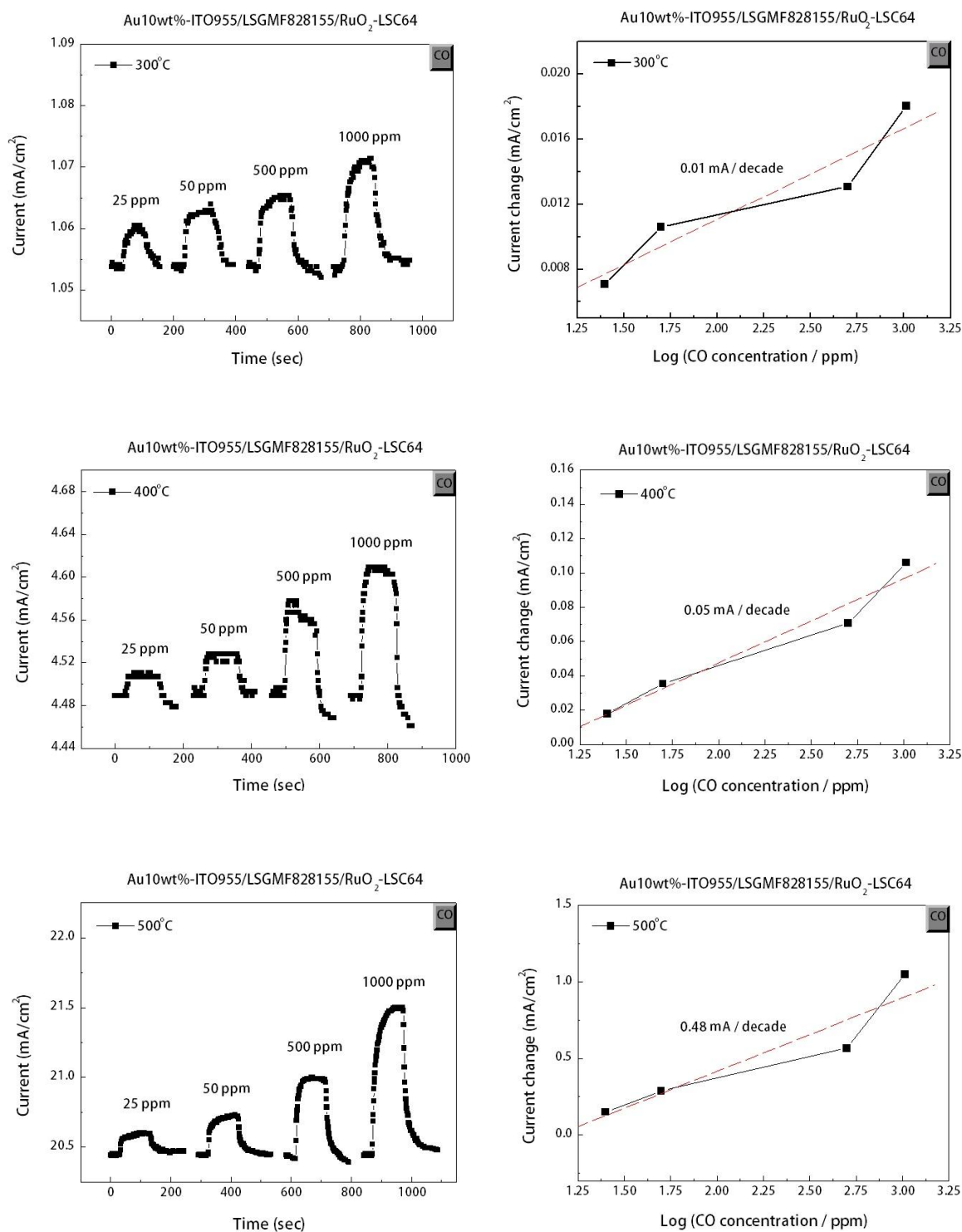
Figure B.3 The response curves and current change against CO concentration of the sensor using LSGMF828155 as electrolyte at 300°C to 500°C.
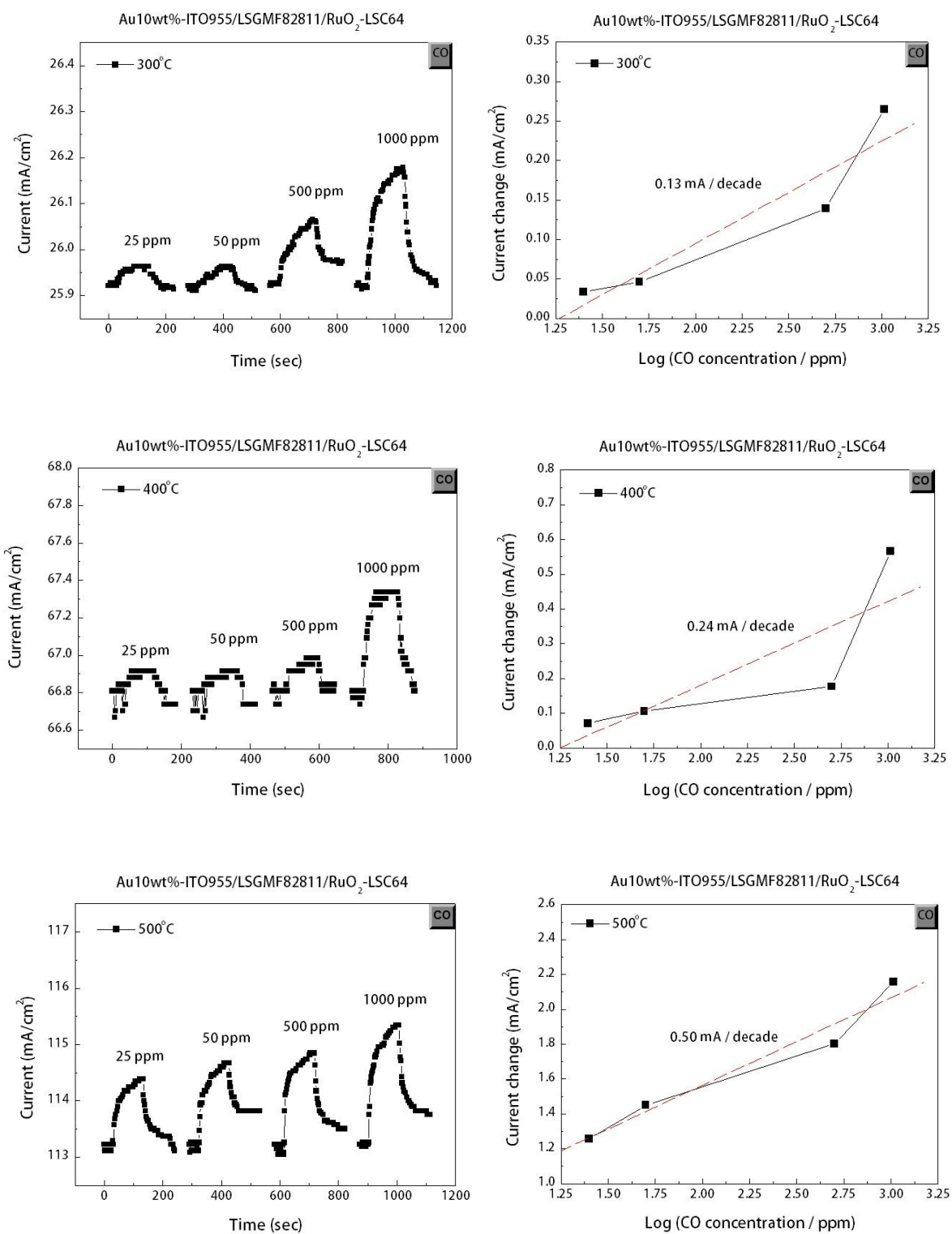
Figure B.4 The response curves and current change against CO concentration of the sensor using LSGMF82811 as electrolyte at 300°C to 500°C.
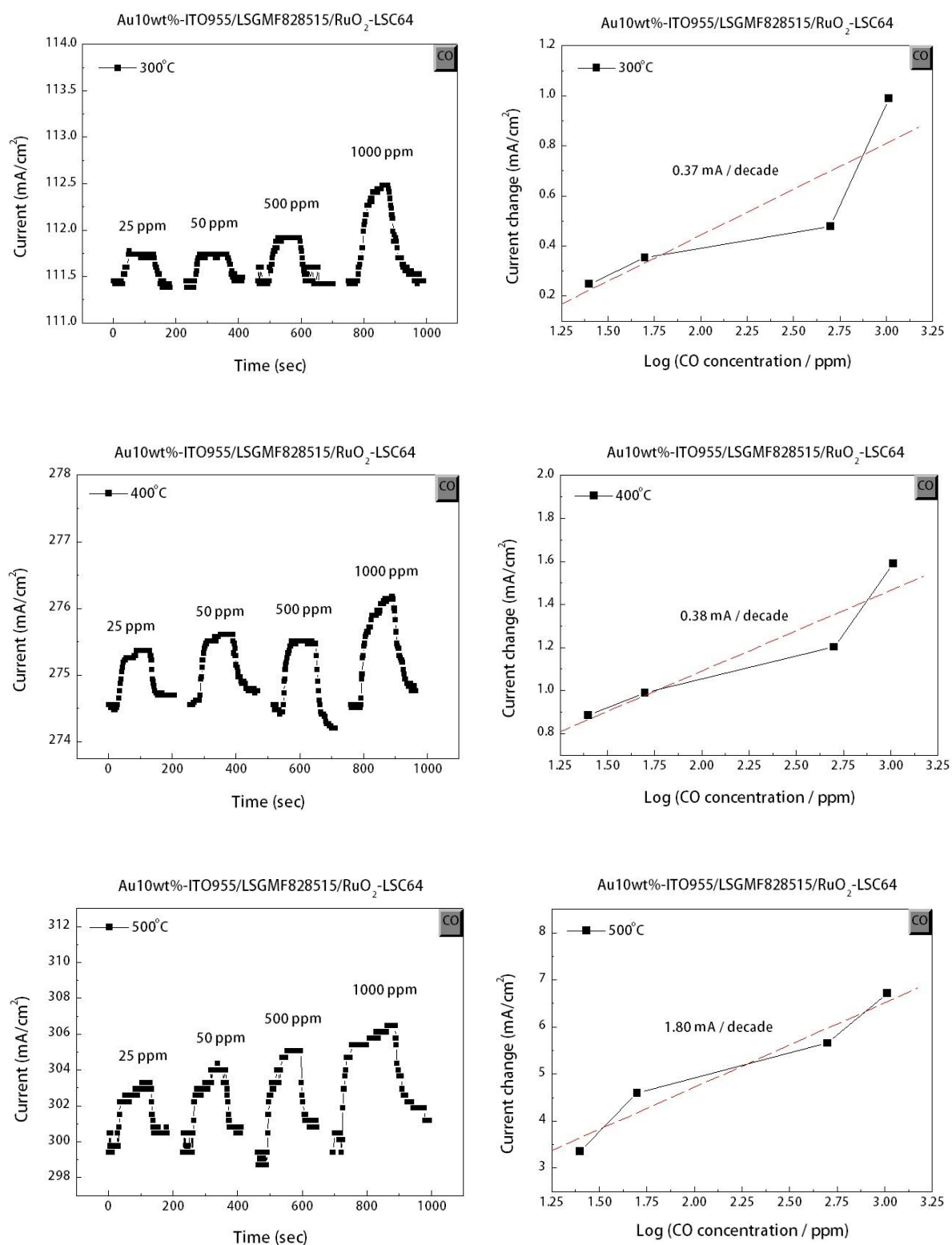
Figure B.5 The response curves and current change against CO concentration of the sensor using LSGMF828515 as electrolyte at 300°C to 500°C.
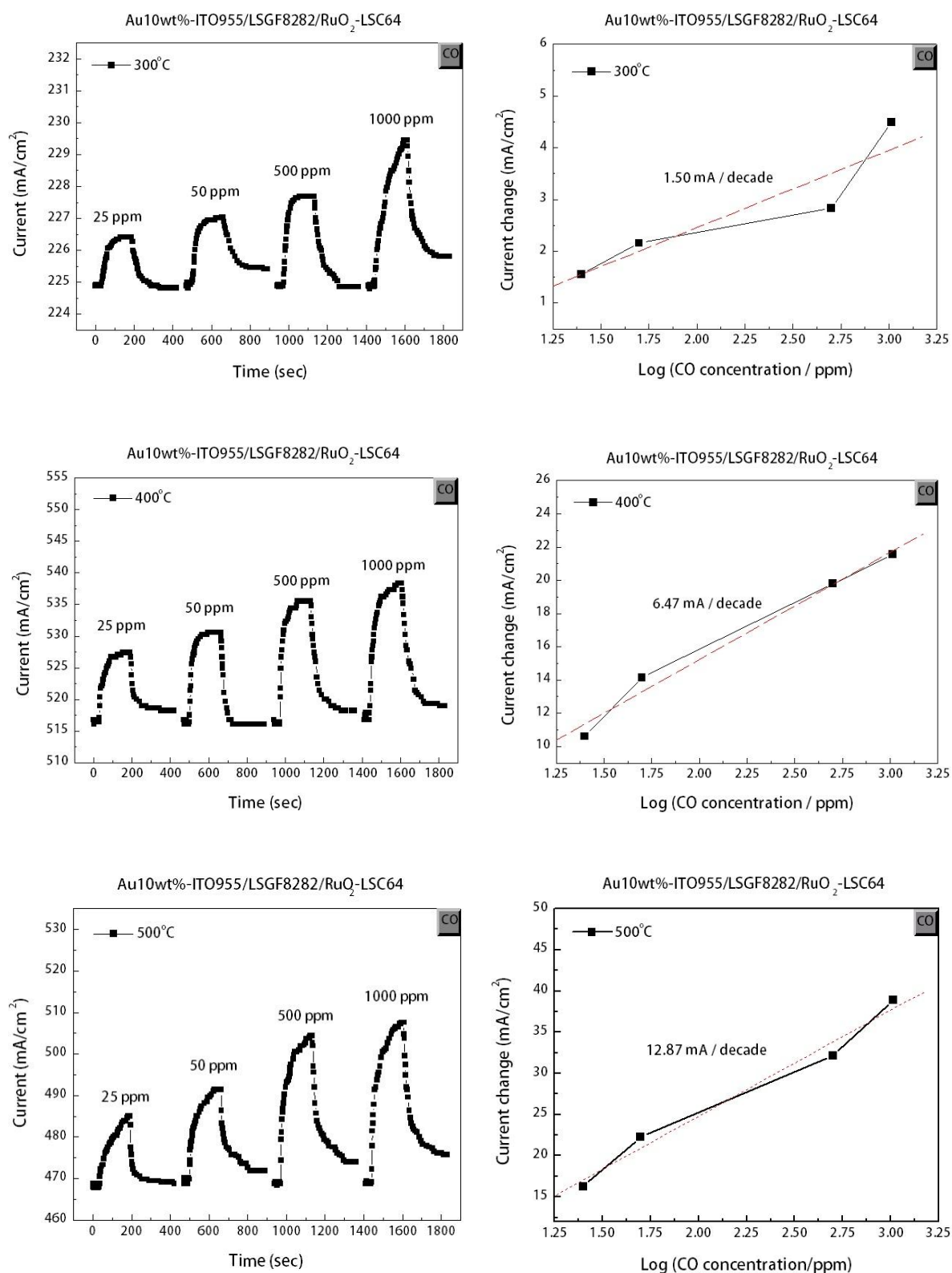
Figure B.6 The response curves and current change against CO concentration of the sensor using LSGF8282 as electrolyte at 300°C to 500°C.

Figure B.7 The response curves and current change against CO concentration of the sensor using LSGF8291 as electrolyte at 300°C to 500°C.

Figure B.8 The response curves and current change against CO concentration of the sensor using LSGF828515 as electrolyte at 300°C to 500°C.

Figure B.9 The response curves and current change against CO concentration of the sensor using LSGF8282 as electrolyte at 300°C to 500°C.
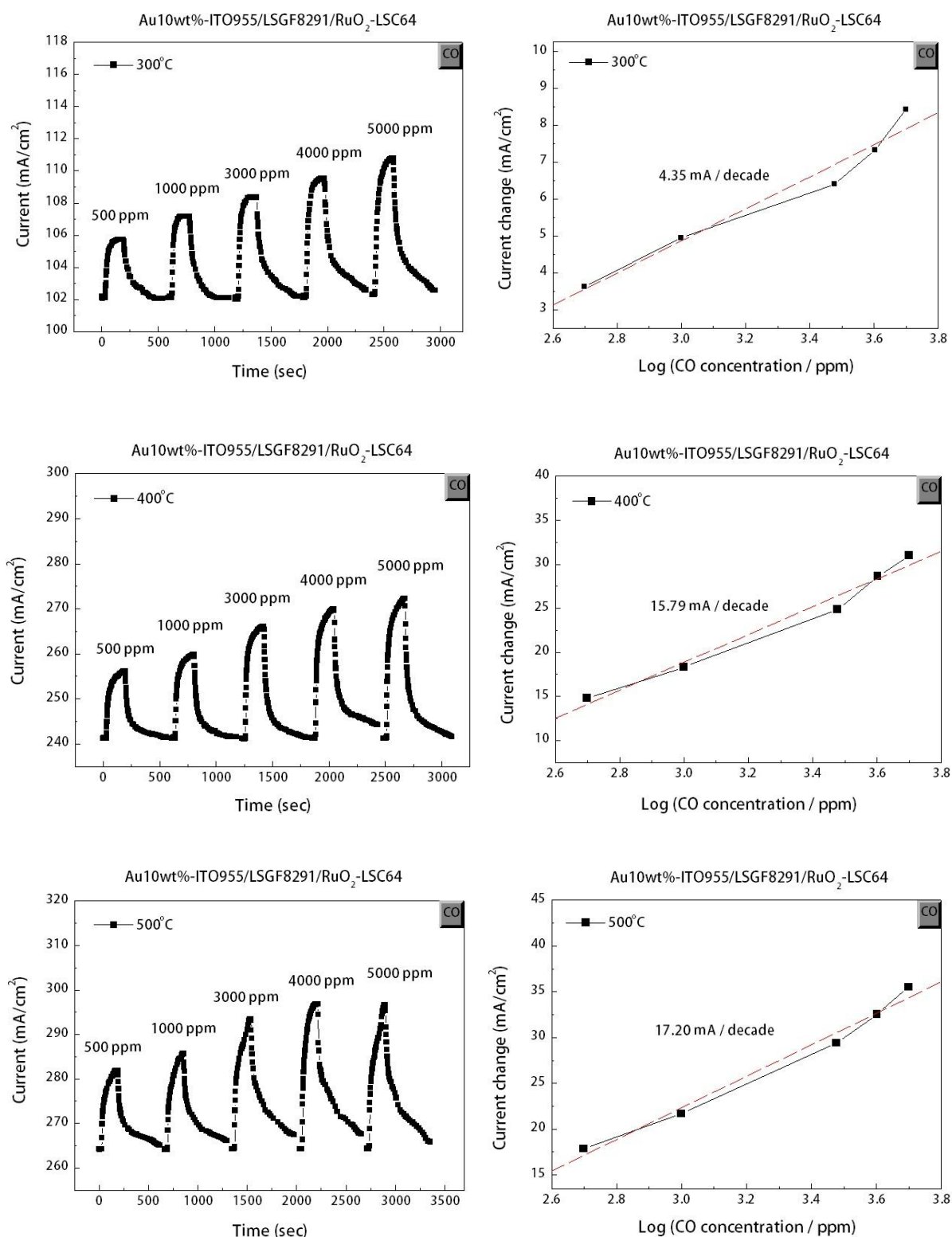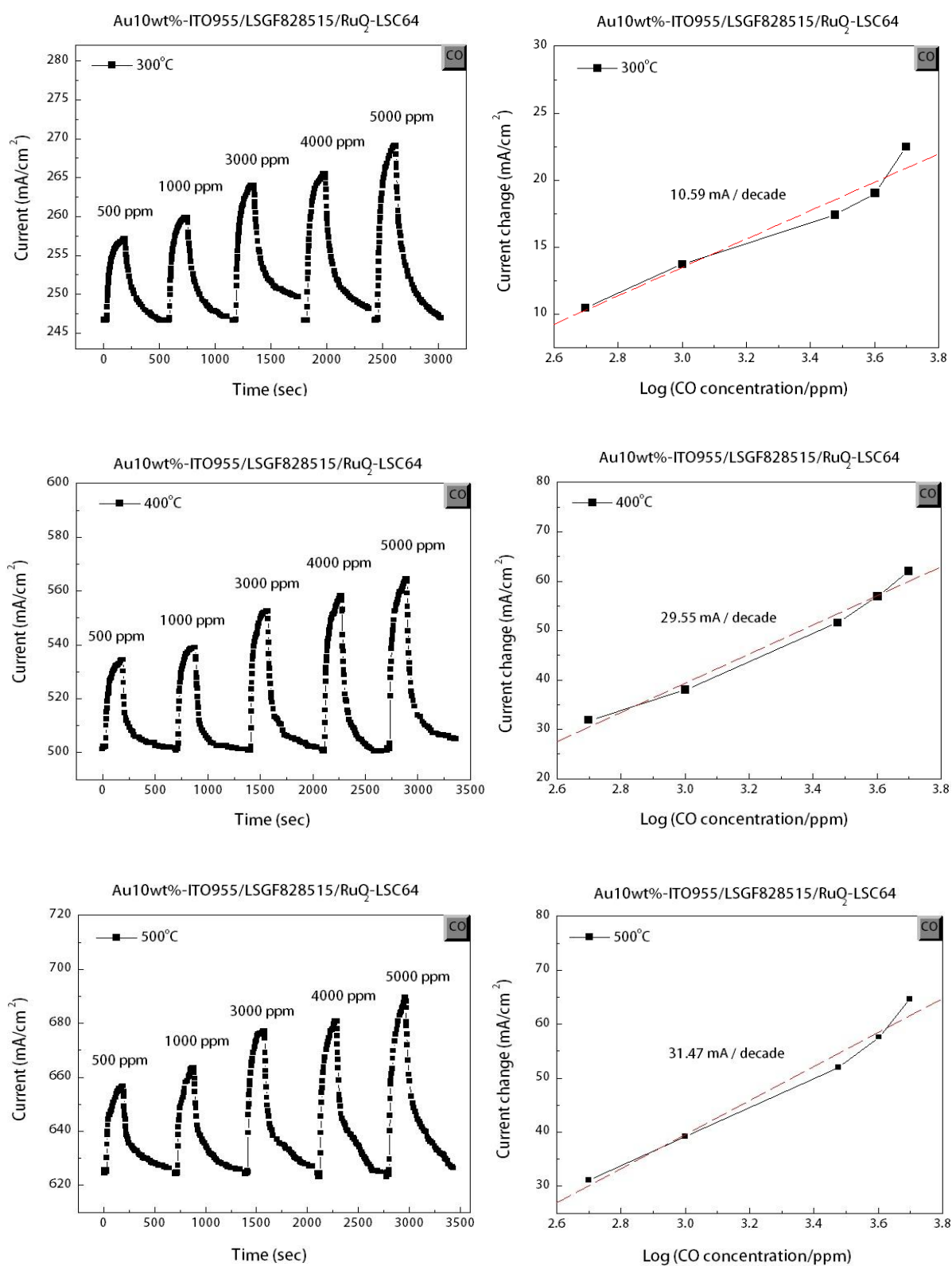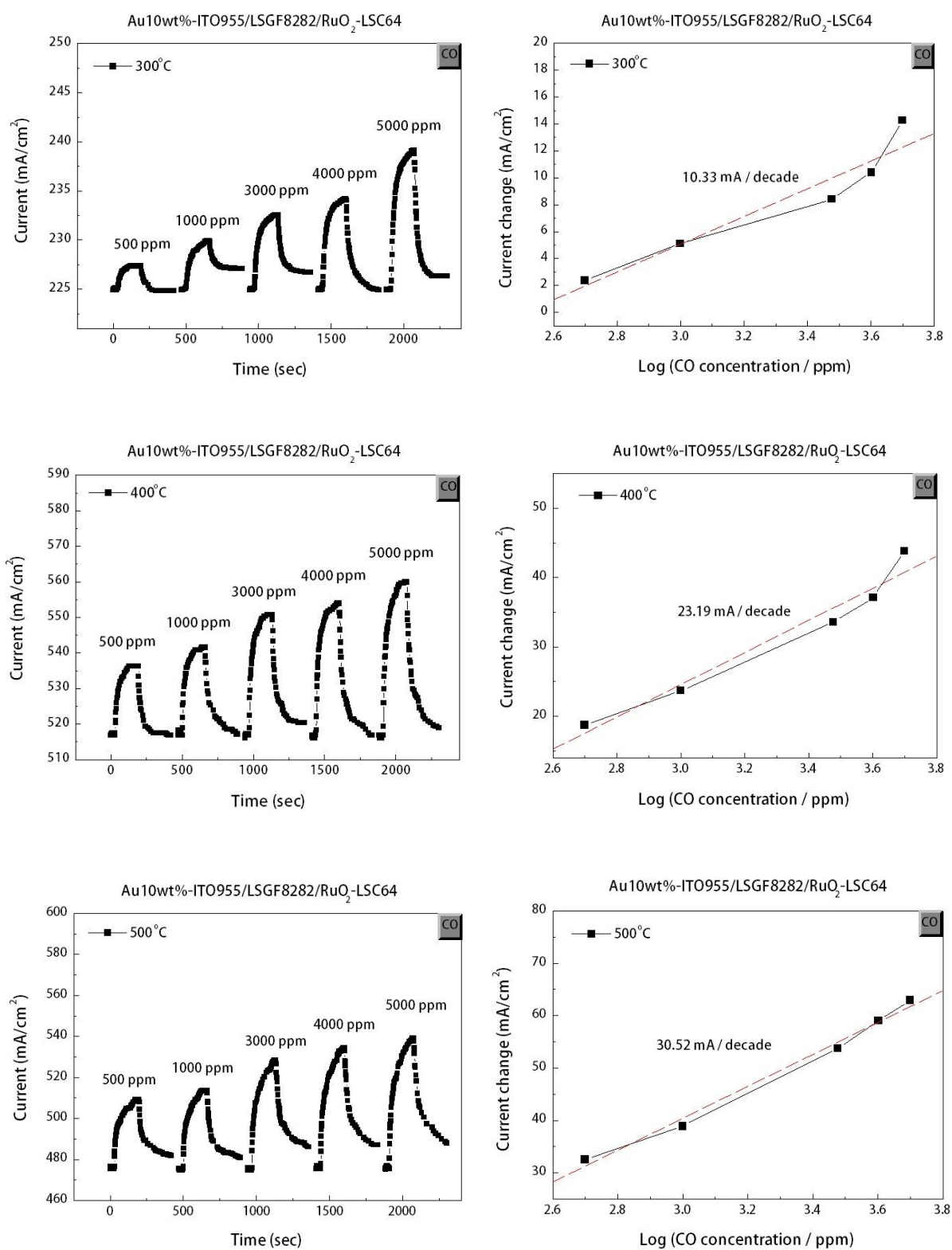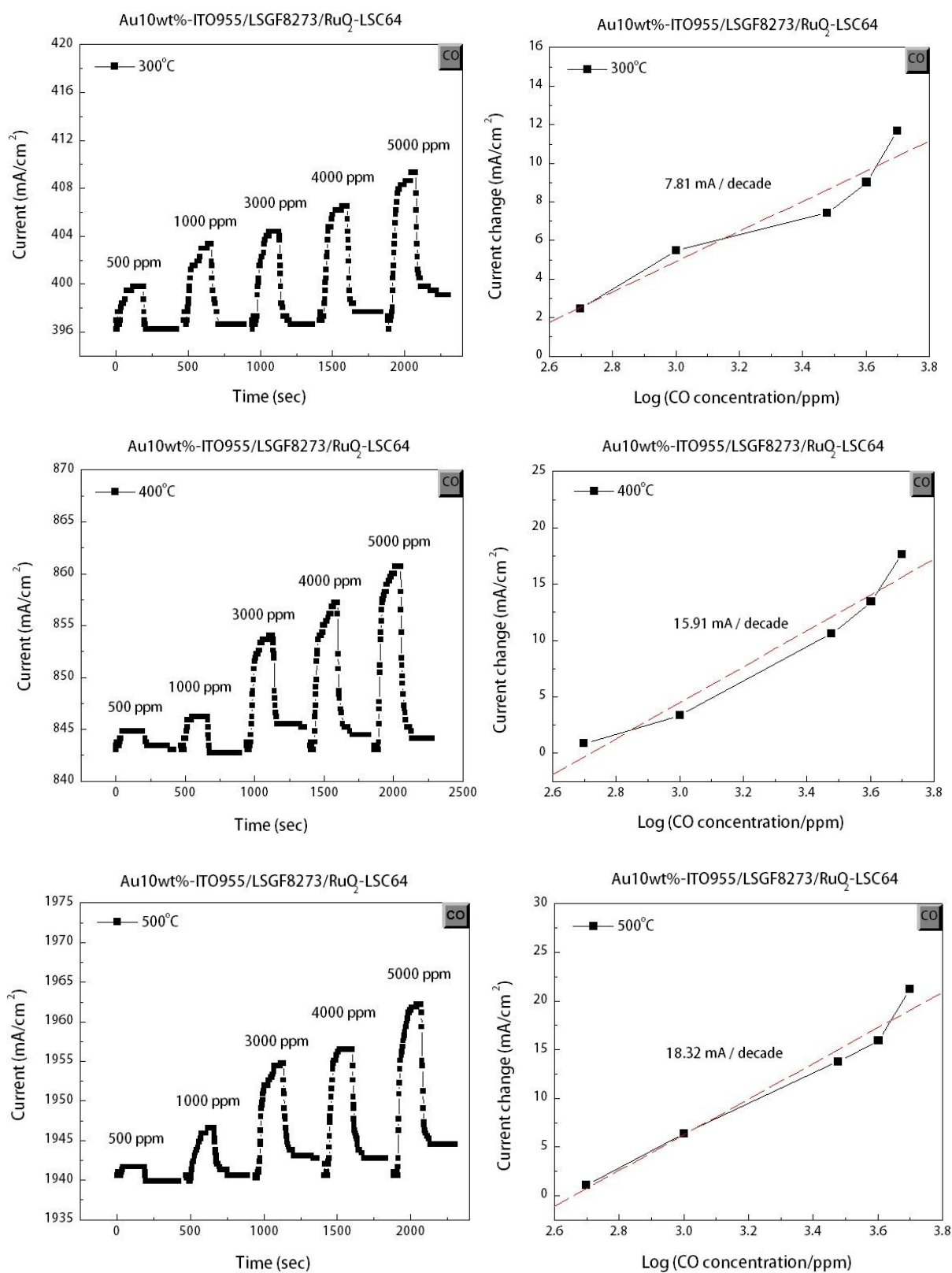
Figure B.10 The response curves and current change against CO concentration of the sensor using LSGF8273 as electrolyte at 300°C to 500°C.

Table B.1 Summary of the CO sensitivity of $La_{0.8}Sr_{0.2}Ga_{0.8}Mg_{0.2-x}Fe_xO_{3-\delta}$ (x = 0.05, 0.10, 0.15, 0.2)

Compounds	CO sensitivity (mA/decade) at various operating temperature		
	300°C	400°C	500°C
LSGMF828155	0.01	0.05	0.48
LSGMF82811	0.13	0.24	0.50
LSGMF828515	0.37	0.38	1.80
LSGF8282	1.50	6.47	12.87

Table B.2 Summary of the CO sensitivity of $La_{0.8}Sr_{0.2}Ga_{1-x}Fe_xO_{3-\delta}$ (x = 0.10, 0.15, 0.20, 0.30)

Compounds	CO sensitivity (mA/decade) at various operating temperature		
	300°C	400°C	500°C
LSGF8291	4.35	15.79	17.20
LSGF828515	10.59	29.55	31.47
LSGF8282	7.92	23.19	30.52
LSGF8273	7.81	15.91	18.32

APPENDIX C

Selectivity

Table C.1 Sensitivity and selectivity to various gases of LSGF828515 sensor at the operating temperature 400°C.

Gases	Concentration (ppm)	Sensitivity (mA/decade) at 400°C	Selectivity
CO	500-5000	27.79	1.00
CO_2	25000-50000	-0.26	0.01
CH_4	125-500	0	0.00
H_2	125 - 890	0.38	0.01

Selectivity (S) to CO is calculated from the following equation:

$$Selecticity = \frac{S_{gas}}{S_{CO}} \qquad (C.1)$$

Therefore, the selectivity of CO_2 is:

$$Selectivity = \frac{S_{CO_2}}{S_{CO}} = \frac{0.26}{27.79} = 0.01$$

VITAE

Name :	Miss Chanadda Phawachalotorn
Nationality :	Thai
Birthdate and place :	August 22, 1980; Trang

Education :

2007-2012: Ph.D. in Inorganic Chemistry, Department of Chemistry, Faculty of Science, Chulalongkorn University, Bangkok, Thailand

2002-2005: M.Sc. in Inorganic Chemistry, Department of Chemistry, Faculty of Science, Prince of Songkla University, Songkhla, Thailand

1998-2001: B.Sc. in Chemistry, Department of Chemistry, Faculty of Science, Prince of Songkla University, Songkhla, Thailand

Research experience :

2008-2009: Work as technician stuff at Department of Applied Chemistry, Faculty of Engineering, Kyushu University, Fukuoka, Japan

Scholarship :

Development and Promotion of Science and Technology talents project (DPST)

Publications:

[1] Ishihara, T., Phawachalotorn, A., Kadowaki, R., and Sanguanruang, O. Solid oxide amperometric CO sensor for monitoring exhaust gas from water heater. Sensors and Materials 22 (2010): 183-192.

[2] Phawachalotorn, C., Sanguanruang, O., and Ishihara, T. Highly selective amperometric sensors for carbon monoxide detection in exhaust gas. Sensors and Actuators B 161 (2012) 635-640.